

DOTTORATO DI RICERCA IN GEOFISICA

CICLO XXVI

Settore Concorsuale di afferenza: 04 / A4

Settore Scientifico disciplinare: GEO / 10

EARLY WARNING FOR LARGE EARTHQUAKES:
OBSERVATIONS, MODELS AND REAL-TIME
DATA ANALYSIS

Presentata da: Simona Colombelli

Coordinatore del Dottorato:

Prof. Michele Dragoni

Relatore:

Prof. Aldo Zollo

ACKNOWLEDGEMENTS

It's hard to find the words to say how grateful I am to my supervisor, Prof. Aldo Zollo. He has been guiding me for all these years, with constant feedback and lively enthusiasm. His continuous motivation and support are the reasons for all the things I have achieved. I thank him because he shares with me his immense knowledge. Because he has shown me the way to follow, but always let me the freedom I asked. And because he has listened to me whenever I needed it.

A very big big thanks to Antonio Emolo. To me he is a teacher first, and a friend just after. I thank him for his deep esteem and for the trust he has always had in me. His precious advices have made me grown up more than any other thing.

A few, but special words I wish to tell to Gaetano Festa, which I got to know better throughout these years. You have been a model to follow, somebody to whom be inspired.

I will be forever thankful to Richard Allen, for how much I have learned while working with him during my seven months at the University of California, Berkeley. I am sure he does not know of how important it has been for me.

A great thanks to Matteo Picozzi, for his friendship and professional collaboration and for always being so understanding with me.

I am grateful to Raffaella De Matteis, for the careful and patience with which she has reviewed my thesis. I really appreciated the suggestions she gave me.

I acknowledge Prof. Paolo Gasparini, for having supported me from the very beginning of this experience.

A special thanks to my favourite colleagues Antonella Orefice, Sergio Del Gaudio and Claudio Martino, for having given me a smile in the hardest times.

Thanks to all students, post-docs, researchers and to all the present and past *RISSCLab* people, for making these three years with them a wonderful time. A special thanks to the *0F14-room* guys. I really don't know how they can stand me in the room!

Thanks to Qingkai Kong and Serdar Kuyuk. They didn't make me feel alone, while I was completely alone.

Words cannot express my gratitude to my family. During these three years I have shared with them from the basic physics of seismology to the deepest feeling of my heart. Thanks for our long after-dinner talks... I've loved them so much!

Finally, a sincere and deep thanks to Martino. Thanks for having been with me throughout this experience, for having understood my needs and for having always remembered that I was working on a dream ...

CONTENTS

Acknowledgements	3
Introduction	9
PART I - The Tohoku-Oki Event: a case-study for Early Warning	15
1 The 2011, M 9.0 Tohoku-Oki Earthquake	17
1.1 Outline of the earthquake	17
1.2 Twin ruptures for the giant earthquake	18
1.3 Frequency dependent slip radiation	19
1.4 Time evolution of the rupture process	22
2 Early magnitude estimate for the Tohoku-Oki earthquake	25
2.1 The concept of real-time magnitude estimate	25
2.2 Evidence for the parameter saturation	26
Box 2.1: EEW parameters and scaling relationships . . .	29
2.3 Suitability of the existing methodologies	30
2.4 Preliminary analysis	31
2.5 Expanding the P-wave Time Window	32
2.6 Real-Time Analysis	34
2.7 Discussion	36
PART II - From the observations to a physical model for the rupture beginning	39
3 Time evolution of Early Warning parameters	41
3.1 Database description and method	41

3.2	P_d and τ_c vs. time: overall results	43
3.3	P_d vs. time: a deeper look at the curve	44
4	Peak displacement amplitude vs. time: observed trend, scaling and physical interpretation	47
4.1	Scaling of T2, B2 and PL with magnitude	47
	Box 4.1: P_d vs. Moment Rate Function relationships . .	50
4.2	Scaling of T1 and B1 with magnitude	51
4.3	Initial slope: analysis at a fixed time window	51
4.4	A physical model for the rupture initiation	53
4.5	Considerations for the real-time applications	55
	Box 4.2: The nucleation phase and the slip-weakening model	56
	PART III: Real-time strategies for the extended source effects	59
5	Rapid Estimate of the Potential Damage Zone	61
5.1	The Threshold-Based Approach	61
5.2	Local Alert Level Definition	63
	Box 5.1: Basic equations of the method	64
5.3	Potential Damage Zone Definition	66
5.4	Application to strong Japanese events	67
5.5	Application to the Tohoku-Oki event	69
5.6	Discussion	71
6	Application of real-time GPS to Earthquake Early Warning	73
6.1	Introduction of GPS data	73
6.2	Real-time strategy	75
	Box 6.1: Permanent displacement extraction	77
	Box 6.2: Point source magnitude	78
6.3	Early Warning outputs	78
	Box 6.3: Static-slip inversion	80
	Box 6.4: Ground shaking prediction	82
6.4	Application and results	83
	6.4.1 The Mw 9.0 2011 Tohoku-Oki earthquake . . .	83
	6.4.2 The 2003 Mw 8.3 Tokachi-Oki earthquake . . .	86
	6.4.3 The Mw 7.2 El Mayor-Cucapah earthquake . . .	89
6.5	Discussion	92

Conclusions and perspectives	95
A Supporting Information	101
A.1 Database description	101
A.2 Description of data processing	103
A.3 Resolution and tests	105
A.3.1 Filter effect	105
A.3.2 Distance effect	107
A.3.3 Source depth effect	109
A.4 Validation of the linear trend	110
A.5 Residual analysis	111
A.6 Dependency on the fit model	111
Data and Resources	115
Bibliography	116

INTRODUCTION

This thesis is placed in the context of Earthquake Early Warning, with a special attention to the large magnitude events. Earthquake Early Warning Systems are real-time information systems able to rapidly detect an ongoing earthquake and broadcast a warning in a target area, before the arrival of the most destructive S-waves. Different observational parameters, typically amplitude and period parameters, are measured within a few seconds of P-wave signal and are used to rapidly estimate the magnitude of the ongoing earthquake and to predict the expected ground shaking at the same site or at some other location. Depending on the source-to-site distance, warning times, i.e., the *"lead-times"*, can be a matter of seconds, tens of seconds or even minutes, when the distance from the earthquake epicenter is large.

Thanks to advances on technological issues, Earthquake Early Warning Systems experienced a sudden improvement and a wide diffusion in many seismic regions of the world in the last three decades. Operative Earthquake Early Warning Systems are currently in Japan, Taiwan, Mexico, California and Romania. Development and testing is currently being doing in Southern Italy, Turkey, China, Switzerland and South Korea. Feasibility studies are finally in progress for Greece, South Iberia region, Israel and Eastern Caribbean Islands.

Earthquakes are among the most disastrous natural events which affect many seismic regions of the world. Most of the observed damage

is often due to collateral phenomena triggered by the earthquake, such as landslides, tsunamis, explosions, fires and industrial accidents. The application of Early Warning Systems represents an important contribution to the real-time risk mitigation. Many systems and facilities can benefit even from a short warning time. Among them, for example, transportation systems, schools, gas pipelines, elevators, power plants. Human actions may take longer, but if population is educated to the rapid response actions, a few seconds can save lives.

Earthquake Early Warning is a complex and articulated matter, involving technological and practical aspects - related to the instruments, algorithms, and operative methodologies - and more theoretical issues, related to the physics of the rupture processes. All of these aspects are indispensable one to each other for the reliability and the efficiency of the systems. Developing an ideally perfect methodology which cannot be applied in real-time is meaningless. On the other hand, writing fast and stable algorithms, without a deep investigation of the physical aspects, is dangerous.

This thesis is a collection of works focused on the topic of Early Warning for large earthquakes, with a special attention to the methodological and physical aspects of the problem. The topic is addressed from different points of view and the structure of the thesis reflects the variety of the aspects which have been analyzed. The thesis is divided into three main parts.

The first part is dedicated to the giant, 2011 Tohoku-Oki (Japan) earthquake, which is the largest and best recorded seismic event occurred since the Japanese Earthquake Early Warning system is operative (i.e., since October 2007). Because of its large magnitude and its complex rupture process, this event is an ideal case to test the existing methodologies for Earthquake Early Warning. An overview of the earthquake is provided in the first chapter, where the main features of

its rupture process are analyzed and discussed. In the second chapter the Tohoku-Oki earthquake is used as a case study for Early Warning methodologies.

Critical aspects and limitations of the standard approaches for large events arise in this chapter. The difficulties are related to the real-time magnitude estimate from the first few seconds of recorded signal. The rupture process of an earthquake is the result of a complex and random combination of many factors and the final magnitude depends on some average quantities of the whole process. In case of a large earthquake ($M > 7$) tens of seconds are necessary for the whole process to be concluded. In Early Warning system, the magnitude estimates are done using a small portion of the P-wave signal (a few seconds) while the rupture is still ongoing. Whether and how a few seconds can be used for the magnitude prediction has not yet been fully understood. In the second chapter a new strategy for the rapid magnitude estimate is proposed and applied to the single Tohoku-Oki earthquake. The application of this strategy, while solving some of the limitations, raises relevant issues about the physics of the rupture process. Upon these issues, the effectiveness of Early Warning systems and the feasibility of real-time magnitude estimate are based. A deeper analysis and the extension of the proposed methodology to other earthquakes are thus required in order to answer the questions raised.

With this purpose the second part of the thesis begins. Here a larger number of earthquakes is analyzed, including small, moderate and large events. Starting from the measurement of two Early Warning parameters, the behaviour of small and large earthquakes in the initial portion of recorded signals is investigated. The aim here is to understand whether small and large earthquakes can be distinguished from the initial stage of their rupture process.

Contrasting models have been provided so far to describe the earthquake initiation process. In the first model, which is usually referred

to as the "cascade model", the rupture starts in the same way for small and large magnitude events. What controls the final size are the friction conditions across the fault plane, which may either oppose or favour the fracture propagation, resulting in the breaking of a small fault patch or, alternatively, in the rupture of a big size asperity. The immediate implication of the cascade model is that a seismic event is a pure stochastic process for which the final size is unknown until the rupture has finished and it is even more undetermined when only the beginning of the process is considered. An opposite point of view is that of deterministic models, which explain the final size of an earthquake in terms of a different initiation process.

So far, the analysis of data has provide contradictory observations. Some authors support the idea of the unpredictable earthquake magnitude, i.e., they looked at the initial portions of P-wave recordings for different magnitude earthquakes and found no evidence for a magnitude-dependent rupture initiation. Other studies have shown, instead, the existence of features in the initial phase of earthquakes that somehow control their final size.

In this second part of the thesis, we analyzed the time evolution of two Early Warning parameters (the peak displacement amplitude and the average period) and observed a different initial behaviour between small and large events. A plausible interpretation for the observations is finally proposed and a physical model related to the nucleation phase of earthquakes is suggested.

The third part of the thesis is meant to be the continuation and the integration of the first part and is focused on practical, real-time applications. Beyond the real-time magnitude estimation another relevant goal of an Early Warning system is the rapid identification of the potentially damaged zone and the prompt broadcasting of a warning in the highest vulnerable areas before the arrival of the strongest shaking, so that security actions can be rapidly activated.

To this aim, in the final part of the thesis, two different approaches for the rapid prediction of the potential damaged zone are proposed and discussed. The first one is a "threshold-based" method which uses traditional seismic data. The method is essentially based on the real-time, joint measurement of two Early Warning parameters, which are compared to threshold values, for the definition of a local alert level. The real-time mapping of the alert levels provides an estimate of the Potential Damage Area.

Then an innovative approach based on the use of continuous GPS data is explored. In this approach, the static component of ground motion is used for a real-time mapping of the slip distribution on the fault plane, providing reliable magnitude estimates and allowing for a rapid characterization of the extension of the source.

Both strategies provide an extended image of the ongoing seismic phenomena and are aimed at improving the prediction of large scale effects of strong earthquakes. The ground shaking maps can be used in real-time for the prompt activation of emergency procedures and in the immediate post-event emergency phase for an efficient planning of the rescue operations.

Within the whole thesis a few insert box are included, which are auxiliary to the main text and essentially contain further details about methodological and theoretical aspects. Finally, an appendix contains supplementary analysis to support results and conclusions of the main text.

PART I

THE TOHOKU-OKI EVENT: A CASE-STUDY FOR EARLY WARNING

The mega-thrust, 2011 Tohoku-Oki earthquake has re-opened the discussion about the effectiveness of Earthquake Early Warning systems for such large events. For this earthquake, the complexity of the rupture process played a key role for the real-time magnitude estimate and the limitations of the standard approaches have become evident after the experience of this event. The initial magnitude released by the Japan Meteorological Agency was significantly underestimated (M 4.3) and only about two minutes after the earthquake occurrence it was increased to the value of M 8.1.¹

The following two chapters are dedicated to the Tohoku-Oki earthquake. First, the main features of the source process are summarized. The images of the rupture evolution and the space-time variation of the slip on the fault plane are then discussed in order to point out the complex features of the rupture process.

In the second chapter, after a brief introduction to the problem of real-time magnitude estimate, we investigated the suitability of existent Earthquake Early Warning methodologies and empirical regression laws for the Tohoku-Oki earthquake. During this event, the dense strong-

¹See Hoshiaba et al. 2011 for a detailed reconstruction of the Earthquake Early Warning announcements released by Japan Meteorological Agency.

motion networks deployed across Japan provided seismic observations over wide ranges of distances and azimuths from the source, with a high signal-to-noise ratio up to several hundred kilometers from the source. We have no experience of any other giant earthquake with such a high quality and number of records. The Tohoku-Oki event thus represents a unique opportunity to check the extension of present methodologies up to giant earthquakes, to bring out their limits and to propose new strategies to overcome such limitations.

Within the second chapter, an evolutionary approach for the rapid magnitude estimate of a large event is proposed and tested for this single case.²

²The analyses presented in the following two chapters are extracted from: Maercklin, N., Festa, G., Colombelli, S. and Zollo, A (2012). Twin ruptures grew to build up the giant 2011 Tohoku, Japan, earthquake, *Sci. Rep.* 2, doi 10.1038/s-rep00709.

Colombelli, S., Zollo, A., Festa, G. and Kanamori, H. (2012). Early magnitude and potential damage zone estimates for the great Mw 9 Tohoku-Oki earthquake, *Geophys. Res. Lett.* 39, doi 10.1029/2012GL053923.

THE 2011, M 9.0 TOHOKU-OKI EARTHQUAKE

1.1 Outline of the earthquake

The giant Tohoku-Oki earthquake occurred on March 11th, 2011 at 05:46:24 UTC at $38.297^{\circ}N$, $142.372^{\circ}E$ and depth = 30 km (USGS Agency information) near the east coast of Honshu, Japan, on a crustal portion of the subduction zone at the boundary between the Pacific and Okhotsk (North American) plates (Figure 1.1). In this region the overriding continental plate is dragged down by the subducting Pacific plate (Ito, Yoshioka, and Miyazaki 2000).

Large earthquakes have struck the northeast Honshu island also in the recent past, reaching magnitudes as large as M 8.2 (Hashimoto et al. 2009). These events originated in the deepest part of the seismogenic zone along the descending slab (at 30-50 km depth), such as the case of the 1978, M 7.6, Miyagi-Oki earthquake. A magnitude 9.0 event, however, sounded as almost unexpected for this zone of the Japan slab (Stein and Okal 2011).

The USGS's W-phase moment tensor inversion and finite fault model solutions suggest a mega-thrust earthquake (strike 193° , dip 14° , rake 81°) rupturing an area of about 300x150 km, with a cumulative seismic moment of 4.42×10^{22} Nm. Slip models indicate that the fault moved upwards of 30-40 m with a permanent horizontal displacement exceeding 4 m at the closest coastal station and significant ground motion up

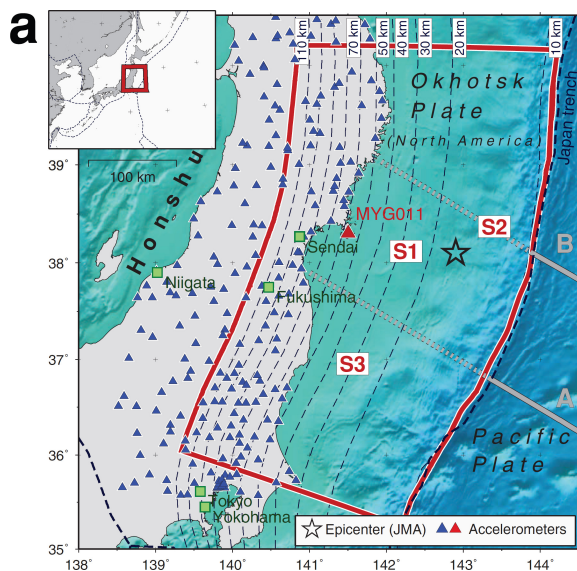


Figure 1.1: Earthquake source region. Map of the Japan region showing the event epicenter from the Japan Meteorological Agency. The background image is the bathymetry, with blue colours indicating deeper sea bottom and dashed contours showing the depth to the subducting plate. The main source regions S1, S2, and S3 and the used accelerometer stations (triangles) are also shown. [After Maercklin et al. 2012.]

to 300 km from the hypocenter (Simons et al. 2011).

1.2 Twin ruptures for the giant earthquake

The closest station, MYG011, where a peak ground acceleration of about 1 g has been recorded, clearly displays two main high-frequency transients (Koketsu et al. 2011; Meng, Inbal, and Ampuero 2011). These are delayed about 50 seconds from each other, and the second wave packet has the same peak amplitude but a larger duration than the first one (Figure 1.2a).

The relatively long time separation and the similar peak amplitudes on near-field accelerograms suggest that the second phase is due to a radiating seismic source rather than to secondary or multi-path arrivals related to wave propagation. The band-pass filtered displacement records confirm the evidence for two main phase arrivals, hereafter referred to as *S1* and *S2*. These two large-amplitude phases can be clearly identified in the whole distance range on the time versus distance seismic section of displacement records (Figure 1.2b), show-

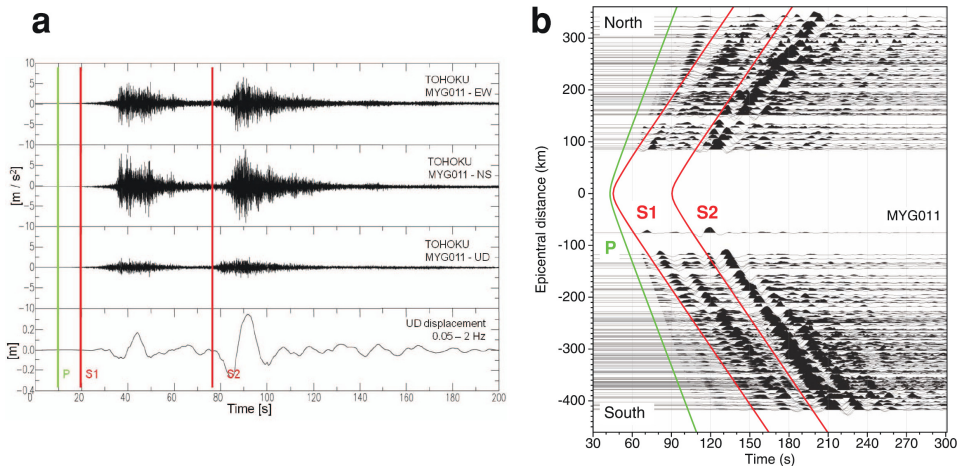


Figure 1.2: Waveform data. (a) Recorded acceleration waveforms at station MYG011, and vertical (UD) component of band-pass filtered displacement record (bottom trace). Green and red bars show theoretical P -wave, $S1$ - and $S2$ -wave arrival times. (b) Band-pass filtered and amplitude-normalized vertical-component displacement records, sorted by distance from the epicenter. The red lines approximate the arrivals of the phases $S1$ and $S2$, and the slopes of the red lines indicate an S -wave velocity of 3.7 km/s. Time is in seconds after 05:46 UTC on 11 March 2011. [After Maercklin et al. 2012.]

ing that both phases propagated at a velocity close to the average shear wave speed in the crust (3.7 km/s). Therefore, and because of their linear polarization, the phases can be interpreted as S-wave pulses radiated during the initial stage of the Tohoku-Oki earthquake rupture from two distinct sources.

1.3 Frequency dependent slip radiation

Kinematic models obtained from inversion of geodetic, strong-motion, teleseismic and tsunami data revealed a complex rupture propagation, with a frequency dependent radiation (Ide, Baltay, and Beroza 2011). Tsunami, geodetic and teleseismic data indicate an anomalously large slip at shallow depths in the trench vicinity (Koketsu et al. 2011; Lee

et al. 2011; Romano et al. 2012). High frequency radiation around 1 Hz was inferred to be generated in the deeper regions of the plane, beneath the Japanese coast (Ishii 2011; Kurahashi and Irikura 2011). The images of the earthquake rupture evolution as inferred from back-projection of wave amplitudes of teleseismic records (e.g., Yoshida, Miyakoshi, and Irikura 2011; Ide, Baltay, and Beroza 2011) show that the first two sources activated almost in the same area of the subducting Japan slab, nearby the hypocentral region, about 80 km eastward off the Sendai coast, producing most of the earthquake moment release within the first 100 seconds of the rupture. On the other hand, late, less energetic, sources have been activated after about 100 seconds and 200-300 km south east of the hypocentral area.

The modelling of strong-motion records, in terms of high frequency radiating sources, confirms this evidence, with the most energetic sources being located nearby and westward of the earthquake epicenter (Kurahashi and Irikura 2011).

The behaviour of the rupture in the intermediate frequency range was proven to show some complications when kinematic models are obtained from backprojection of teleseismic data (Koper, Hutko, and Lay 2011; Meng et al. 2012).

To model the space-time variation of the earthquake fault slip in the intermediate frequency range and estimate the associated slip amount, Maercklin et al. (2012) developed and applied a backprojection technique to local strong-motion data, filtered in three frequency bands (0.05-0.1 Hz, 0.1-0.2 Hz, and 0.2-0.4 Hz). Figure 1.3 shows the cumulative slip of the entire rupture for the three investigated frequency bands. Most of the slip is released in the 0.05-0.1 Hz band, in which the slip distribution is dominated by three main large-amplitude source regions (S_1 , S_2 , and S_3). The first one is located southwest and closest to the hypocenter, exhibits slip amplitudes of up to 25 m, and is responsible for the S_1 phase. The second, largest source corresponds

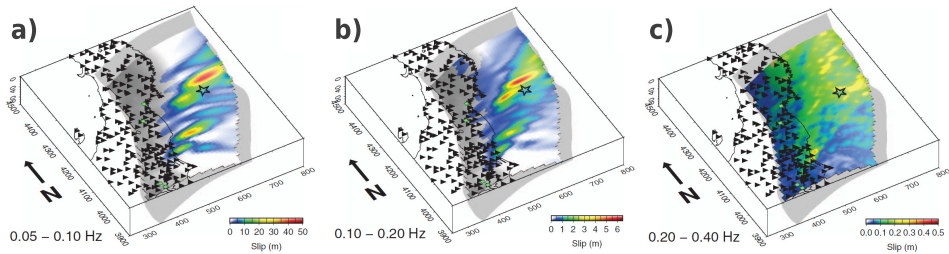


Figure 1.3: Slip distribution. Colour-coded final slip distribution obtained from backprojection in different frequency bands. Frequencies and the respective colour scale are given below each image. [After Maercklin et al. 2012.]

to the $S2$ phase and is located in northeastern, up-dip direction from the hypocenter, nearby the oceanic trench. In the studied frequency band, the $S2$ source is imaged in a rather small area of about 100×50 km, and it shows maximum slip values as large as 50 m, which presumably contributed to the generation of extremely high amplitude tsunami waves. The third strong source, $S3$, with a slip amount of about 40 m, is located 200 km southwest, on the deeper portion of the slab and close to the coast. The seismic phase associated with this source region is not as clearly visible as those of the previous two, because it is hidden by the dominant $S2$ phase for most of the stations along the section (Honda et al. 2011).

Going to higher frequency bands, a very similar image is obtained in the intermediate band 0.1-0.2 Hz, whereas the image from the highest-frequency data (0.2-0.4 Hz) shows a more chaotic distribution, with the largest values in the northern half of the rupture area and located in the vicinity of the source regions of largest slip seen in the lower-frequency images. From one frequency band to the consecutive, higher one, the results show a decrease in maximum slip amount in one order of magnitude (50 m, 6.5 m, and 0.5 m, respectively). The total moment released on the entire fault plane within each frequency band corresponds to respective moment magnitudes M_w of 8.8, 8.3, and 7.8.

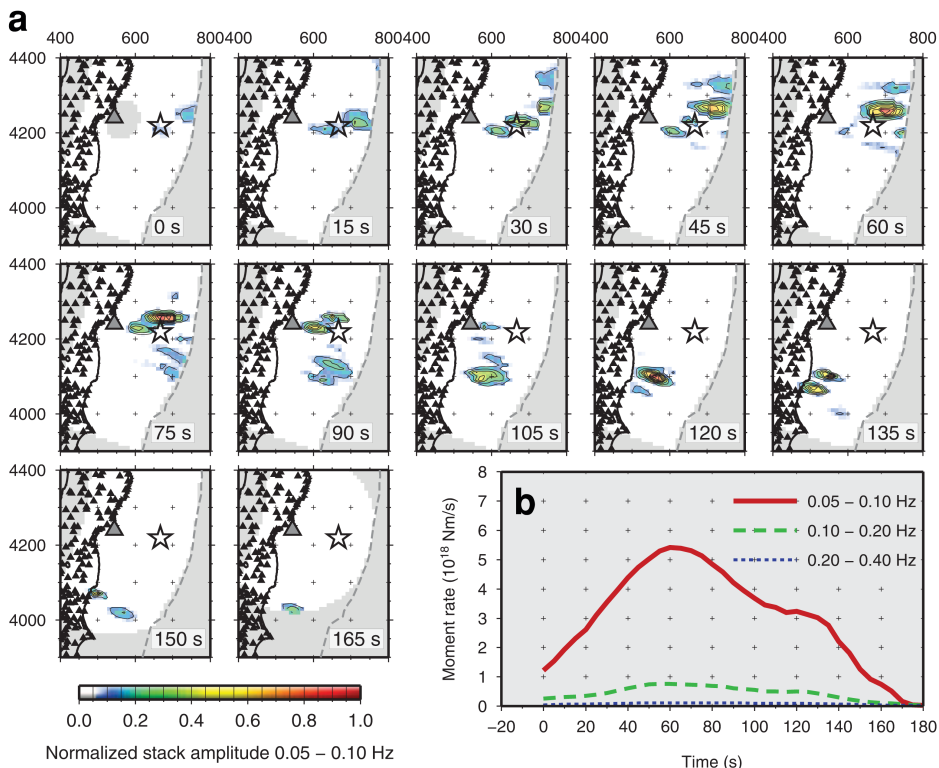


Figure 1.4: Rupture evolution and moment rate. (a) Time slices of the rupture evolution for the 0.05–0.10 Hz band in 15-second intervals. Coordinates are in km (UTM grid). (b) Moment rate functions for the three frequency bands obtained from the rupture time slices. [After Maercklin et al. 2012.]

1.4 Time evolution of the rupture process

The space-time evolution of the slip function has been tracked by Maercklin et al. (2012), by repeating the backprojection imaging in a sliding time window, in the three frequency bands (0.05–0.1 Hz, 0.1–0.2 Hz, and 0.2–0.4 Hz). Figure 1.4a shows the evolution of the rupture as a function of time for the 0.05–0.1 Hz frequency band (i.e., the range where most of the slip has been released). The snapshot images reveal that during the first 60 seconds the giant earthquake grew up as twin ruptures mainly developing bilaterally, almost along-dip within a

100 km wide slab stripe. A rather slow (less than 2 km/s) bilateral rupture in east-southeast and west-northwest directions away from the hypocenter is observed, leading to a nearly simultaneous activation of the source regions of the two phases $S1$ and $S2$.

The $S1$ source is activated down-dip the hypocenter, extends in a small stripe of almost 100 km downward toward the coast and lasts for almost 60-75 s, slightly deepening as time goes on. In the same time window, the propagation is dominantly upward along the slab interface, toward the oceanic trench. The phase $S2$ seems to be associated with a distinct source, produced by the delayed rupture of an about 15 km deep, strong asperity, generating large slip amplitudes at shallow depths. Also $S2$ source deepens between 45 and 90 s, breaking an adjacent stripe northward the hypocenter. The breaking of the $S2$ asperity near the ocean bottom has subsequently triggered the almost unilateral rupture propagation to the southwest, in a direction parallel to the trench. During this stage the rupture propagated along a distance of about 300 km from $S2$ at a higher rupture speed (~ 3 km/s).

A third source, $S3$, then radiated close to the southern limit of rupture zone and at a greater depth than $S1$ and $S2$. Finally, the rupture came to arrest at this deeper part of the slab, and the total rupture duration was about 160 seconds.

In terms of moment release, 70% of the total seismic moment has been released in a relatively small area of 150x150 km near the hypocenter, covering just about 30% of the total ruptured area. Separate moment magnitudes for the three sources $S1$, $S2$, and $S3$ are M_w 8.1, M_w 8.4, and M_w 8.2, respectively. The peak slip rates are 0.9 m/s at $S1$, 1.3 m/s at $S2$, and 1.5 m/s at $S3$. The rupture duration of each source is about 60 s, and evidence of repeating slip of the source $S1$, has been found by Maercklin et al. (2012), consistently with what has been found by Lee et al. (2011) using teleseismic, local seismic and geodetic data.

EARLY MAGNITUDE ESTIMATE FOR THE TOHOKU-OKI EARTHQUAKE

2.1 The concept of real-time magnitude estimate

In the framework of Earthquake Early Warning (EEW) applications, among the real-time operations, the magnitude estimate is one the most critical issues. Event detection, location, ground motion prediction and alert notification are essentially practical problems, related to the development of reliable and efficient algorithms. On the contrary, since the rupture process of earthquakes has not yet been fully understood, the magnitude estimate represents an unsolved, conceptual issue, as well as a complex problem from a practical point of view. The computation of magnitude requires the knowledge of the average slip on the fault plane and of the extension of the plane itself. One should therefore wait until the rupture propagation has finished to measure the final quantities of the whole process.

In Earthquake Early Warning Systems (EEWS) the early portion of recorded signals is used to characterize the final size of the event. The magnitude estimate is based on empirical relationships between the earthquake size and parameters measured in the early portion of P- and S-wave trains (see Box 2.1). For small-to-moderate events (up to $M \sim 7$), the fracture process is concluded within a few seconds

and therefore there are no concerns on the effectiveness of EEWs for the real-time magnitude prediction. In the case of large earthquakes ($M > 7$), instead, the magnitude estimates are done during the early stage of the fracture process, while the rupture is still ongoing. The behaviour of the rupture may be rather complex, in terms of space-time evolution and of frequency dependency, as it was found in the case of the Tohoku-Oki earthquake (Chapter 1). Whether and how the final magnitude can be predicted in real-time, while the source complexities are unknown, is an open debate.

Beyond the theoretical aspects, the ability to correctly distinguish a small shock from a large event from the first observations is a crucial feature of an EEWs and plays a key role in the rapid assessment of the earthquake's damaging potential.

2.2 Evidence for the parameter saturation

Among the empirical scaling relationships which are generally used for EEW applications, one of the most stable and robust correlation is the observed scaling between the initial peak ground displacement (P_d) (measured within 3 seconds from the P-wave arrival) and the final Peak Ground Velocity (PGV), at each recording site (Wu and Kanamori 2005b; Wu and Kanamori 2008a; Wu and Kanamori 2008b; Zollo et al. 2010, see also Box 2.1 for the parameter definition). We analyzed 546, 3-component strong-motion accelerometer records for the Tohoku-Oki earthquake, in the distance range R 120 ÷ 530 km from the epicenter. We measured P_d in a 3-second P-wave Time Window (hereinafter PTW) and studied its correlation with the final PGV , as it is usually done for this two parameters.

The top-left panel of Figure 2.1 shows the observed values of P_d and PGV with respect to the scaling relationship of Zollo et al. (2010). For this earthquake, all data points significantly depart from the expected trend. The PGV values are measured along the entire signal and

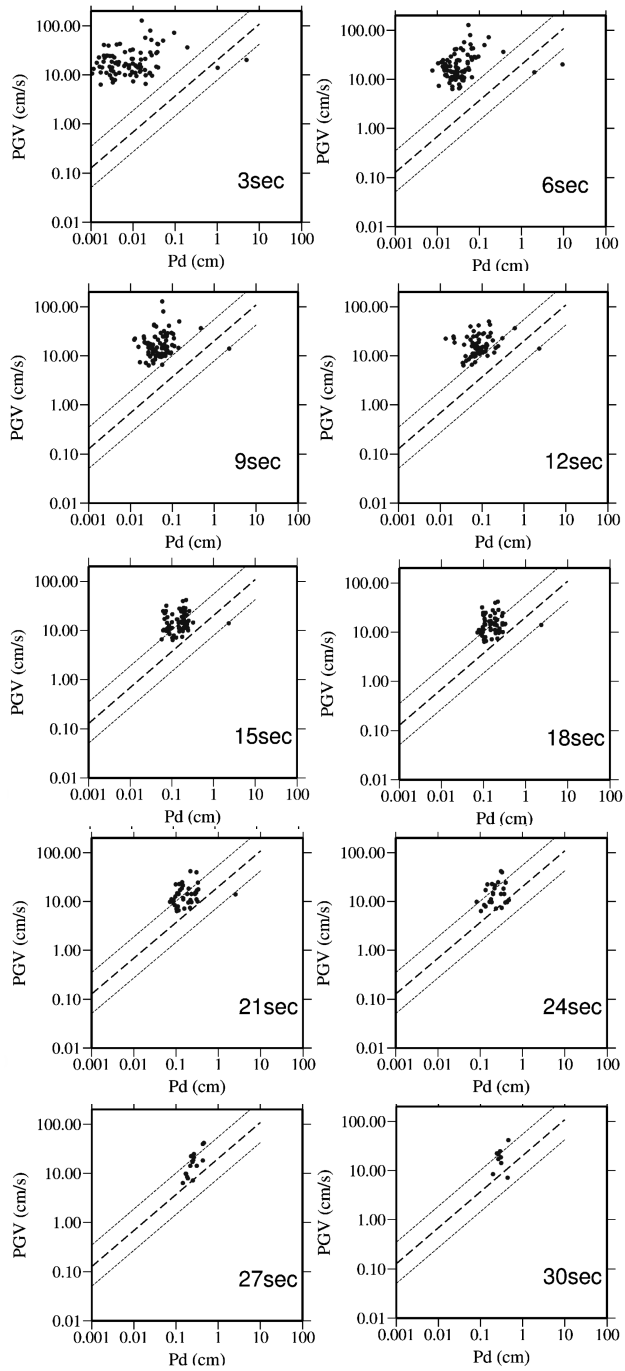


Figure 2.1: P_d vs. PGV for different PTWs. The figure shows the observed values of P_d vs. PGV for different P-wave time windows, with respect to the expected trend, as proposed by Zollo et al. (2010).

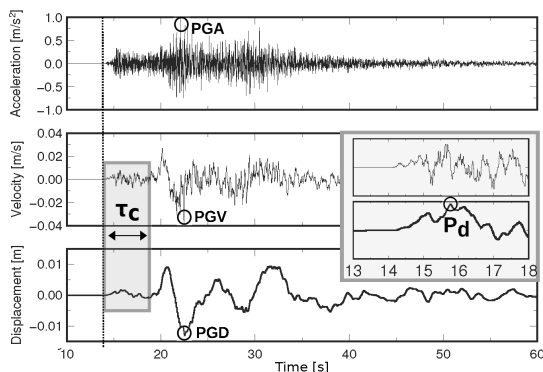
therefore do not depend on the time window adopted. On the contrary, the P_d values, measured within a 3-second time window, are much smaller than those expected for this event. However, as the PTW increases, P_d values increase and all data points progressively move toward the expected trend. Finally, when a 24-second PTW is used, most of data are consistent with the trend.

It is worth to note that the number of data points decreases as the time window increases. Since the empirical relationship between P_d and PGV is calibrated using P-wave data only, it is important to avoid the S-wave contamination while increasing the PTW. To this aim, we computed the theoretical S-wave arrival times at all the stations and excluded from our analysis those for which the estimated S-wave arrival occurred within the considered PTW. While expanding the PTW, the closest stations are thus excluded one by one during the analysis.

The previous observation is a direct evidence for the saturation effect of EEW parameters for large earthquakes. The saturation is a well known problem and has been extensively discussed among literature (Kanamori 2005; Rydelek and Horiuchi 2006; Rydelek, Wu, and Horiuchi 2007; Zollo, Lancieri, and Nielsen 2007). It is due to the use of a few seconds of the P-wave which cannot capture the entire rupture process of a large earthquake (Festa, Zollo, and Lancieri 2008). Longer PTWs are required to characterize the size of a large event.

Box 2.1: EEW parameters and scaling relationships

Zollo, Lancieri, and Nielsen (2006) showed that the low-pass filtered, peak displacement amplitude of initial P- and S-wave signals correlates with the earthquake magnitude. The initial peak amplitude (P_d) can be measured on the single vertical component or on the modulus of the displacement vector. In both cases the functional dependence of the peak amplitude follows a general attenuation relationship of the form:



$$\log(P_d) = A + B \cdot M + C \log(R) \quad (2.1)$$

where M is the magnitude, R the distance and A , B and C are coefficients derived through a best-fit regression analysis. Hereinafter we will adopt the initial P-peak amplitude of the vertical component and will refer to it as P_d .

An alternative magnitude estimate can be obtained using period parameters, which are pretty independent on the distance. Kanamori (2005) defined the Average Period (τ_c) of the first seconds of P-wave signal as:

$$\tau_c = 2\pi \cdot \sqrt{\frac{\int_0^{\tau_0} u^2(t) dt}{\int_0^{\tau_0} \dot{u}^2(t) dt}} \quad (2.2)$$

where $u(t)$ is the ground displacement and τ_0 is usually set at 3 seconds after the arrival of the P-wave. By measuring τ_c in seconds Zollo et al. (2010) determined the relationship between the Average Period and magnitude. They found:

$$\log(\tau_c) = 0.21 M - 1.19 \quad (2.3)$$

The gray box in the above figure shows the initial portion of P-wave signals on velocity and displacement records, which are used to measure P_d and τ_c .

In addition to the event magnitude, the estimate of the expected ground shaking at target sites is another relevant piece of information to be provided in real-time. To this aim, by measuring PGV in cm/s and P_d in centimeters, Zollo et al. (2010) obtained an empirical relationship:

$$\log(PGV) = 0.73 \cdot \log(P_d) + 1.3 \quad (2.4)$$

which allows estimating the expected shaking at each site, once that the initial displacement amplitude is measured.

2.3 Suitability of the existing methodologies

The existing methodologies and the empirical regression relationships which are currently adopted for EEW applications may not be suitable for such giant events. Their validity, indeed, is limited to certain conditions, which we briefly summarize below:

- the empirical regression laws relating EEW quantities and source parameters were derived and validated using databases limited in magnitude (up to M 7-7.5; Allen and Kanamori 2003; Olson and Allen 2005; Wu and Kanamori 2005a; Wu and Kanamori 2005b; Wu and Kanamori 2008b; Zollo et al. 2010), which are well below the $M = 9$ value of the Tohoku-Oki event;
- the coefficients of the regression relationships were calibrated using the initial amplitude in a fixed P-wave time window of 3-4 seconds. The coefficients may not be suitable for longer PTWs and a re-calibration of the empirical relationships could be necessary;
- the regression relationships among EEW parameters and source parameters have been generally applied up to 50-60 km of hypocentral distance, approximately covering the area in which the damaging effects of a moderate-to-large earthquake are expected. Such a distance range is too restricted for the Tohoku-Oki earthquake, that was felt as "very strong" up to about 300 km from the source (Hoshihara et al. 2011).
- for real-time applications a causal 2-pole Butterworth, high-pass filter with a cut-off frequency of 0.075 Hz is usually applied to remove undesired long-period trends and baselines introduced by double integration (Boore, Stephens, and Joyner 2002). While removing the artificial distortions, the filter also reduce the low

frequency content of the recorded waveforms and may change the scaling between early measurements and the final magnitude. Zollo et al. (2010) have shown that this cut-off frequency preserves the scaling of the EEW parameters with magnitude in a broad range ($M 4 \div 7$). Whether the scaling is preserved for giant earthquakes has not yet been verified.

Our first purpose is thus to investigate the reliability of existing EEW methodologies and empirical regression relations for the Tohoku-Oki earthquake.

2.4 Preliminary analysis

We performed a preliminary study to evaluate the joint effect of the high-pass filtering and of the expansion of the PTW on the Tohoku-Oki records. In particular, we measured two EEW parameters, the initial peak displacement (P_d) and the average period (τ_c) (see Box 2.1). Acceleration waveforms are single and double integrated to get velocity and displacement respectively and the high-pass filter is finally applied after the double integration.

We selected some sample accelerograms (spanning the whole analyzed distance range) and tested 80 combinations of cut-off frequency and PTW, from 0.001 Hz to 0.07 Hz and from 3 to 30 s, respectively (Table 2.1). As previously explained, while expanding the time window, those stations for which the estimated S-wave arrival occurs within the considered PTW have been excluded one by one during the analysis. Furthermore, in order to compare the average P_d values for different

	PTW (s)	3	6	9	12	15	18	21	24	27	30
Freq. (Hz)	0.001	0.003	0.005	0.007	0.01	0.03	0.05	0.07			

Table 2.1: List of different P-wave time windows and cut-off frequencies used.

stations, these have to be corrected for the geometrical attenuation effect. Using an independent dataset of Japanese, Taiwan and Italian earthquakes (3552 records corresponding to 296 events in the range of magnitude $4 < M < 8.4$ and distance $R < 200$ km) and through a linear regression analysis, we derived the coefficients of the following attenuation relationship:

$$\log P_d = -3.59 (\pm 0.09) + 0.73 (\pm 0.091) \cdot M - 1.14 (\pm 0.05) \cdot \log R \quad (2.5)$$

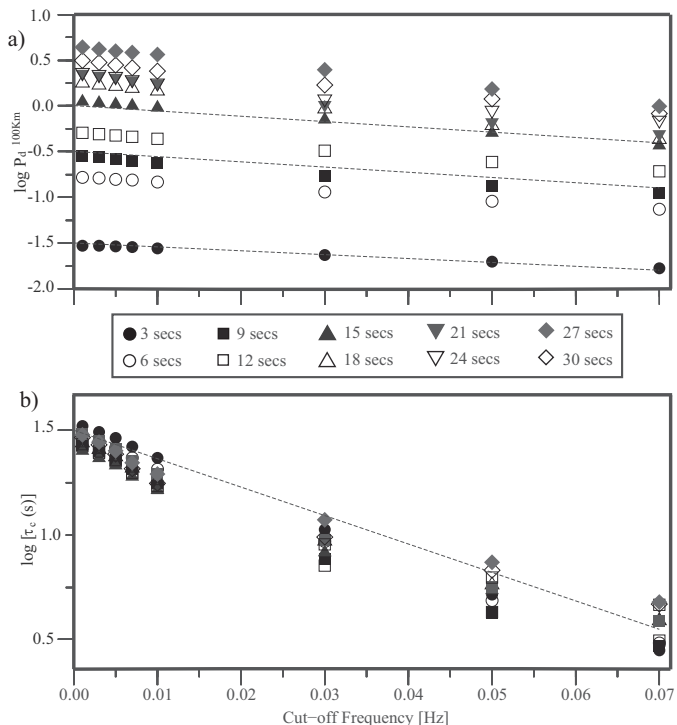
where P_d is measured in centimeters, M is the magnitude and R is the hypocentral distance in kilometers. These coefficients were used to correct the displacement for the distance effect and to normalize all the measured values to a reference distance of 100 km.

Figure 2.2a,b shows the average P_d and τ_c values as a function of the cut-off frequency for different PTWs. $\log(P_d)$ and $\log(\tau_c)$ show a similar trend with frequency: for both parameters, the greatest values are associated to small cut-off frequencies and large PTW. Both parameters almost scale linearly with the cut-off frequency for each considered time window. This behaviour suggests that, independently from which filter is adopted, $\log(P_d)$ [or $\log(\tau_c)$] may be used for estimating the magnitude, provided that the proper scaling coefficients are obtained from the data. For the sake of uniformity with previous works and since the empirical relationships used in this work have been obtained with a 0.075 Hz cut-off frequency, we decided to maintain this value for the filtering operation.

2.5 Expanding the P-wave Time Window

Once we have established the cut-off frequency to be used, we measured the EEW parameters using different PTWs, from 3 to 60 s for all the available records, with the same procedure as discussed above. The purpose is now to understand whether the problem of magnitude underestimation due to the parameter saturation may be overcome

Figure 2.2: Average P_d and τ_c values as a function of cut-off frequency and PTW. $\log(P_d)$ (a) and $\log(\tau_c)$ (b) generally increase with long PTWs and decrease with high cut-off frequencies. For both parameters, the trend with frequency is almost linear and is approximately represented by the dashed lines. [After Colombelli et al. 2012a.]



using appropriate PTWs and if the empirical regression relations relating EEW parameters and magnitude are still valid for this event. The saturation effect on P_d and τ_c measurements in short PTWs is well evident from data. Figure 2.3a,b shows the mean value and standard deviation of P_d and τ_c within progressively increasing time windows measured after the first P-arrival. Again, data possibly contaminated by the S-wave arrival have been excluded and the P_d estimates have been corrected for the distance effect, according to Equation (2.5). As for the peak displacement (Figure 2.3a), it regularly increases with the PTW, reaching a plateau at about 25-30 s, this corresponding to hypocentral distances greater than 240 km. From equation (2.5), the mean value of magnitude for $\text{PTW} \geq 30 \text{ s}$ is $M = 8.4 \pm 0.2$. The average period (Figure 2.3b) shows a similar behaviour although the errors on measurements at each PTW are much larger than those found for the peak displacement. τ_c increases with the PTW and becomes constant

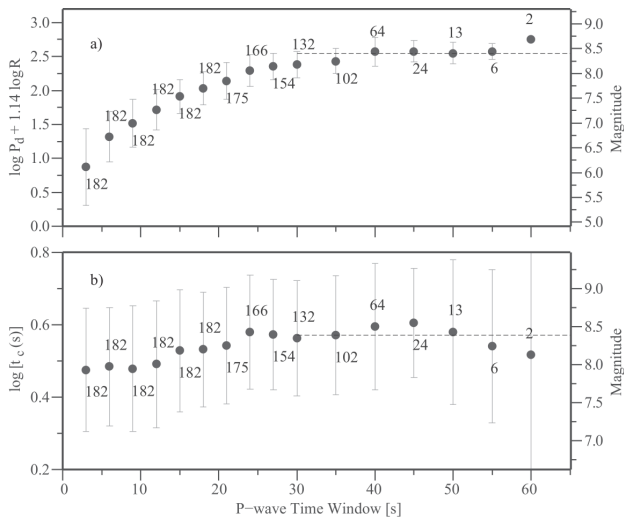


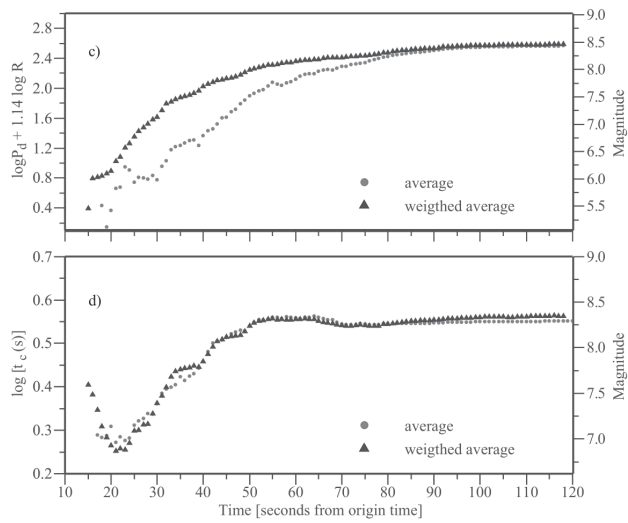
Figure 2.3: Average values of P_d (a) and τ_c (b) as a function of the PTW. Error bars are the standard deviation associated to each value; the gray number close to each point is the number of stations used for each time window. For each plot, the corresponding magnitude scale (from Equations 2.5 and 2.3) is also represented. The final saturation level (PTW ≥ 30 s) is shown by the gray dashed lines. [After Colombelli et al. 2012a.]

after 25-30 s at a mean value which again corresponds to $M = 8.4 \pm 0.2$ according to Equation 2.3. In both plots, error bars represent the standard deviation associated with each value; they depend on the scatter of the measurements but also on the number of observations, which decreases with increasing PTW. The final values of magnitude estimated from P_d and τ_c are consistent within error bars, suggesting that more robust estimations can be obtained by the combined use of amplitude and period parameters.

2.6 Real-Time Analysis

The available PTW at each time step and recording site depends on the P-wave propagation and on the apparent velocity through the seismic network. To use our approach in real-time EEW applications, we reordered P_d and τ_c measurements as a function of time from the event origin time, as it is usually done in EEWS. While maintaining the idea of the expanding PTW, we considered the delayed P-wave arrival time as a function of distance. In the previous analysis we used the same

Figure 2.4: Real-time evolution of P_d (c) and τ_c (d) as a function of time from the origin time. In each plot, gray circles are the standard average values while triangles are the result of the weighted average computation. Each weight is proportional to the square of the PTW. For each plot, the corresponding magnitude scale is also represented. [After Colombelli et al. 2012a.]



PTW for all the stations; here, instead, we use the maximum PTW available for each triggered station, i.e., the time interval between the observed P-wave arrival time and the theoretical S-wave arrival time. In this way all the stations contribute to the measurement, with shorter PTWs for nearby stations and longer PTWs for more distant stations. Results obtained from this analysis are plotted in Figure 2.4a,b (gray circles) and show that the general trend of average P_d and τ_c is similar to that of Figure 2.3a,b, both parameters providing evidence for saturation around 50 s from the origin time.

A possible risk when averaging values resulting from windows with different lengths is that stations with short PTWs can provide a magnitude underestimation, thus affecting the mean value. In order to reduce this effect, at each considered time step we computed the weighted averages of P_d and τ_c , with a weight proportional to the square of the window length (dark triangles). With this approach, we found a significant increase of the initial average values of P_d , while the effect is less evident on τ_c , being probably hidden by the intrinsic larger variability of this parameter. As expected, when a few number of stations (all with short P-wave time windows) is considered, there is no clear

difference among average and weighted average. As the number of stations increases, the difference becomes more evident. In both cases, however, the final average magnitude values are consistent with the results of the off-line analysis.

2.7 Discussion

The evolutionary estimate of P_d and τ_c as a function of the PTW showed that the existing methodologies and regression relationships commonly used for EEW applications can be extended even to the giant Tohoku-Oki earthquake, provided that appropriate time and distance windows are selected for the measurements. We found that P_d and τ_c are indeed largely underestimated when a small PTW is used (a few seconds) while stable and consistent values are obtained for PTW exceeding 25-30 s. Both P_d and τ_c estimate an earthquake magnitude $M > 8$ when using large PTWs (> 25 s), although uncertainties in magnitude estimate from P_d (± 0.3) are significantly smaller than the uncertainties from τ_c (± 1.0).

As for the magnitude estimate, both P_d and τ_c exhibit a saturation effect and provide a magnitude value of $M = 8.4$. Since the final earthquake magnitude is 9.0, does this smaller value reflect the magnitude of the early portion of the event or is it an artefact due to uncertainties in the empirical regression laws and/or to measurement procedures?

As discussed in Chapter 1, kinematic inversions for this earthquake have shown a complex frequency dependent rupture history, with asperities radiating energy with different frequency content at different locations. The three principal peaks of the moment rate function have been interpreted as different slip episodes. The observed parameter saturation beyond 30 s probably corresponds to the end of the first rupture episode. Since the second rupture episode appears to be deficient in high-frequency (>0.05 Hz) energy radiation, we therefore suggest

that the 0.075 Hz high-pass filter used for the evolutionary estimate of P_d and τ_c captured the energy from the first event while filtering out the prominent energy emitted from the second one, thus leading to a smaller magnitude (8.4), when compared to the final earthquake size. For the practical real-time implementation of our methodology, we proposed the use of the maximum PTW available for each triggered station, i.e. the time interval between the observed P-wave arrival time and the theoretical S-wave arrival time. We correct the underestimation of magnitude due the inadequacy of the PTW considered, based on the weighted average computation of both parameters.

This study suggests that records at distances up to several hundred kilometers from the earthquake epicenter help in constraining the magnitude estimate obtained from near-source data. However, the maximum distance to be considered needs to be properly defined as a function of the signal-to-noise ratio, which decreases with epicentral distance and event size. Automatic selection of the proper PTW can be achieved, for example, by increasing the PTW until both P_d and τ_c parameters stabilize, i.e., until no significant variations are observed. In order to account for the uncertainties on P_d and τ_c , appropriate strategies to combine these two parameters could be adopted, such as Bayesian probabilistic approaches as proposed by Lancieri and Zollo (2008). Furthermore, an initial location of the hypocenter is required, in order to correctly estimate the S-wave arrival time, and to exclude data at stations for which the S-waves are expected to arrive within the selected PTW.

PART II

FROM THE OBSERVATIONS TO A PHYSICAL MODEL FOR THE RUPTURE BEGINNING

In the previous chapter we introduced an evolutionary approach for the rapid magnitude estimate, based on the progressive expansion of the P-wave time window. The methodology has been applied to the single Tohoku-Oki earthquake and has provided evidence for the Early Warning parameter saturation in a 3 second time window. While for small-to-moderate earthquakes several authors have shown that such a time window is enough for a correct evaluation of the size, for this magnitude 9.0 event, a minimum time window of 25-30 seconds is needed to get stable magnitude estimates.

In light of this result, relevant conceptual questions immediately arise: is there a minimum time beyond which the final magnitude of an earthquake can be predicted? If this time does exist, is it related to the physics of the rupture process?

In this part of the thesis we explore the evolutionary approach, based on the expansion of the P-wave time window, using a larger number of earthquakes, including small, moderate and also large events. We analyze the time evolution of two Early Warning parameters (the initial peak displacement amplitude and the average period), measured along the initial portion of P-wave signals. Our purpose is to understand

*whether their time evolution is related to the rupture process and to develop a physical model to justify the observed behaviour of these parameters.*¹

¹The analyses presented in the following two chapters are extracted from: Colombelli, S., Zollo, A., Festa, G. and Picozzi, M. Small and large earthquakes: evidence for a different rupture beginning, submitted to *Nature Communications*.

TIME EVOLUTION OF EARLY WARNING PARAMETERS

3.1 Database description and method

Most of the previous studies on the beginning of waveforms analyzed either few earthquakes recorded at a limited number of stations or earthquakes belonging to the same sequence. In such conditions, it can be difficult to recognize and clearly discriminate between source and propagation effects which can both influence the initial shape of signals. In this study we used a larger, high-quality, dataset of 43 moderate-to-strong Japanese events, spanning wide magnitude and distance ranges ($M 4 \div 9$; $R 0 \div 500$ km). We analyzed a total of 7514, 3-component waveforms, recorded at 1208 stations. The data set includes different types of fault mechanism with events that are distributed in depth between 5 and 60 km. Among the 12 earthquakes with $M \geq 6.0$ we included the 2003, $M8.0$ Tokachi-Oki event and the 2011, $M9.0$ Tohoku-Oki mega-thrust earthquake. The full list of analyzed events is provided in Table A.1. Figure 3.1a shows the stations used and the epicenters of the selected events; data histograms and distributions are shown in panels b,c,d.

We manually picked the P-wave onset time on each vertical component of accelerometer records. A total number of 13.841 waveforms have been manually picked. The displacement waveforms are obtained from acceleration records through a double integration operation and a high-

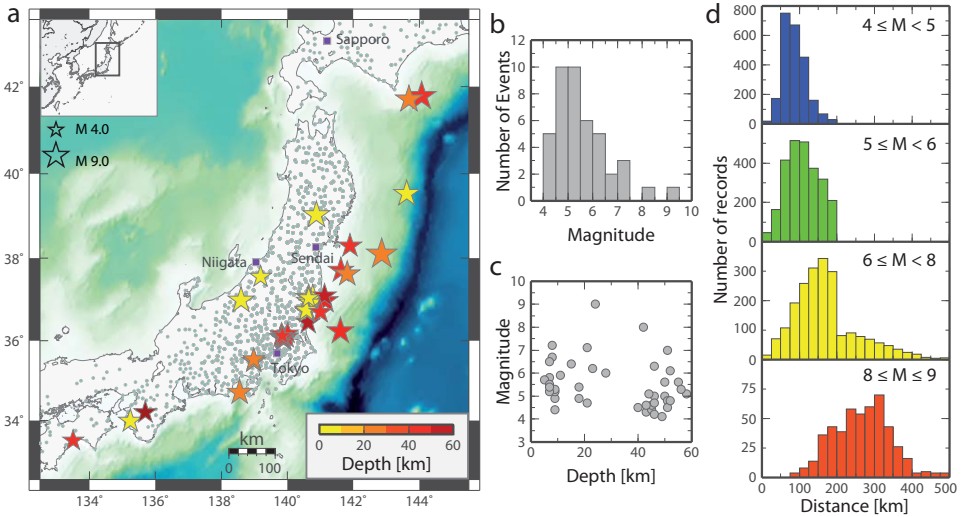


Figure 3.1: Event map and data histograms. (a) The map shows the distribution of stations used in this study (small green circles) and the epicentral location of the 43 selected events (coloured stars). The size of the star is proportional to the magnitude and the color represents the source depth. (b) histogram of the number of earthquakes as function of magnitude. (c) distribution of magnitude as a function of depth for the selected events. (d) distribution of records as a function of distance for different magnitude classes.

pass filter, with a 0.075 Hz cut-off frequency. Following the approach proposed in Chapter 2, we measured the peak displacement amplitude on the filtered P-wave signals (P_d) and the average period (τ_c) over progressively expanding PTWs, starting from 0.05 s after the P-wave onset time and until the expected arrival of the S-phase. For each event we obtained the logarithm of P_d vs. PTW curve (hereinafter LPDT curve) and the logarithm of τ_c vs. PTW curve (hereinafter LTCT curve) by averaging all the available data at each time window (typically more than 100 records). Before computing the average, the observed P_d values at different stations have been corrected for the geometrical attenuation effect. For earthquakes with $M < 7$ we used only data up to a maximum hypocentral distance of 200 km, while for $M \geq 7$ events we included records up to 500 km. The computation is

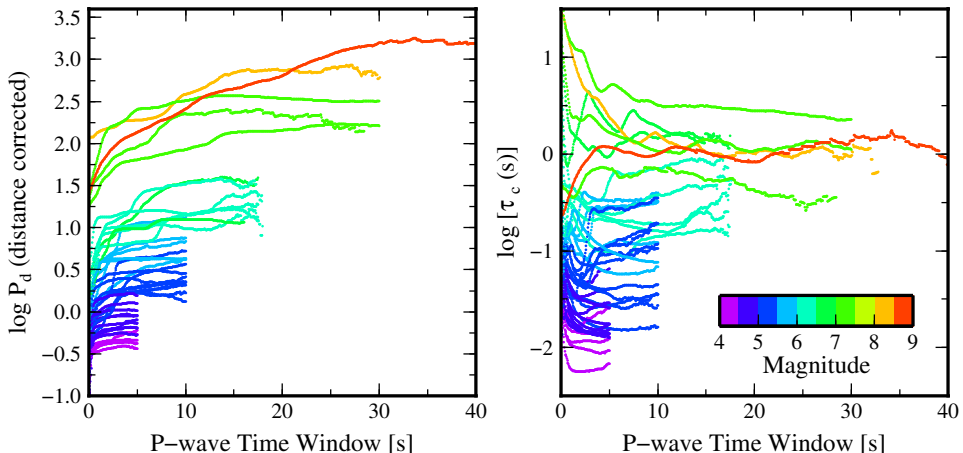


Figure 3.2: Average LPDT and LTCT curves for all analyzed events. The color scale represents the event magnitude and the P_d values have been corrected for the distance effect, before computing the average.

stopped when less than 5 stations are available in the PTW, or when the PTW reaches a prior determined time limit, whichever condition occurs first. To avoid the S-wave contamination when increasing the time window, we excluded from the average all the stations for which the expected S-wave arrival time occurs within the considered PTW. Other details of data processing are provided in Section A.2.

3.2 P_d and τ_c vs. time: overall results

Figure 3.2 shows the LPDT and LTCT curves for each of the analyzed event. The visual inspection of the curves reveals the main features of the two parameters, which are briefly discussed below:

- both for P_d and for τ_c , the shape of the curves is similar for all the events, independently on the magnitude;
- both for P_d and for τ_c , the mean level of the whole curve increases with increasing magnitude;

- for all the analyzed events the LPDT curve starts from small values and then progressively increases with time until a final, stable value is reached. The final plateau level generally increases with magnitude;
- the LTCT curves do not show a clear time dependence. The mean value of each curve generally increases with magnitude, but an unstable behaviour with time is observed;
- a short, unstable initial phase (i.e., few seconds) on the LTCT curves is observed. Since the period parameter is computed as a finite integral over a time window, this unstable behaviour could be related to the computation process.

3.3 P_d vs. time: a deeper look at the curve

From the plots of Figure 3.2, it appears evident that both P_d and τ_c carry information on the event size. Among the two parameters the peak displacement amplitude has a clear and stable time evolution, while the period parameter shows an unstable behaviour, difficult to interpret. Since our goal here is to understand if these two parameters are related to the rupture process, we will therefore focus the stable P_d parameter for the following analysis.

A deeper look at the P_d evolution allows to identify three distinct parts on the LPDT curves: an initial increase, a final plateau level and an intermediate, transition part among these two. To reproduce the observed shape we modelled the LPDT curves using a piecewise linear function (Figure 3.3), which is the simplest model to fit the whole curve, while keeping the three distinct parts.

For each event we fit the data and determined 5 parameters: the corner time of the first and second straight line (T1 and T2, respectively), the slope of the two lines (B1 and B2, respectively), and the final plateau

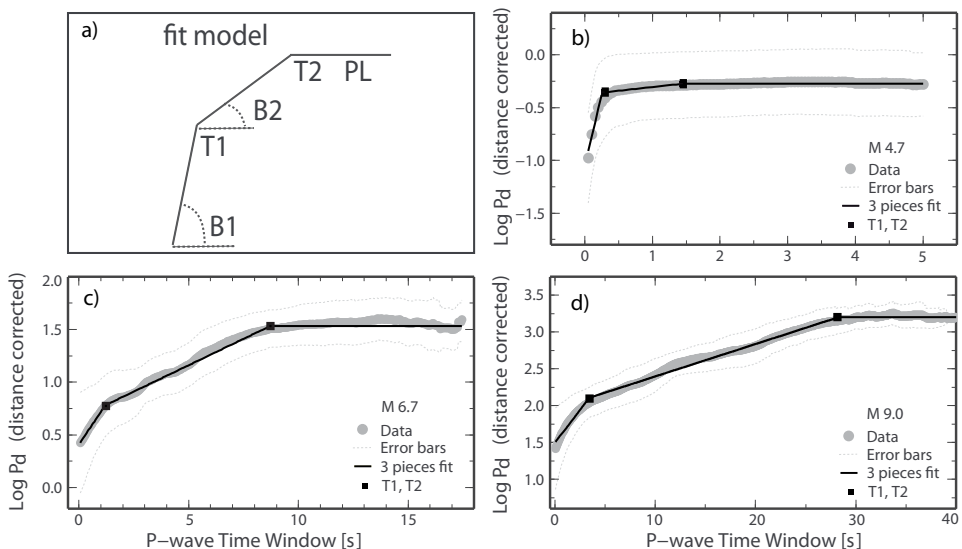


Figure 3.3: Fit model and example of LPDT curve for three representative events. (a) schematic representation of the piecewise linear fitting function. (b,c,d) Example of LPDT curve for three representative events. The y-axis represents the average of logarithm of P_d , obtained by using all the available data at each time, after correcting individual values for the distance effect (Equation A.2 of Supplementary Information). Gray circles are the observed data with the associated $\pm 1\sigma$ error bars (dashed lines). The solid line is the best fit function and the dark squares mark T1 and T2 times.

level (PL). Examples of fitted curves for three representative events are shown in Figure 3.3.

We then looked at the scaling of the fit parameters with magnitude to find out similarities or differences among the events. While doing that, we also identified different factors that might have influenced the shape of the LPDT curves. The earthquake depth, for example, may impact source processes and frictional properties, thus affecting our observation about the evolution of P-wave peak displacement with time. Among the other factors, the high-pass filtering operation and the propagation effects related to crustal structure, geometrical spreading and anelastic attenuation are the most relevant. We performed different tests and separately investigated the influence of these factors on

the analysis (see Section [A.3](#)). We did not find any clear evidence that neither the source depth nor the other effects are responsible for the observed trends of fit parameters with magnitude.

PEAK DISPLACEMENT AMPLITUDE VS. TIME: OBSERVED TREND, SCALING AND PHYSICAL INTERPRETATION

4.1 Scaling of T2, B2 and PL with magnitude

For a single station, the far-field source kinematic models indicate that the P_d vs. time curve reproduces the shape of the apparent source time function (Aki and Richard 2002). By averaging P_d among many stations, distributed over azimuth and distance, the resulting function approximates the Moment Rate Function (MRF).

We found that T2 and PL scale with magnitude (Figure 4.1), which is an a posteriori validation of the hypothesis that averaged LPDT curves approximate the MRF. The observed scaling of T2 with magnitude suggests that the saturation time of LPDT curves can be also used as a proxy for the source duration. Assuming that the LPDT curve approximates the MRF, we would expect T2 to be comparable to the half duration of the source. The immediate implication, is that the measurement of T2 can provide an approximate estimate of the extension of the source. In the context of EEW applications, this can be a relevant piece of information to provide, although further considerations about the use of the LPDT curves for EW purposes are discussed

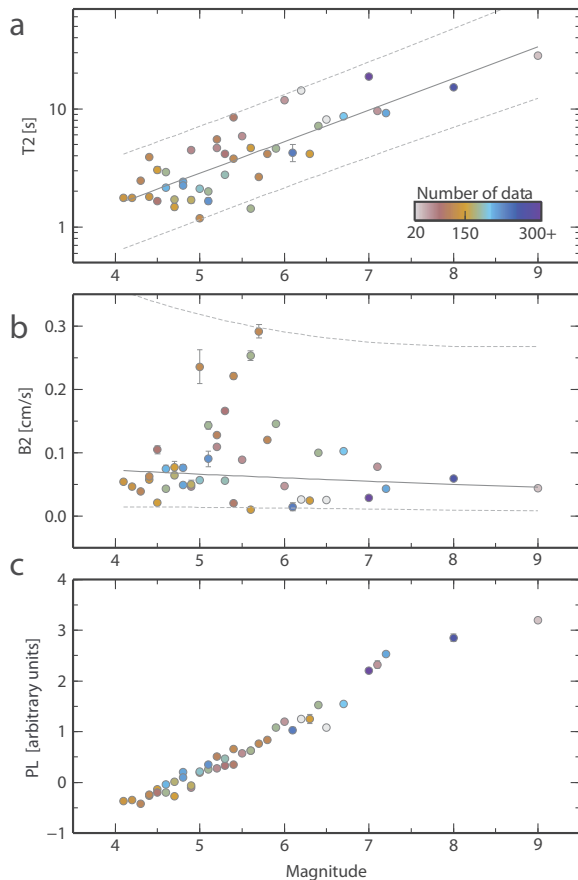
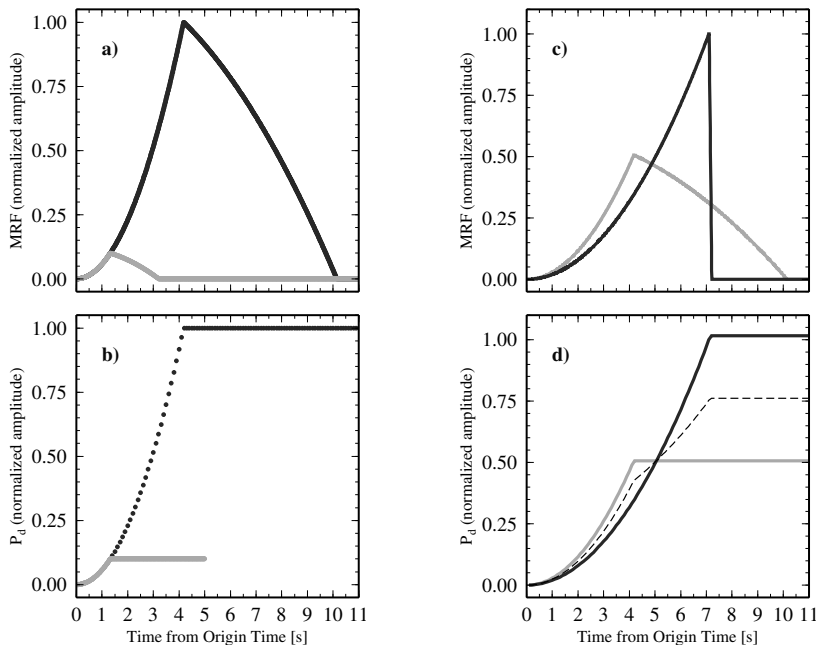


Figure 4.1: Fit parameters T_2 , B_2 and PL vs. magnitude a) Second corner time of the linear piecewise fit model (T_2), in a log-linear scale. b) Slope of the second line piece of the fit model (B_2) as a function of magnitude for all the analyzed events, in a linear scale. c) Saturation level (PL) of the LPDT curve for each event. The saturation level is measured at the time T_2 . In each plot, the color scale indicates the number of data used for the average computation at the time T_2 . In panels a and b, the solid gray line shows the linear best fit function and the thin dashed lines are the 95% confidence interval for new observations, given the existing fit to the data. Error bars on individual data points are also shown in the plot (only the largest errors are visible).

in Section 4.5.

While the scaling of T_2 and PL with magnitude is evident from the plot, the slope of the second line (B_2) does not show any clear trend with magnitude. We did not perform a detailed analysis about the B_2 parameter. However, we can suggest a few hypothesis to explain the observed behaviour. The MFRs are typically modelled using simplified triangular-like functions (Sato and Hirasawa 1973). The real shape of the MFRs can be much more complex and the transition between the initial point and the maximum peak is nothing but regular. The behaviour of B_2 may therefore reflect the irregular shape of this function. Furthermore, the intermediate phase on the LPDT curves could be related to the variability of the peak amplitude, when measured at

stations with different azimuth (see Box 4.1). If this was the case, the B2 slope would depend on the azimuthal coverage of stations, rather than on the event magnitude.

Box 4.1: P_d vs. Moment Rate Function

Let us assume the source model of Sato and Hirasawa (1973) and let us measure the initial peak displacement on this synthetic MRFs, following the same approach as used on the real waveforms. Panel a) shows an example of MRF for two different magnitude earthquakes, at a fixed azimuth. Panel b) shows the resulting P_d vs. time curves. Given the triangular-like shape for the MRFs, the P_d vs. time curves increase as long as the MRFs increase and the plateau of the P_d vs. time curves is reached at the peak of the MRF.

Let us now consider the synthetic MRFs for a fixed magnitude and for two different azimuths (0 and 90°) and the respective P_d vs. time curves (panels c and d). For each azimuth, the shape of curve is the same of panel b). If we compute the average P_d vs. time curve, the shape of the curve is different and an intermediate step appears. Averaging out on a large number of curves at different azimuths, a continuous and smoothed P_d vs. time curve is obtained, which looks like what is observed on real data.

The examples shown in this box have to be intended as a pure clarifying exercise. We adopted a simplified source model which may not be appropriate to describe real events and this is especially true for large earthquakes, for which the complexity of the source cannot be neglected.

4.2 Scaling of T1 and B1 with magnitude

For their possible relation with the rupture process beginning, our main focus is on the initial parameters, T1 and B1. We found a significant log-linear correlation with magnitude for both T1 and B1. In particular, T1 increases with magnitude while B1 is inversely proportional to the earthquake size (Figure 4.2a,b). These results indicate that the evolution of LPDT curve at the early stage of the rupture is to some degree related to the final earthquake size. Figure 4.2c shows the observed LPDT curve up to its T1 time for few representative events and the expected slopes given the B1 vs. magnitude trend (small box). In terms of errors, the individual estimated parameters are remarkably accurate and their scaling with magnitude is robust (linear correlation coefficient, $R^2=0.8$), although a clear variability appears from the plot on the whole dataset.

4.3 Initial slope: analysis at a fixed time window

The most relevant result of this analysis is the observed variation of the initial slope of P_d for different magnitude earthquakes (i.e., the trend of B1 vs. M). Without using any fitting procedure, this result appears evident from a visual inspection of the curves and it is even more evident when comparing the way the initial P_d increases for earthquakes belonging to different magnitude class (Figure 4.2).

However, the use of a 3-piecewise linear function to fit the data might have introduced some bias in the estimation of B1 and T1. We then tested the persistence of the B1 trend for increasing magnitude also by limiting all the LPDT curves to a fixed time window. We selected 1s for $M \geq 6$ and 0.1s for $M < 6$ and for each event, we estimated the initial slope (by fitting data with a single straight line). Figure A.6

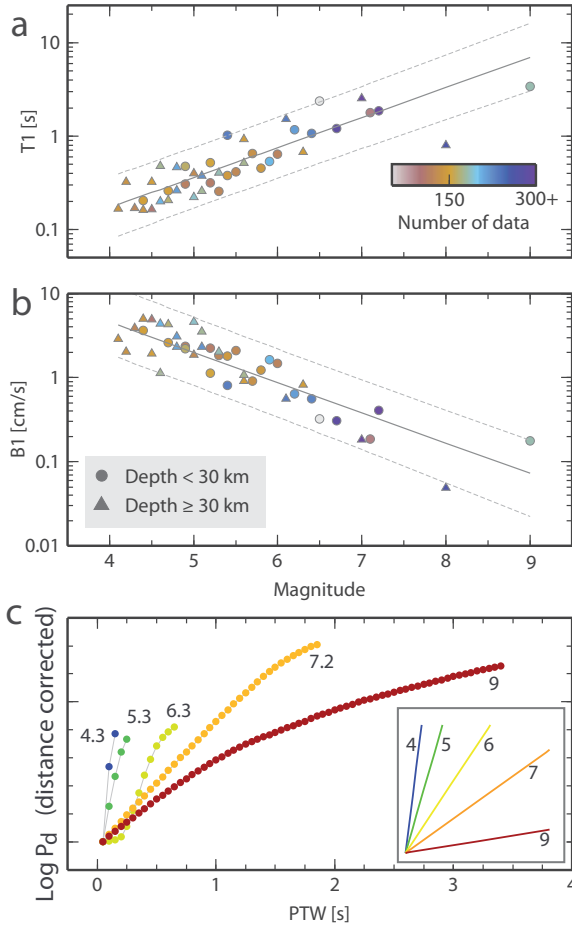
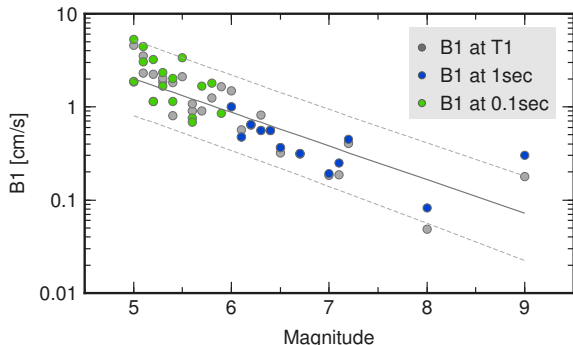


Figure 4.2: Fit parameters T_1 and B_1 vs. M . (a) First corner time of the linear piecewise fit model as a function of magnitude, in a log-linear scale. (b) Slope of the first line segment of the fit model as a function of magnitude, in a log-linear scale. In both panels the color scale indicates the number of data used for the average computation at the time T_1 . The solid gray line shows the linear best fit function and the dashed lines are the 95% confidence intervals for new observations, given the existing fit to the data. Error bars on individual data points are also shown (only the largest are visible). (c) Zoom on the LPDT curve until the time T_1 for some representative events. A common initial value has been assigned to compare the shape of the curves. The insert box shows the expected initial slope of the LPDT curve for different magnitudes, given the observed trend of B_1 with magnitude.

shows that the slope estimates obtained within a fixed time window are consistent with those obtained by fitting the whole curves and that the trend of B_1 with magnitude is still observed when only the very beginning of the curves is considered.

Figure 4.3: Slope estimates within a fixed time window. The slope is obtained using a single linear fit function. For $M \geq 6$ events (blue circles), the slope is measured within 1 second, while for $M < 6$ (green circles) the slope is measured within 0.1 second. Light gray circles are the slopes estimated with the 3-piecewise model, up to the first corner time T_1 .



4.4 A physical model for the rupture initiation

A plausible interpretation for the observed trend of T_1 and B_1 with magnitude is related to differences in the friction during the nucleation phase of earthquakes. The characteristic time for nucleation of large earthquakes is one to few seconds (Beroza and Ellsworth 1996; Ellsworth and Beroza 1995; see also Box 4.1), which is indeed comparable with our estimates of the T_1 time from LPDT curves (Figure 4.2a). Furthermore, our observations indicate that the initial shape of the P_d vs. time curves mainly follows an exponential trend.

The slow stable nucleation phase and its transition to the dynamic earthquake rupture have been deeply investigated by theoretical, numerical and laboratory studies to understand the preparatory phase of earthquakes and the rupture potential to grow into a large event (Kaneko and Ampuero 2011; Nielsen, Taddeucci, and Vinciguerra 2010; Ohnaka 1996, 2000; Ohnaka and Yamashita 1989; Rubin and Ampuero 2009). In the framework of linear slip weakening models, analytical solutions of the nucleation phase indicate that the exponential growth is mainly controlled by the weakening rate (Ampuero, Vilotte, and Sánchez-Sesma 2002; Dascalou, Ionescu, and Campillo 2000), which

is the ratio between the strength drop of the fault related to the friction and the characteristic slip weakening distance (Dc), over which the energy is dissipated.

During the nucleation the initial stress is close to the threshold in the slipping zone. We can therefore replace the strength drop with dynamic stress drop in our interpretation. Observations indicate a decrease of $B1$ of about one order of magnitude in the range $M4.5 \div 7$ (Figure 4.2b). In the same range this would correspond either to a decrease of the initial stress or to an increase of the critical slip distance, both of one order of magnitude.

Far-field measurements indicate an unclear scaling, or eventually a weak increase of the stress drop with magnitude in this range (Oth et al. 2010). Although these estimates refer to the whole rupture process, an initial decrease is unlikely to result in a final constant value, independent of magnitude. On the other way round, assuming for Dc a characteristic value of 0.5-1m for a $M = 7$ event (Tinti, Bizzarri, and Cocco 2005), the corresponding value for a $M = 4.5$ would be in the scale of 5-10cm. Extrapolating this value to negative magnitudes, micrometric-to-millimetric values for Dc would be obtained, consistent with the estimates from laboratory experiments. Such a scaling indicates the availability of a larger fracture energy in the initial part of the rupture for larger magnitude events. Additionally, the nucleation size is directly linked to the weakening rate for linear slip weakening models (Uenishi and Rice 2003) and this suggests a larger size and a longer characteristic time of the nucleation of larger events, as confirmed by the positive scaling of $T1$ with magnitude.

Although the observed $T1$ values are comparable to the nucleation times, we cannot exclude that they concern the initial acceleration of the dynamic rupture phase. Therefore, we argue that when an earthquake rupture develops over a region with a low Dc value, its probability to break adjacent regions is low. On the other hand, when

a coherent rupture nucleates in a region of larger Dc the probability to grow into a larger size event becomes larger. In this context, the variation of Dc and of the probability of growing for earthquake initial ruptures, justifies the dispersion of B1 values with respect magnitude.

4.5 Considerations for the real-time applications

The observed variation of the initial slope of LPDT curves with magnitude has a strict relation with the rupture initiation and has immediate, important impact on the rapid assessment of the earthquake size, which is the most crucial issue in the framework of Earthquake Early Warning operations.

For the present work, a careful and detailed analysis has been performed. All the waveforms have been visually inspected and the P-wave onset time has been manually picked, in order to avoid or reduce any noise contamination on the analysis. For each event, hundreds of records, spanning wide azimuth and distance ranges, have been used to reconstruct the shape of LPTD curves, for a total, huge number of high-quality waveforms analyzed.

In real-time working systems, the availability of data depends on the P-wave propagation and on the apparent velocity through the seismic network. In the first seconds after the occurrence of an earthquake, a limited number of data is usually available. The shape of the LPDT curves could be affected by the number and azimuthal coverage of the recorded waveforms. Further analysis, which are beyond the purpose of this work, are hence required to simulate the real-time data streaming and assess the minimum near-source data necessary to constrain the initial slope.

Assuming that the trend of B1 with magnitude does persist when few, near-source data are used, as long as the slope is well constrained from

data, our results suggest that a few seconds (< 3) can be enough for an approximate evaluation of the earthquake size. In particular, the slope estimate within the first second can be used for a first-order discrimination between small earthquakes and potentially large size events.

Box 4.2: The nucleation phase and the slip-weakening model

Laboratory experiments (e.g., Dieterich 1979; Ohnaka 1996) and theoretical models (e.g., Das and Scholz 1982; Dieterich 1986) have shown that failures begin with an episode of slow sliding over a limited region of the fault. This zone is called the "nucleation zone" and is a zone of quasi-static slip and low rate of moment release that precedes the dynamic rupture.

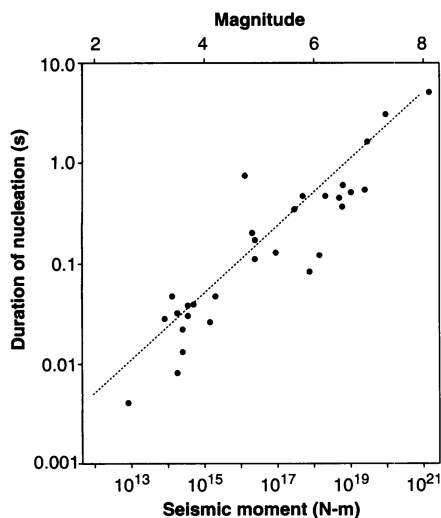


Figure 4.4: Duration of the nucleation phase. The figure shows the duration of the nucleation phase (ν) as a function of the seismic moment (M_0). [After Ellsworth and Beroza 1995.]

the size and the duration of the seismic nucleation phase, indeed, increase with the total seismic moment of the earthquake.

In laboratory experiments, Dc is of the order of millimeters-to-centimeters, while meters are generally found from seismic data.

(continued)

Box 4.2: The nucleation phase and the slip-weakening model (continued)

In the framework of friction laws, laboratory experiments have shown that static friction moves to the dynamic friction in a characteristic dislocation length. These models are generally known as "slip-weakening", since they assume that the friction decreases while slip increases.

In particular, in the linear slip-weakening model (Andrews 1976; Ida 1972, Figure 4.5), slip is zero until the total stress reaches a peak value (yield stress, τ_u). Once this stress has been reached, slip D starts to increase up to a critical slip distance (D_c , labelled as " d_o " in the figure), while the friction coefficient decreases linearly down to the dynamic the value.

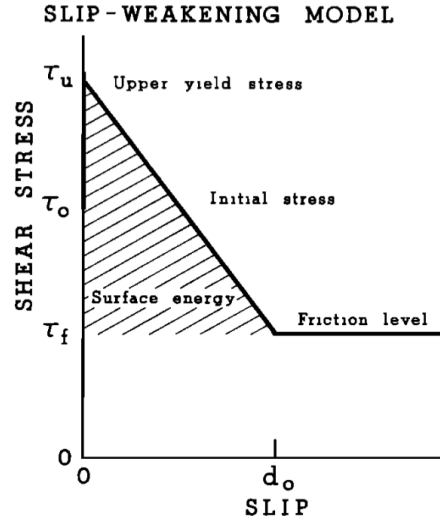


Figure 4.5: Slip-weakening model. [After Andrews 1976.]

Assuming a linear slip-weakening model and using a linearized perturbation analysis, Ampuero, Vilotte, and Sánchez-Sesma (2002) derived the analytical solution of the nucleation of the rupture. The solution indicates an exponential growth of the nucleation phase in its meta-stable phase, with the exponential growth which is controlled by the weakening rate.

In terms of our analysis, the observed LPDT curves suggest that the initial increase of peak amplitude follows an exponential trend. Assuming the model of Ampuero, Vilotte, and Sánchez-Sesma (2002), the initial slope of the curves (B1), has to be related to the slip-weakening rate. To justify the observed decrease of B1 with magnitude, either the initial stress decreases with magnitude, or the characteristic length increases with it.

PART III

REAL-TIME STRATEGIES FOR THE EXTENDED SOURCE EFFECTS

When a large earthquake occurs, an other relevant piece of information to provide in real-time is the expected ground shaking at target sites, for the immediate activation of emergency procedures. If the earthquake rupture extends for hundreds of kilometers and a simple point source is assumed, even if we improve the magnitude estimate, the computation of the source-to-site distance may be inadequate, thus significantly affecting the ground shaking estimate. This is especially true for targets sites that are close to the fault but far away from the epicenter. The standard approaches for the ground shaking prediction, which are based on the solely magnitude estimate, may result in underestimated predictions, thus reducing the effectiveness Early Warning systems. In the following chapters, two different strategies for the ground shaking prediction are introduced.

The first is a threshold-based approach, which integrates the regional and on-site methodologies for Early Warning. It can be used to predict finite source effects, such as directivity and azimuthal variation of the ground motion, without explicitly estimating the size of the fault.

The second approach is based on GPS data and on the inversion for the static slip on the fault plane. This method may provide a rapid es-

imate both of the event magnitude and of the rupture area extension. Both approaches aim at the correct evaluation of the expected ground shaking at the target sites, which is a crucial piece of information to be provided to the end-user audience.¹

¹The analyses presented in the two following chapters are extracted from: Colombelli, S., Amoroso, O., Zollo, A. and Kanamori, H. (2012). Test of a Threshold-Based Earthquake Early Warning Using Japaned Data, *Bull. Seism. Soc. Am.* 102, doi 10.1785/0120110149.

Colombelli, S., Allen, R. M. and Zollo, A. (2013). Application of real-time GPS to earthquake early warning in subduction and strike-slip environments, *Journal Geoph. Res.* 118, doi 10.1002/jgrb.50242.

RAPID ESTIMATE OF THE POTENTIAL DAMAGE ZONE

5.1 The Threshold-Based Approach

The concept of EEWS is today becoming more and more popular in the seismological community, especially in the most active seismic regions of the world. EEWS have experienced a very rapid improvement and a wide diffusion in many active seismic regions of the world in the last three decades (Figure 5.1). They are currently operating in Japan (Nakamura 1984, 1988; Odaka et al. 2003; Horiuchi et al. 2005), Taiwan (Wu and Teng 2002; Wu and Zhao 2006), Mexico (Espinosa-Aranda et al. 2009) California (Allen et al. 2009a,b; Böse et al. 2009) and Romania (Böse, Ionescu, and Wenzel 2007). Many other systems are under testing or development in Turkey (Alcik et al. 2009), China (Peng et al. 2011), Southern Italy (Zollo 2009; Satriano et al. 2010; Zollo et al. 2014), Switzerland and South Korea. Finally, feasibility studies are in progress for Greece, South Iberia region (Carranza et al. 2013), Israel and Eastern Carribean Islands.

Most of existing EEWS essentially operate in two different configurations, *regional* (or network-based) and *on-site* (or station-based), depending on the source-to-site distance and on the geometry of the network with respect to the source area. A regional EEWS is based on a dense network of sensors, covering a portion or the entire area that is threatened by earthquakes, while the targets to be protected

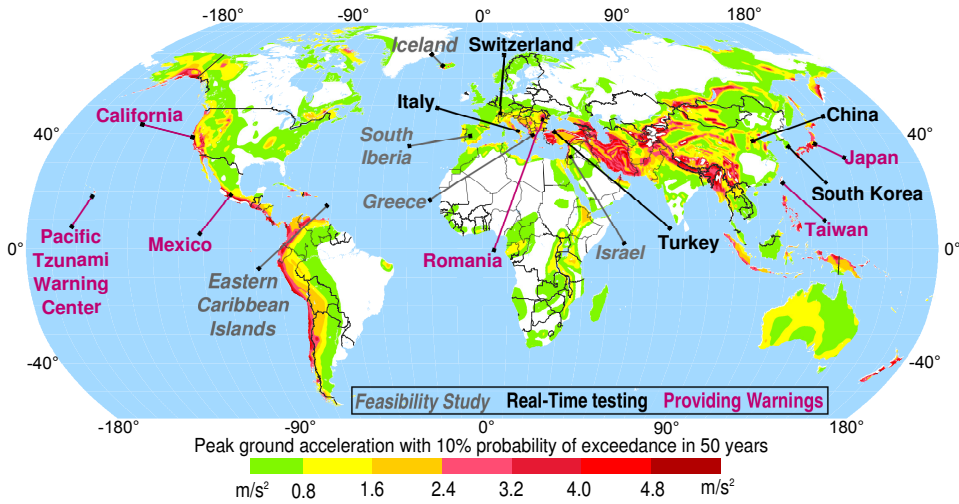


Figure 5.1: Worldwide EEWS. The map shows the distribution of EEWS around the world, with a color indicating the status of the system. In purple, the operative systems, which are providing warnings to public users. In black, the systems which are currently under real-time testing. Gray color is finally used for those countries where feasibility studies are ongoing.

are far away from the source region. In this approach, the relevant source parameters (event location and magnitude) are estimated from the early portion of recorded signals (initial P-waves) and are used to predict, with a quantified confidence, a ground motion intensity measure (e.g., Peak Ground Acceleration, *PGA*, and/or Peak Ground Velocity, *PGV*) at a distant site where a target structure of interest is located, through the use of empirical Ground Motion Prediction Equations (GMPE). Given the source-to-site distance, the “*lead-time*”¹ can be relatively long in a regional configuration, while the prediction of the shaking at distant sites may be affected by large uncertainties, due to the use of empirical predictive relationships.

On-site (or site-specific) EEWS consist of a single sensor or an array of

¹The *lead-time* is defined as the time elapsed between the alert issue and the arrival of damaging waves (S-waves) at the target site. It represents the effective time available to activate security actions and emergency procedures.

sensors deployed in the proximity of the target structure to be alerted. In this configuration the early portion of recorded P-wave signal is used to predict the ensuing peak ground motion at the same site and to provide a local alert level. The main advantage of such an approach is that the alert for an impending earthquake at the target site is based on a local measurement of P-wave ground motion, without using empirical predictive laws and bypassing the estimate of earthquake location and magnitude, which might be affected by large uncertainties in a real-time analysis. In an on-site configuration, however, the *lead-time* is relatively shorter, as compared to the network-based approach (Satriano et al. 2010).

A recent idea for EEWS, proposed by Zollo et al. (2010), is the integration of the two approaches, which allows for accurate estimates of earthquake parameters and reliable predictions of the expected ground motion, while providing sufficient lead-times to the target sites. The "Threshold-Based Approach" is aimed at the definition of local alert levels and at the rapid estimate of the earthquake Potential Damage Zone (PDZ). The basic concepts and equations of the method of Zollo et al. (2010) are first summarized in the following section. Then, a more refined approach for the PDZ definition is proposed and applied to real events.

5.2 Local Alert Level Definition

At each recording station, the initial peak displacement amplitude and the average period are measured along the first 3 seconds of signal, after the P-wave onset time. The measured values of P_d and τ_c are then compared to threshold values (prior established) and a local alert level is assigned at the site, according to a decision table. Four alert levels (0, 1, 2, 3) have been defined based on the combination of P_d and τ_c at a given site (Figure 5.2). The threshold values of P_d and τ_c

correspond to a minimum magnitude $M = 6$ and to an Instrumental Intensity (I_{MM}) equal to *VII*. Thresholds have established using the τ_c vs. M relationship (Equation 5.2), the P_d vs. PGV relationship (Equation 5.1) and assuming that PGV provides an intensity measure, through the conversion table of Wald et al. (1999), see Box 5.1).

Box 5.1: Basic equations of the method

The key element of the method is the real-time, simultaneous measurement of P_d and τ_c in a 3-second window after the arrival time of the first P-wave at accelerometer stations located at increasing distances from the epicenter. In this approach, the initial peak displacement is also used as a proxy for the PGV for a real-time mapping of the most likely damaged area.

Based on the analysis of strong-motion data from Japan, Taiwan and Italy, measuring P_d in centimeters and PGV in centimeters per seconds, Zollo et al. (2010) found:

$$\log(PGV) = 0.73(\pm 0.01) \cdot \log P_d + 1.30(\pm 0.02) \quad (5.1)$$

The period parameter (τ_c) is used to estimate the earthquake magnitude (M). Measuring τ_c in seconds and through a best-fit weighted regression line on average binned data ($\Delta M = 0.3$) with the same data set used before, they found:

$$\log(\tau_c) = 0.21(\pm 0.01) \cdot M - 1.19(\pm 0.08) \quad (5.2)$$

In a standard attenuation relationship, the peak amplitude depends, at the first order, on the hypocentral distance (R) and on the earthquake magnitude. Given the dependency of average period on the earthquake magnitude, equations (5.1) and (5.2) are combined in order to derive a single empirical relationship among P_d , τ_c and R . Measuring R in kilometers, τ_c in seconds, P_d in centimeters, through a multivariate linear regression analysis Zollo et al. (2010) found the following equation:

$$\log(P_d) = 1.93(\pm 0.03) \cdot \log(\tau_c) - 1.23(\pm 0.09) \cdot \log(R) + 0.6(\pm 0.1) \quad (5.3)$$

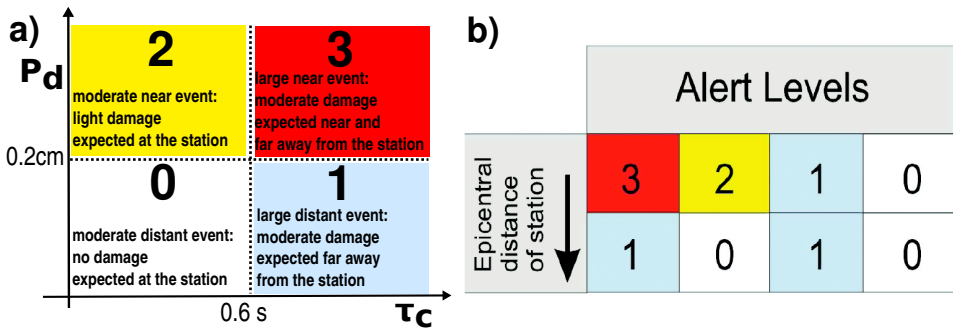


Figure 5.2: Alert level definition. (a) P_d and τ_c diagram showing the chosen threshold values and the regions delimiting the different alert levels. (b) Expected variation of alert levels as a function of the epicentral distance: the allowed transitions between alert levels are from 3 to 1 and from 2 to 0. [After Zollo et al. (2010).]

The alert level scheme comes from an original idea of Wu and Kanamori (2008b) and can be interpreted in terms of potential damaging effects nearby the recording station and far away from it. For example, following the scheme of Figure 5.2, the maximum alert level (level 3, i.e. $\tau_c \geq 0.6$ s and $P_d \geq 0.2$ cm) corresponds to an earthquake with expected $M \geq 6$ and $I_{MM} \geq VII$. This means that the earthquake is likely to have a large size and to be located close to the recording site. A high level of damage is thus expected both nearby and far away from the recording station. On the contrary, in case of a recorded alert level equal to 0 (i.e., $\tau_c < 0.6$ s and $P_d < 0.2$ cm), the event is likely to be small and far away from the recording site. No damage is thus expected either close or far away from the station. Analogous considerations can be done for the alert levels 1 and 2. Due to the amplitude decay with distance, P_d is expected to decrease while moving far away from the source, while τ_c , which only depends on magnitude, is expected to remain approximatively stable. Therefore, only the 3-to-1 and the 2-to-0 transitions between alert levels are allowed².

²For example, if alert levels 3 (or 2) are observed in the source area, only alert levels 1 (or 0) are expected far away from it.

5.3 Potential Damage Zone Definition

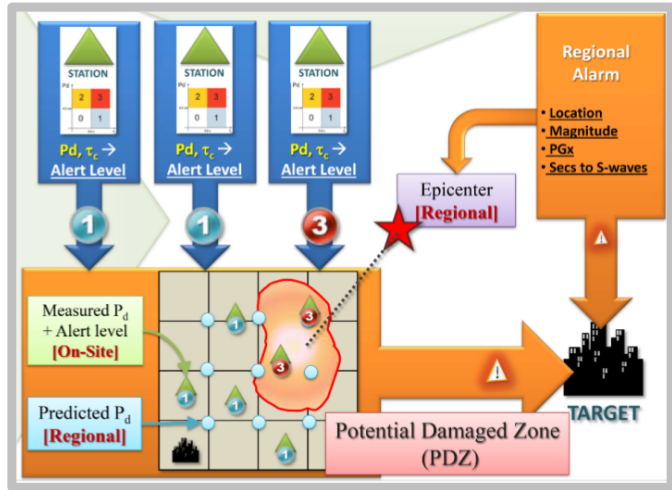
The idea of Zollo et al. 2010 was to define the PDZ as a circular area (including the highest observed alert levels) within which the strongest ground motion is expected to arrive. Fixing the parameter P_d at its threshold value, and using the progressively updated estimates of the period parameter, Equation 5.3 was used to determine the radius of the area within which the peak amplitude is expected to overcome the threshold value.

Here we improve this approach and propose a more refined methodology for the rapid mapping of the PDZ, based on the interpolation of predicted and observed P_d values within the considered area.

As soon as a station has been triggered by an earthquake, a preliminary location is obtained by using the real-time location technique of Satriano, Lomax, and Zollo (2008) (embedded in the *RTL*oc code). Then, when 3 seconds of P-wave signal are available at the recording station, P_d and τ_c are measured and a local alert level is assigned based on the decision scheme of figure 5.2a. The whole area of interest (i.e., the area covered by stations and the target area) is then divided into cells and the peak displacement values are predicted at each node of the grid, in order to fill the gaps where the P_d measurements are not yet available (through equation 5.3). Measured and predicted P_d values are then interpolated and the PDZ is delimited by the contour line corresponding to $P_d = 0.2$ cm (Figure 5.3).

This routine is repeated every second: as new observations of P_d and τ_c are available, other local alert levels are assigned at the triggered stations and updated estimates of the PDZ can be obtained from the interpolation of measured and predicted P_d values. Meanwhile, the event location and magnitude estimates are also refined as new phase picks and τ_c measurements are available. Figure 5.3 illustrates the conceptual scheme for the PDZ definition and computation.

Figure 5.3: PDZ definition. Conceptual scheme showing how measured and predicted P_d values are interpolated over the considered area. The PDZ is obtained by delimiting the region where $P_d \geq 0.2$ cm.



5.4 Application to strong Japanese events

The proposed methodology has been tested off-line using ten strong earthquakes ($M > 6$), recently occurred in Japan. For each of the analyzed earthquakes we compared the PDZ map with the I_{MM} and the Japanese Intensity (I_{JMA}) maps. Figure 5.4 shows examples of the map comparison for three representative events. The visual matching between the real-time PDZ and the postevent intensity maps suggests that the PDZ reproduces with a good approximation the area within which the highest intensity values are observed, both on the I_{JMA} and on the I_{MM} map. The $P_d = 0.2$ cm contour line approximately corresponds to a I_{JMA} around 5, which is indeed the minimum intensity necessary to issue a public warning.

A quantitative assessment of the performance can be obtained by evaluating the correspondence between the alert level issued at each station and the real macroseismic intensity experienced during the earthquake. To this end, we defined "successful", "missed" and "false" alarms, based on the criteria listed in Table 5.1, and we counted their total number.

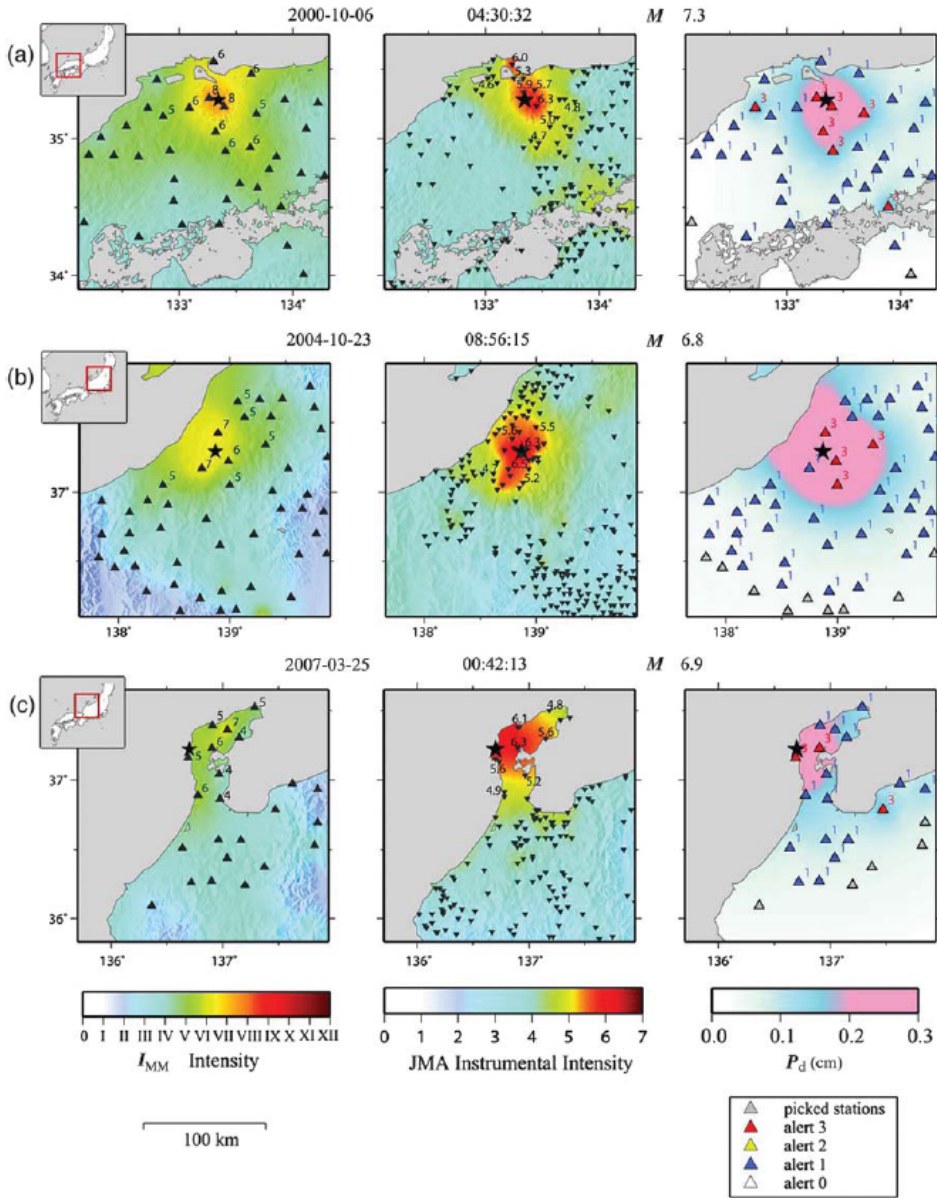


Figure 5.4: Examples of PDZ maps. The figure shows the results for the M 7.3, 2007, Western Tottori earthquake (a), the M 6.8, 2004, Chuetsu earthquake (b) and the M 6.9, 2007, Noto-Hanto earthquake (c). In each panel, the black star represents the epicenter and the triangles indicate the stations used for the analysis. Left panels: I_{MM} maps obtained from the observed PGV values. Center panel: I_{JMA} maps. Right panels: The PDZ maps resulting from the interpolation of measured and predicted P_d values, delimited by the color transition from light blue to red. Triggered stations are represented by grey triangles, while red and blue triangles show the alert level recorded at each station. [After Colombelli et al. 2012b.]

Alert Level	Successful Alarm	Missed Alarm	False Alarm
3	$I_{MM} \geq VII$	n.d.(*)	$I_{MM} < VII$
2	$I_{MM} \geq VII$	n.d.	$I_{MM} < VII$
1	$I_{MM} < VII$	$I_{MM} \geq VII$	n.d.
0	$I_{MM} < VII$	$I_{MM} \geq VII$	n.d.

Table 5.1: Definition of Successful, Missed and false Alarms, based on the recorded alert level. Each recorded alert level corresponds to a successful, missed or false alarm, based on the observed values of intensity. For example, a recorded alert level 3 corresponds to a successful alarm if the observed intensity (at that site) is $\geq VII$ and to a false alarm if the observed intensity is $< VII$. Similarly, the recorded alert level 1 corresponds to a successful alarm if the observed intensity is $< VII$ and to a missed alarms if the observed intensity is $\geq VII$. The alert levels 3 or 2 cannot be missed alarms, as well as 1 and 0 cannot be false alarms. (*), not defined. [After Colombelli et al. (2012b).]

The main results are shown in Figure 5.5: 87.4% of alert levels was correctly assigned, false alarms were 11.9% and missed alarms 0.7%. Despite the very high percentage of successful alarms, the percentage of false alarms turned out to be relatively high. In order to understand the relevance of this result we computed the difference between the predicted intensity ($I_{MM} = VII$) and the real observed intensity value. The variance distribution represented in left panel of Figure 5.5 shows that 36% of false alarms corresponds to an intensity value of VI ; 52% corresponds to intensity V , and 12% to intensity III . An intensity value of V , although it does not correspond to the maximum alert level (3), is synonymous with an earthquake that can be perceived by the population and may provoke some damage; keeping this in mind, the percentage of false alarms can be considered smaller. Thus, 52% of the false alarms were, in any case, not completely wrong.

5.5 Application to the Tohoku-Oki event

Using the same approach as described before, we estimated the P_d distribution for the whole territory of Japan during the 2011 Tohoku-

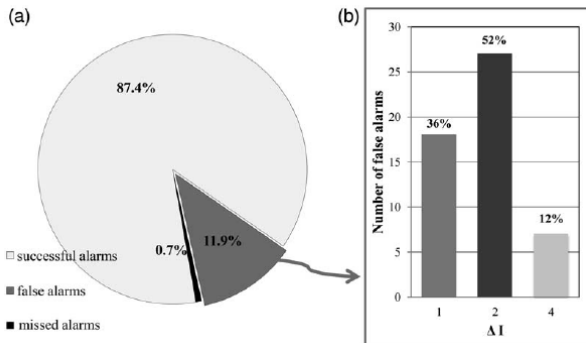


Figure 5.5: Cumulative statistics for the ten Japanese events. (a) The relative percentage of successful, false, and missed alarms. (b) In the histogram of false alarms, ΔI represents the difference between predicted ($I_{MM} = VII$) and observed intensity values. [After Colombelli et al. 2012b.]

Oki earthquake. For this event, in light of the results presented in Section 2.6, we used a progressively expanding PTW and simulated the real-data streaming across the network. We estimated the real-time predicted PDZ by interpolating the observed P_d values at close-in stations and the predicted P_d values at more distant sites. In Figure 5.6 we compare the I_{MM} distribution (a) with the predicted P_d distribution that would have been available 40 (b) and 60 s (c) after the origin time. The PDZ of Figure 5.6b is fairly consistent with the area where the highest intensity values are observed. The $P_d = 0.2$ cm contour line (represented by the color transition from light blue to red) approximately corresponds to the I_{MM} 6-to-7 transition. The first reliable mapping of the P_d distribution is available 40 s after origin time (panel b). However, the local alert levels at the coastal stations are available well before (two alert level 3 at the closest stations are available 25 s after the origin time) and this information can be used to issue a warning. A stable P_d distribution is finally available later in time, around 60 s after origin time (panel c). In the southern part of Japan (Tokyo region) the intensity values are not well reproduced, probably due to a significant contribution of the late peak arrivals radiated by the late activated asperities located southward the epicenter (i.e., the S3 source in Chapter 1), which mostly affected this area.

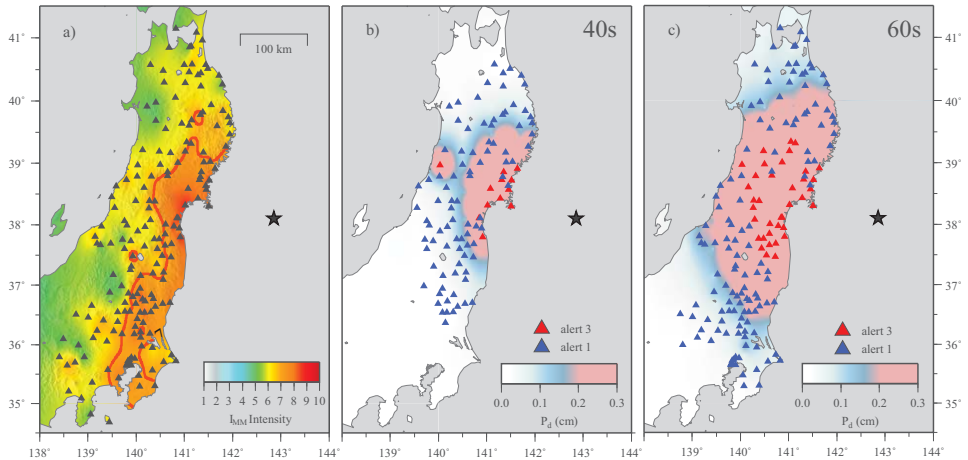


Figure 5.6: PDZ map for the Tohoku-Oki event. Comparison between (a) the I_{MM} map and the predicted P_d distribution that would have been available (b) 40 and (c) 60 s after the origin time. The distribution of P_d values is obtained after interpolating measured and predicted P_d values. In panel (a) the red contour line is the $I_{MM} = 7$ transition. In panels b and c, the color represents the local alert level that would have been assigned to each recording site. [After Colombelli et al. 2012a.]

5.6 Discussion

In the present chapter we have proposed a quantitative approach for a real-time mapping of the PDZ, based on the interpolation of measured and predicted values of initial peak ground displacement. The PDZ is available within a few seconds from the origin time. Then, with the passing of time, the shape and extension of the PDZ can be refined and local alert levels can be used to validate the alert issued by near-source stations. For all the analyzed events, the studied cases displayed a very good matching between the rapidly predicted PDZ, inferred from initial P-peak displacement amplitudes, and the instrumental intensity map, the latter being mapped after the event, using PGV and/or PGA , or from field macro-seismic surveys.

Compared to the pure on-site and regional EEWS this approach is

likely to provide more robust prediction of the area where the highest level of damage is expected to be observed. The proposed methodology for earthquake early warning is suitable to Japan or other high seismic risk countries, where a dense network of accelerometers is developed over the whole territory.

For the Tohoku-Oki earthquake, the availability of real-time measurements of P_d and τ_c at the closest stations allows for a rapid prediction of the expected ground motion at stations located far away from the source area and for a rapid estimation of the PDZ. This information would have been released approximately at the time of the S-wave arrival along the coast (about 40 s from the origin time). However, since the Tohoku-Oki earthquake epicenter was about 120 km offshore, it took more than a minute before the strongest shaking arrived in the same area (in Sendai area the maximum shaking arrived about 75 s after the origin time, see the timeline in Figure 6.4). The threshold-based approach would have not diminished the usefulness for early warning in that case.

APPLICATION OF REAL-TIME GPS TO EARTHQUAKE EARLY WARNING

6.1 Introduction of GPS data

The combined use of seismic and geodetic observations is now a common practice for finite-fault modelling and seismic source parametrization. With the advent of high-rate 1Hz GPS stations, the seismological community has recently begun looking at GPS data as a valid complement to the seismic-based methodologies for EEW.

For real-time seismic applications large dynamic range, accelerometric sensors are generally used. Accelerometer waveforms are integrated twice to obtain displacement time series; for near-field records this operation may lead to unstable results. Precise recovery of ground displacement requires indeed accurate baseline corrections and estimations of rotation and tilt motion (Kinoshita and Takagishi 2011). Furthermore, the application of the high-pass filter after the double integration operation, removes the artificial distortions but also reduces the low-frequency content of waveforms and possibly the static offset. Since GPS stations are able to register directly the ground displacement without any risk of saturating and any need of complicated corrections, geodetic displacement time series represent an important complementary contribution to the high-frequency information provided by seismic data.

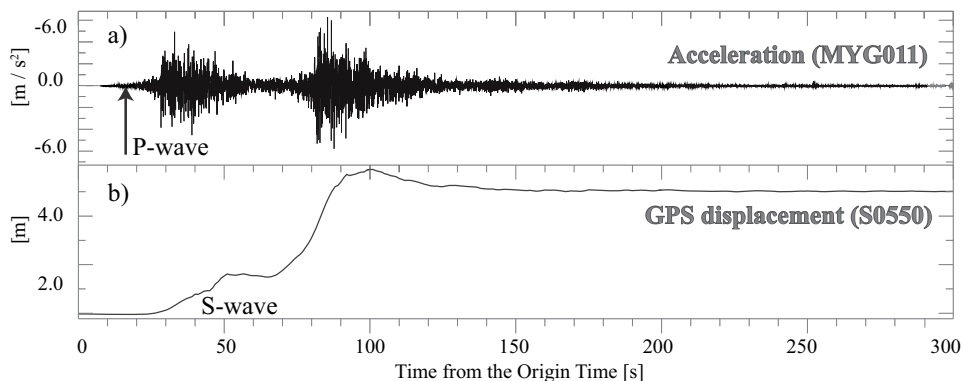


Figure 6.1: Comparison between GPS and seismic data. (a) acceleration waveform recorded during the 2011, Tohoku-Oki earthquake, at the closest seismic station (MYG011). (b) displacement waveform at the GPS station (S0550), co-located with MYG011 station. For both stations, the horizontal East-West component is shown. The accelerometer essentially recovers the dynamic component of ground motion, while the static deformation is dominant on GPS sensors.

GPS methods provide the evolutionary measurement of a ground motion quantity which is directly related to the earthquake magnitude. The permanent ground deformation, i.e., the resulting co-seismic displacement after the dynamic vibration has finished, is generally used to estimate the earthquake magnitude from GPS data and this is not affected by any saturation effect. Figure 6.1 shows a comparison between the GPS timeseries and the seismic displacement at two co-located stations.

The main limitation of GPS data is that the co-seismic ground displacement starts to be evident later than the P-wave arrival on the seismic records and approximately at the same time of the S-wave arrival (Allen and Ziv 2011). However, this does not prevent the use of close-in GPS stations for the issuance of a warning with the expected ground shaking at more distant sites and for the use of these data for tsunami early warning.

Many authors have recently started applying GPS data to EEW (Allen and Ziv 2011; Crowell, Bock, and Melgar 2012; Wright et al. 2012; Ohta

2012); they show that a rapid and remarkably robust magnitude estimate can be obtained, while the rupture process is underway. Here we investigate whether and how 1Hz GPS data can be used for both the rapid determination of the event size and for the real-time estimation of the rupture area, which would allow for a better prediction of the expected ground shaking at the target sites. For a practical implementation of EEWS, rapidity and reliability of the real-time estimations are fundamental features for the diffusion of a warning. We focus on the development of a rapid, stable, but approximate methodology and let more complex, post-event analysis achieve a complete and refined fault model characterization.

6.2 Real-time strategy

Following the approach proposed by Allen and Ziv (2011), we developed an efficient real-time static slip inversion scheme to provide a reliable magnitude estimate and a rapid estimation of the rupture area extent. We do not attempt to solve for detailed slip distributions but our focus here is to maximize the stability of the methodology when only limited information about the ongoing earthquake is available. The strategy we propose is simple and robust, and is expected to be suitable for any seismically active region. The main steps of the strategy are described below and in the flow-chart diagram of Figure 6.2. A detailed description for each step is given in Boxes 6.1 to 6.4.

The preliminary step for the inversion strategy is the real-time extraction of the static offset, which is done using a simple STA/LTA approach (Box 6.1). As soon as the static offset estimate is available at the first triggered GPS station, a preliminary estimate of the earthquake size can be obtained by approximating the source as a point source and assuming a short source-receiver distance. A point dislocation is obviously an unrealistic model for big earthquakes recorded at

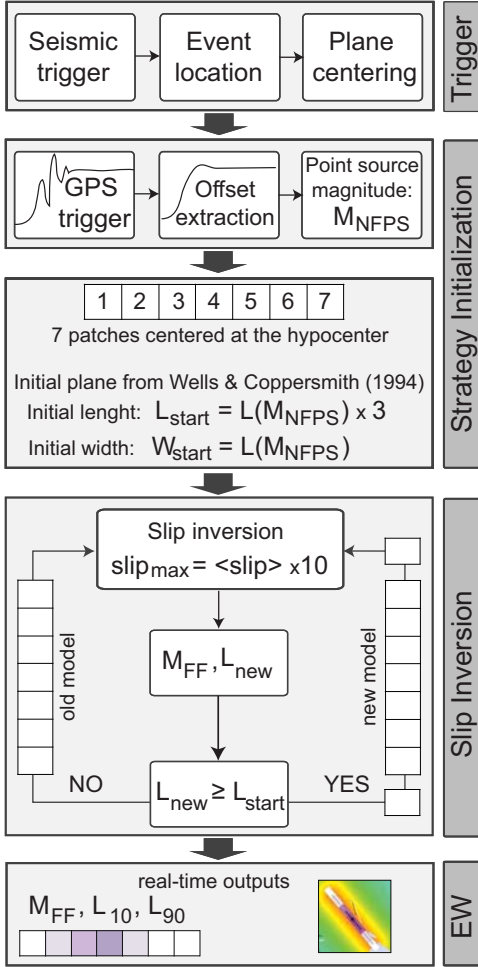


Figure 6.2: Flowchart of the inversion strategy. The algorithm looks for a trigger on the GPS displacement time series and starts the offset extraction. A rapid estimate of magnitude (M_{NFPS}) is obtained from the first available offset and is used to initialize the fault plane model (L_{start} and W_{start}). The slip inversion is then repeated every second. The new magnitude (M_{FF}) is used to estimate an expected fault length (L_{new}). L_{new} is then compared to L_{start} . If L_{new} is smaller than L_{start} , the same model is adopted, and a new inversion is run. If L_{new} is greater than L_{start} , the fault plane length is increased, and two patches are added at each end of the fault. Three real-time outputs are provided by the inversion strategy at each time: the current magnitude estimate resulting from the slip inversion (M_{FF}), and the real-time estimations of L_{10} and L_{90} . M_{FF} and L_{10} are finally used to predict the ground shaking in the region. [After Colombelli, Allen, and Zollo 2013.]

near source distances, but this assumption may provide a useful and rapid initial magnitude estimate from the early recorded signals (Box 6.2). Then, the slip inversion on a given fault plane starts. The offset estimates are updated every second (the data is 1 sample per second), and the slip distribution is therefore recalculated every second as new data becomes available (Box 6.3). The evolutionary magnitude estimate resulting from the slip inversion is finally used to predict the intensity distribution in the proximity of and far away from the source (Box 6.4).

Box 6.1: Permanent displacement extraction

The permanent deformation is mathematically described by the near-field term in the Green's function. Due to its rapid decay with distance (as $1/R^2$) (Aki and Richard 2002; Kanamori and Brodsky 2004) the static deformation can be dominant in the proximity of the source but is generally obscured by the dynamic component at greater distances. Although accurate estimates of the permanent displacement can be easily obtained in the post-event phase, following dynamic motion, the static deformation is expected to arrive shortly after the arrival of the first dynamic component. As long as we are able to distinguish the static component from the dynamic oscillation, real-time estimates of the permanent ground deformation can be achieved before the dynamic component has subsided.

In order to extract the static component we used the algorithm developed by Allen and Ziv (2011). The algorithm looks for a trigger along the record using a pre-determined condition on the short-term (STA) vs. long-term signal average (LTA) (Allen 1978). For all the analyzed earthquakes the short term and the long term time windows have been set to 2 and 100s, respectively and the STA/LTA threshold ratio for the triggering declaration has been set to 10. These values have been found by trial and error to provide correct trigger attributions at close-in stations and to avoid false triggers at distant sites.

Starting from the trigger time, a cumulative running average of the observed displacement is computed along the waveforms and is delivered as a real-time estimate of the static offset. To prevent the inappropriate use of a dynamic oscillation amplitude as the permanent offset, the algorithm starts to deliver the running average after a) two zero crossings, b) two trigger-amplitude crossings or c) 10s after the trigger time, whichever comes first. These three conditions have been purposely designed to account either for cases where the dynamic oscillation is dominant (and the signal is a sinusoidal-type oscillation) and for cases where the static component is dominant (and the waveform is a ramp-type signal).

Use of the running average as an estimate of the static offset is expected to remove, or reduce, the contribution of the dynamic component of the signal, which would affect the estimation of the static offset. The use of longer time windows for averaging would stabilize the static offset estimation, but they would also delay the final solution. Various approaches for the real-time offset extraction have been proposed based on moving average windows with different length. After looking at their performance in terms of delivery time and stability of the static offset for all stations for these three earthquakes, we find the algorithm proposed by Allen and Ziv (2011) to be the most general and efficient approach. Because of the logarithmic scaling between the permanent deformation and magnitude (through the seismic moment), once the dynamic component has been carefully removed, further small variations in the static offset due to noise or spurious signal contaminations do not have a significant effect on the magnitude estimate.

Box 6.2: Point source magnitude

At short distances from the source, the primary component of the static displacement, u , can be written as (Aki and Richard 2002; Kanamori and Brodsky 2004):

$$u = \frac{1}{4\pi\mu R^2} \cdot M_0 \quad (6.1)$$

where μ is the rigidity modulus of the medium, R the hypocentral distance and M_0 the seismic moment. The application of this formula requires the earthquake hypocenter to be known. Although reliable trigger techniques for GPS data have been proposed (e.g., Ohta 2012), real-time algorithms for earthquake detection on seismic records are more accurate and long proven, and are able to provide reliable estimates of the earthquake location within few seconds from the first P-wave detection (Satriano, Lomax, and Zollo 2008). While accurate locations are not required for this preliminary magnitude estimation, the contribution of seismic EEW methodologies is obviously essential for this stage of our GPS-based strategy. The preliminary near-field, point source magnitude (M_{NFPS}) is useful in its own right and provides a better estimate of magnitude than seismic-based EEW methodologies alone (see later examples). In addition, the M_{NFPS} estimate, and the seismic-based hypocenter location are then used to initialize the inversion scheme, i.e., to determine the initial fault plane to be used for the first real-time static slip inversion, according to the procedure discussed in Section 6.3.

6.3 Early Warning outputs

We start the inversion strategy using the initial fault model dimensions as estimated based on Wells and Coppersmith (1994) relationships; we divide the entire fault plane into 7 rectangular patches. Given that the initial size of the model fault plane is determined based on the first magnitude estimate using the Near-Field Point Source approximation (hereafter M_{NFPS}), it is important to allow the fault plane to increase in size. We use a "self-adapting" strategy in which the fault plane can increase in size based on the evolutionary magnitude estimate (Figure 6.2).

At each inversion, the current magnitude value is used to compute the corresponding length (the expected length from Wells and Coppersmith 1994). As soon as the new estimated length exceeds the

initial value, the model is upgraded. This is done by resizing the entire fault plane (in both length and width) and adding two additional fault patches, one at each end of the plane. Adding two extra patches when the plane needs to be expanded maintains consistency with the previous model in terms of slip distribution and ensures an approximately constant spatial slip resolution over time. For the two new extreme patches we assume the same initial slip range as for the inner adjacent patch.

Two main pieces of information are released in real-time as output from the inversion algorithm: the magnitude resulting from the slip inversion (Finite Fault magnitude, hereafter M_{FF}) and the rupture area extent. We characterize the rupture extent in terms of rupture length along strike and centroid location. We determine where along the fault the slip amplitude drops to 90% and 10% of the maximum value using a piecewise linear fit to the slip values of each patch. We refer to these lengths as L_{90} and L_{10} , respectively.

The real-time measures of magnitude and rupture area length are finally used to produce the expected ground shaking distribution due to the extended finite source. At each 1-second iteration we use the current magnitude value and the L_{10} estimate as a measure of the fault plane length. The fault plane width is fixed at the same value as used for the slip inversion and for the shaking prediction the plane is centered on the middle point of L_{10} . The expected intensity distribution is thus computed based on distance from the finite fault.

Box 6.3: Static-slip inversion

The slip inversion step starts with the construction of the initial fault plane geometry; two pieces of information are required. The first is the position (geographical coordinates) and the orientation (strike, dip, rake) of the fault plane. Various catalogues of active faults around the world have been compiled and provide position, geometry and orientation. This is true for the plate boundary faults, including the major subduction zones that are part of this study, and also for regional faults in California and Mexico. In our approach we make the assumption that the orientation of the fault plane is that of the nearest known fault plane, as taken from the appropriate regional fault catalogue. We then locate the fault plane, with an orientation based on the nearest known fault, such that it intersects the hypocenter for the event underway. The second necessary piece of information is a rough estimation of the fault plane extent along the strike and the dip directions. An approximate but reasonable fault plane model is fundamental both to avoid initial over/under estimations, which may bias the following solutions, and to ensure minimal computation times and maximal resolution of the slip distribution. The near-field, point source magnitude is a reasonable starting value to set up the size of the initial fault plane model.

The size of the fault plane model is determined using the empirical scaling relationships from Wells and Coppersmith (1994) relating the earthquake magnitude to the surface rupture length and the down-dip rupture length (table 2A, Wells and Coppersmith 1994). We use the appropriate scaling relationship for each specific tectonic environment (i.e., for normal, reverse or strike-slip ruptures). Furthermore, to account for bilateral ruptures, and to accommodate the uncertainties in the scaling relationships and the real-time magnitude estimates, our parametrized model has a fault length three times the length provided by the scaling relation along strike.

For simplicity and to minimize the computational time, we initially discretize the fault plane into 7 rectangular, equally sized rupture segments all of which extend the full down-dip width of the fault. Our target is an approximate estimation of the along-strike extension of the rupture (i.e., the length of a line source). This model set-up allows the lateral extent of the slip to vary, and therefore to be determined, in both directions from the hypocenter, neglecting the down-dip variations of slip distribution. We found that 7 is a reasonable number of patches as it allows for a sufficient slip variability along the strike of a $M > 6$ earthquake fault in just one or both rupture directions, while also keeping the model parameters to a minimum. Having a fixed number of patches clearly affects the spatial resolution of the slip model and does not allow capture of slip heterogeneity smaller than the size of the patches themselves. Again, for the aim of our methodology, a rather accurate reconstruction of the slip model is not required. *(continued)*

Box 6.3: Static-slip inversion (continued)

We model the static offset (both horizontal and vertical) using the rectangular dislocations along our defined fault plane embedded in a homogeneous half-space. The entire fault plane is discretized into independent subfaults and the slip on each patch is assumed to be constant (Okada 1985).

The general problem of inversion for slip is non-linear since surface displacements are non-linear functions of the fault geometry through the analytic expression of the Green's Functions derived by Okada 1985. However, when fault geometry and orientation are fixed, the inverse problem becomes linear and can be written as:

$$\mathbf{G}\mathbf{m} = \mathbf{d}$$

where \mathbf{G} is the matrix of Green's functions relating the model parameter \mathbf{m} (slip on each patch) to the observed permanent ground displacement \mathbf{d} .

We solved for the slip on each patch by minimizing the square misfit between observed and predicted displacements (L2 norm). To regularize the inversion the slip is constrained to a single direction. For subduction zones only solutions with normal dip-slip are permitted and in translational tectonic environments only lateral strike-slip is allowed. To avoid rough slip distributions, we applied a median filter to smooth the solution and impose the slip to taper to zero at the edge of the fault.

We solve the inverse problem through a genetic algorithm (Holland 1975, 1992) implemented in a MATLAB code (Shirzaei and Walter 2009). The platform chosen is not the most appropriate for real-time operations but the optimization of the algorithm would require a complete rewriting of the code. For the first inversion, we explore any possible slip value in a range which is determined from M_{NFPS} . Given the fault plane area and the initial seismic moment, we compute the corresponding average slip value and set an initial exploration range around this value. For the specific case of our algorithm, the initial exploration range was set from 0 to 10 times the average slip value. After the first inversion, to stabilize and speed up the estimation of the slip distribution, we constrain the genetic algorithm to look for the optimal solution in a range that is determined based on the results of the previous inversion. At each inversion run following the first one, the slip on each patch is allowed to vary in a narrow range around the value of the previous inversion (0 to 3 times the maximum slip). This range has been found by trial and error to guarantee the stability of the solution at each time, without restricting the exploration range excessively.

Given the slip distribution, the corresponding seismic moment is computed by multiplying the integral of the slip over the fault area by the shear modulus (here assumed to be 33 GPa). The moment magnitude is finally obtained through the moment-magnitude relationship of Hanks and Kanamori (1979).

Box 6.4: Ground shaking prediction

The *PGA* and *PGV* values are first predicted using a standard ground motion prediction equations relating magnitude, distance and the ground motion quantities. The instrumental intensity is then obtained from *PGA* and *PGV* using an empirical conversion relationship. We assumed a rock-soil type and did not consider any amplification/attenuation effect due to local site conditions.

For El Mayor-Cucapah earthquake, we used the approach of ShakeMap (USGS). We compute the expected *PGA* and *PGV* using the ground motion estimation equation of Boore, Joyner, and Fumal (1997), which has the form:

$$\ln Y = b_1 + b_2(M - 6) + b_3(M - 6)^2 + b_5 \ln \sqrt{r_{jb}^2 + h^2} + b_v \ln(v_s/v_a) \quad (6.2)$$

where M is the magnitude, v_s is the average shear wave velocity (upper 30m), r_{jb} is the Joyner-Boore distance (distance from the surface projection of the fault plane - Joyner and Boore 1981) and $b_1, b_2, b_3, b_5, b_v, v_a, h$ are parameters derived from the regression. For the b_1 coefficient we assumed the strike-slip source type. *PGA* and *PGV* are then converted into a Modified Mercalli Intensity (*MMI*) scale, using the empirical relationship of Worden et al. (2012):

$$\begin{aligned} MMI &= c_1 + c_2 \log(Y) && \text{for } \log(Y) \leq t_1 \\ MMI &= c_3 + c_4 \log(Y) && \text{for } \log(Y) > t_1 \end{aligned}$$

where Y is the ground motion quantity (*PGA* or *PGV*) and c_1, c_2, c_3, c_4, t_1 are coefficients derived from the regression.

For the Japanese earthquakes we followed the approach of JMA to compute the expected seismic JMA intensity (I_{JMA}) at each site. We first compute the expected *PGV* distribution using the attenuation relationship of Si and Midorikawa (1999), which is written as:

$$\log A = aM + hD + d + e - \log(R + c) - kR \quad (6.3)$$

where A is the ground motion parameter (*PGA* or *PGV*), M is the magnitude, D is the source depth, R is the distance from the fault plane and a, c, d, e, h and k are coefficients resulting from the regression analysis. *PGV* is then converted into a seismic intensity value using the relationship of Midorikawa, Fujimoto, and Muramatsu (1999):

$$I_{JMA} = p + q \log(A) \quad 4 \geq I_{JMA} \leq 7$$

where A is the ground motion quantity (*PGV*) and p and q are parameters derived from the regression.

6.4 Application and results

The proposed methodology has been applied to 3 earthquakes: the M_w 9.0 2011 Tohoku-Oki earthquake, the M_w 8.3 2003 Tokachi-Oki earthquake and the M_w 7.2 2010 El Mayor-Cucapah earthquake. The 1Hz GPS time series have been post-processed using the method of instantaneous positioning described in Bock, Melgar, and Crowell (2011) with refined orbit and clock corrections.

6.4.1 The Mw 9.0 2011 Tohoku-Oki earthquake

We analyzed the co-seismic ground deformations collected by 847 3-component recording stations of the Japanese GPS Earth Observation Network (GEONET) (Sagiya 2004), in a distance range between 120 and 600 km from the hypocenter. We use a subduction interface with strike and dip of 195° and 15° respectively based on the USGS NEIC catalog of subduction zone plate boundaries. We position the fault plane to intersect the earthquake hypocenter, and we assume a pure reverse fault mechanism.

The GPS-trigger algorithm declares the first arrival at the closest station (station 0550, along the Sendai coast) 29 s after the earthquake origin time and starts to deliver the running estimate of the static displacement 10 s later. At the same time, the magnitude estimation with the near-field and point source approximation gives $M_{NFPS} = 8.22$. With this magnitude, we build our starting model with 7 rectangular patches of 90x50 km each (for total dimension along strike of 630 km, i.e., three times the expected length) and proceed with the slip inversion step. For this earthquake the estimated length does not exceed the length of starting model; the increase in size of the fault plane is thus never triggered. Figure 6.3 summarizes the results of our strategy for three different times [39 s(a), 100 s(b) and 200 s(c)].

The real-time magnitude estimation (Figure 6.4a) is extremely robust

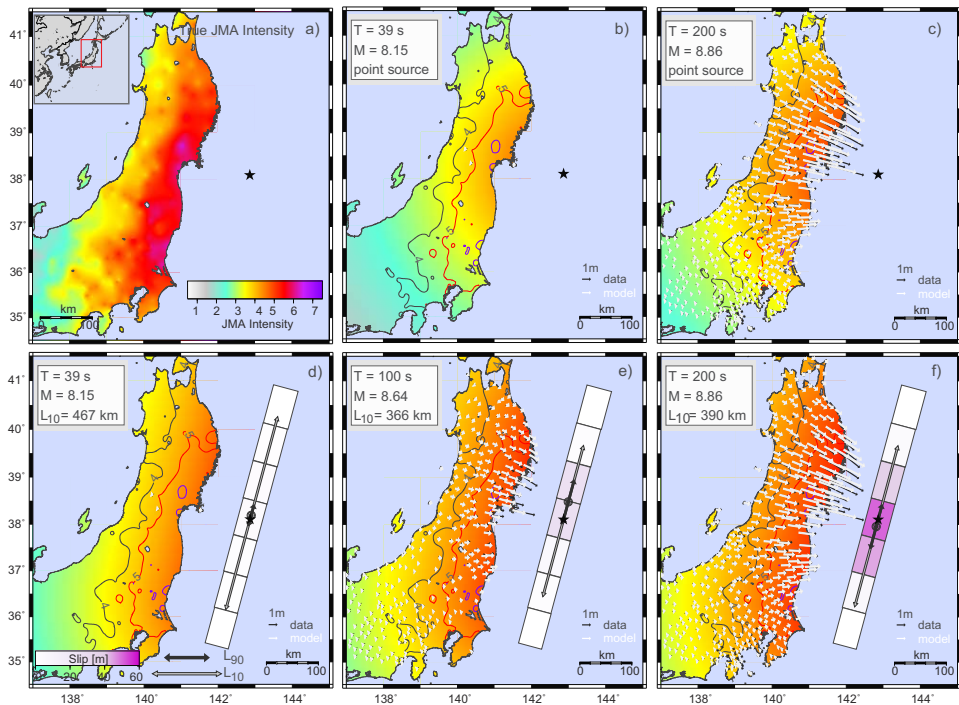
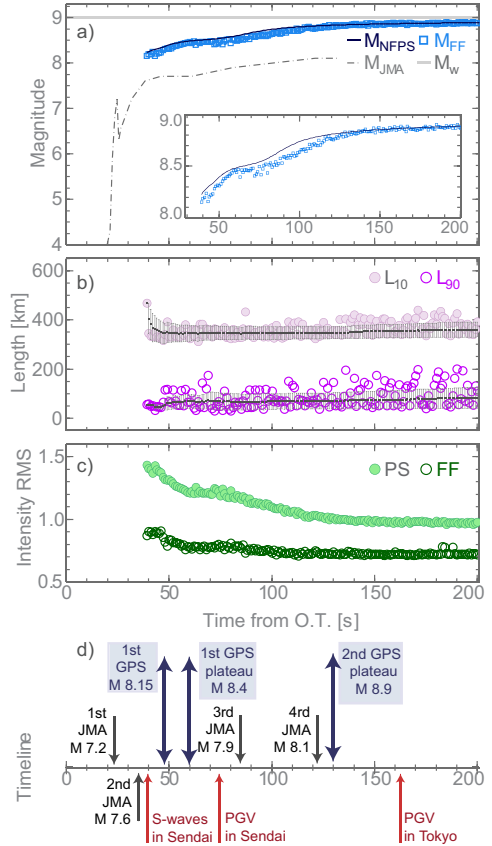


Figure 6.3: Snapshots of the GPS-based strategy for the M_w 9.0, 2011 Tohoku-Oki earthquake. The snapshots show the comparison between the intensity prediction using the point source and the finite fault at three different times. (a) The true JMA intensity (I_{JMA}) distribution. (b and c) The ground shaking predictions assuming a point source (at the hypocenter) at 39 and at 200 s, respectively. (d, e, and f) The results of the finite source strategy obtained at 39, 100 and 200 s, respectively. The background color is the predicted intensity distribution using the current magnitude value and the distance from the finite fault (L_{10}). The length estimates L_{10} and L_{90} are also plotted as vectors on the fault plane with a narrow gray vector, and a thick, shortest black vector, respectively. The small circles at the center of the L_{90} segment correspond to the midpoint that we use as the centroid of the maximum slip area. The gray and red foreground lines represent the $I_{JMA} = 4$ and the $I_{JMA} = 5$ contour lines, respectively. In all panels, black vectors represent the observed horizontal offset while white vectors show the static displacement resulting from the inversion algorithm. [After Colombelli, Allen, and Zollo 2013.]

and consistent with that of other simulated real-time analysis (Ohta 2012; Wright et al. 2012). Both magnitude estimates (M_{NFPS} and M_{FF}) show a similar behaviour. The first result is available at 39

Figure 6.4: Real-time output for the M_w 9.0, 2011 Tohoku-Oki earthquake. Results of the inversion strategy as a function of time from the origin time.

(a) Magnitude with the near-field, point source approximation (M_{NFPS} - dark blue solid line) and magnitude resulting from the slip inversion (M_{FF} - small blue squares). For comparison, the evolution of magnitude estimate provided by the JMA early warning system is also shown as a dotted gray line, and the continuous gray line represents the real moment magnitude value. (b) Real-time estimates of L_{10} (lilac filled circles) and L_{90} (purple empty circles) as provided by the slip inversion. (c) RMS error on intensity prediction, assuming a point source (labeled as PS in the plot, light green filled circles) and the finite fault (FF in the plot, dark green empty circles). (d) Warning timeline for the Tohoku-Oki earthquake showing when the GPS information is available with respect to the time at which the strongest shaking occurs in the Sendai and Tokyo regions and with respect to the JMA warnings. [After Colombelli, Allen, and Zollo 2013.]



s after the origin time, when M_{NFPS} is 8.23 and M_{FF} is 8.15. The two magnitudes rapidly increase reaching a first plateau level around 60 s, when M_{NFPS} gives 8.5 and M_{FF} gives 8.4. A new increase begins around 80-90s and both magnitudes reach their near-final values ($M_{NFPS} = M_{FF} = 8.9$) around 120 s.

Stable estimates of both L_{10} and L_{90} result from the slip inversion as well. L_{10} (intended to represent the total length of the rupture) ranges from 298 km and 476 km, with a mean value of 360 ± 30 km over the entire time period. L_{90} (length of peak rupture) varies between 30 km and 199 km, with a mean value of 83 ± 42 km (Figure 6.4b).

Several authors have derived co-seismic slip distributions and finite fault models for the M_w 9.0, 2011 Tohoku-Oki earthquake using a variety of dataset (Inuma 2011; Lee et al. 2011; Romano et al. 2012; Suzuki, Aoi, and Sekiguchi 2011, among many others). The fault plane is usually modeled as a rectangular area of approximately 400x200 km. A common result between all these models is the presence of extremely large slip asperity (with slip greater than 50 m) concentrated around the hypocenter in a relatively small area (about 100x40 km). A qualitative, visual comparison of our real-time results with post-event analysis shows that L_{10} provides a good estimation of the total ruptured area and L_{90} is consistent in both position and extension with the largest observed asperity.

The RMS plot of Figure 6.4c shows the difference between observed and predicted intensity at each time. We found a systematic, significant improvement in the ground shaking prediction when the finite fault is used (labelled as FF in the plot), with respect to the case of the point source (PS in the plot). Starting from the very beginning our shaking prediction clearly indicates that high intensity values are expected along the entire coast, from the closest Sendai area to the faraway Tokyo region. At the same time, when the point source is used, the intensity is instead largely underestimated especially far away from the epicenter region. We found, however, that the highest intensity values (> 5.5 -6) along the coast are not well reproduced. This may probably due to the fact that we did not consider any local/site effect which may strongly affect the ground shaking.

6.4.2 The 2003 M_w 8.3 Tokachi-Oki earthquake

The 2003 M_w 8.3 Tokachi-Oki earthquake occurred on 25 September at 19:50:07 UTC along the Japan Kuril trench off the Tokachi district of Hokkaido, northern Japan, where the Pacific Plate is subducting beneath the Hokkaido peninsula. Finite fault models indicate a

thrust-fault mechanism (strike 234° , dip 7° , rake 103°) rupturing an area of approximately 140×160 km with an estimated seismic moment of 2.9×10^{21} Nm (Honda et al. 2004). High co-seismic displacements (up to 1 m) were recorded at the coastal stations of GEONET nearest the epicenter (Honda et al. 2004; Miura et al. 2004) where a permanent displacement of about 0.5 m has been observed (Crowell, Bock, and Squibb 2009). Ground deformations were observed up to 200 km away from the source where the displacement amplitude exceeded 2 cm (Irwani et al. 2004). The analyzed data set consists of 169 3-component recording stations in a distance range between 80 and 600 km from the hypocenter.

We use a subduction interface with strike and dip of 211° and 11° respectively, based on the USGS slab model for the subduction zone catalog of the Hokkaido, Japan region. Again the fault is positioned to intersect the earthquake hypocenter and we assume a pure dip-slip reverse fault mechanism. The GPS strategy starts with the first trigger declaration 24 s after the origin time at the closest station (station 0134); the static offset extraction begins 10s later and the initial M_{NFPS} is 8.17. The starting fault plane is made with 7 rectangular patches of 83×55 km each. Since the magnitude does not change significantly, the fault model size is not updated. The results are summarized in Figure 6.5 for three different times [24 s(a), 100 s(b) and 160 s(c)]. For this M_w 8.3 earthquake the initial M_{NFPS} and M_{FF} estimates are somewhat different being M_{NFPS} 8.17 and M_{FF} 8.45. The M_{NFPS} remains approximately constant to its initial value over the entire time range. The M_{FF} estimates vary between 8.15 and 8.45, starting high, and reaching a stable value ($M_{FF} = 8.2$) around 40 s from the origin time (a). The estimated total length (L_{10}) has a stable mean value of 294 ± 26 km (varying between 228 and 355 km) (b). The maximum slip area (L_{90}) ranges between 25 and 180 km, with a mean value of 74 ± 28 km (Figure 6.6).

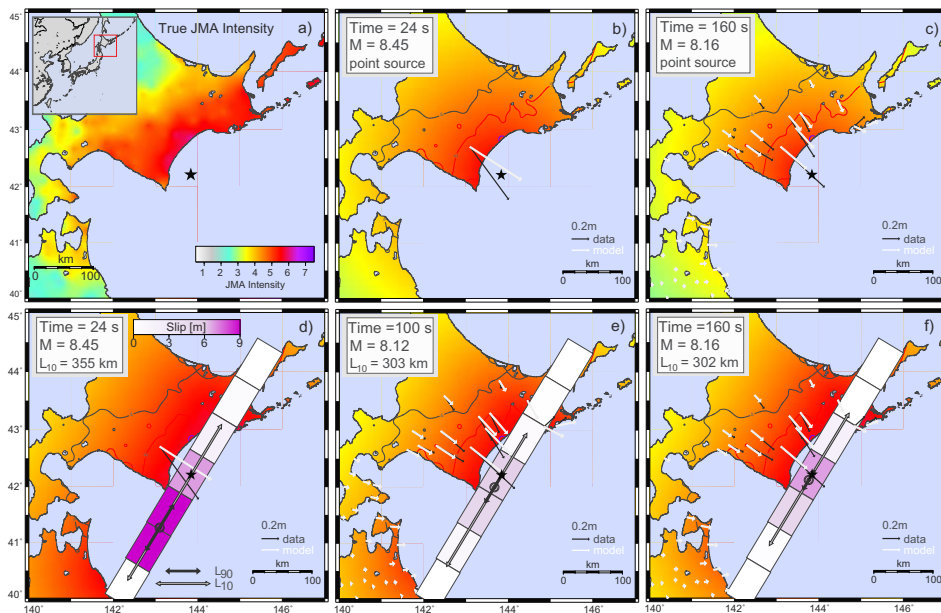
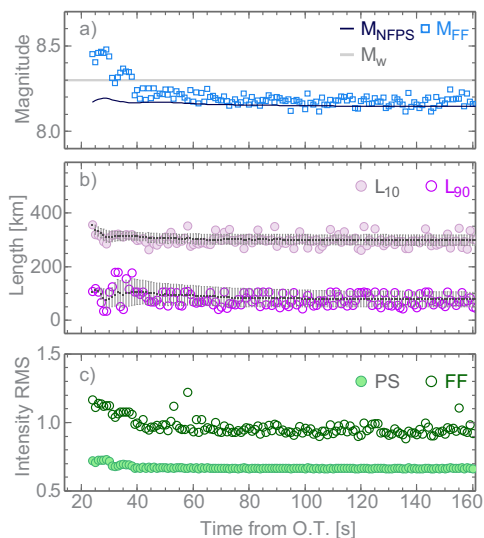


Figure 6.5: Snapshots of the GPS-based strategy inversion for the M_w 8.3, 2003 Tokachi-Oki earthquake. Comparison between the (a) observed intensity with the predicted intensity using (b, c) the point source and (d, e, and f) the finite fault for three different times. The first result from the slip inversion is available 24 s (b, d) after the origin time, followed by the estimates after 100 s (e) and 160 s (c, f). For details, refer to the caption of Figure 6.3. [After Colombelli, Allen, and Zollo 2013.]

Different finite fault models have been proposed for the 2003, Tokachi-Oki earthquake (Honda et al. 2004; Koketsu et al. 2004; Romano et al. 2010). The fault plane is generally modelled with an aspect ratio close to one (140x160 km, 120x100 km, 210x150 km are examples of the adopted dimensions). A general feature resulting from the slip inversions is that the main asperity (with a peak slip of about 6 m) is concentrated in the northwest part of the fault plane and another ruptures area extends down-dip from the hypocenter. While our real-time estimate of the total rupture length (L_{10}) is overestimated when compared to these post-event models, the area where most of the slip occurred is rather well approximated, in both extension (L_{90}) and po-

Figure 6.6: Real-time output for the M_w 8.3, 2003 Tokachi-Oki earthquake. For details, refer to the caption of Figure 6.4. [After Colombelli, Allen, and Zollo 2013.]



sition (centroid) on the plane.

Due to the overestimation of the total rupture length, the ground shaking prediction for this earthquake is less accurate when the finite fault is considered compared to the use of a point source. This is especially true at the initial seconds when the magnitude value is also overestimated. As the magnitude estimation decreases, the RMS gradually reaches an approximately stable value (~ 0.9) which is, however, still larger than the RMS obtained with the point source (~ 0.7). We return to this overestimation in the discussion section.

6.4.3 The M_w 7.2 El Mayor-Cucapah earthquake

The M_w 7.2, 2010 El Mayor-Cucapah earthquake occurred on 4 April, 2010 at 22:40:42 UTC approximately 50 km south of the Mexico-USA border along the boundary between the Pacific Plate and the North America Plate, in northern Baja California. The main shock ruptured a series of fault segments with NW-SE alignment with a total extent of approximately 120x20 km and with an estimated seismic moment of about 3×10^{19} Nm (Hauksson et al. 2010). Moment tensor solutions

and post-earthquake imaging of the rupture process show evidence for a complex rupture history, with a dominant right-lateral strike-slip component (strike 234° , dip 7° , rake 103°) combined with a significant non-double-couple component (Hauksson et al. 2010; Wei 2011). We analyzed the co-seismic displacement registered at 1 Hz GPS stations of the California Real-time Network (CRTN). We model the fault plane with a pure vertical right-lateral strike-slip fault, striking at 320° and intersecting the earthquake hypocenter.

We are able to detect the first trigger 34 s after the earthquake origin time at the station P494, where, 10 s later, the first estimation of static offset becomes available. Based on the first M_{NFPS} value ($M_{NFPS} = 7.25$), we model the initial fault plane with 7 rectangular patches of 28×16 km. Figure 6.7 shows the slip distribution obtained after 34 s (a), 100 s (b) and 160 s (c).

For this earthquake we found very robust magnitude estimations both from M_{NFPS} and from M_{FF} . The two magnitudes are consistent with the M_w value for this event ($M_w 7.2$) although the magnitude resulting from the inversion shows a systematic small underestimation (about 0.2 magnitude units) with respect to M_{NFPS} . Specifically, M_{NFPS} ranges between 7.16 and 7.27, with a mean value of 7.2 while M_{FF} varies between 6.9 and 7.1, with a mean value around 7.0 (Figure 6.8a). L_{10} and L_{90} are also quite stable: L_{10} varies between 107 and 160 km, with a mean value over the entire time period of 143 ± 11 km while L_{90} ranges between 10 and 62 km, with a mean value of 38 ± 14 km (Figure 6.8b).

From the joint analysis of geodetic, remote-sensing and seismological data, Wei (2011) reconstructed the fault geometry and the history of slip during the 2010 El Mayor-Cucapah earthquake. Their fault plane extended about 120 km along strike and about 20 km in the down-dip direction. A similar result has been found by Rodriguez-Perez and Castro (2012) that, based on the distribution of aftershocks, modelled

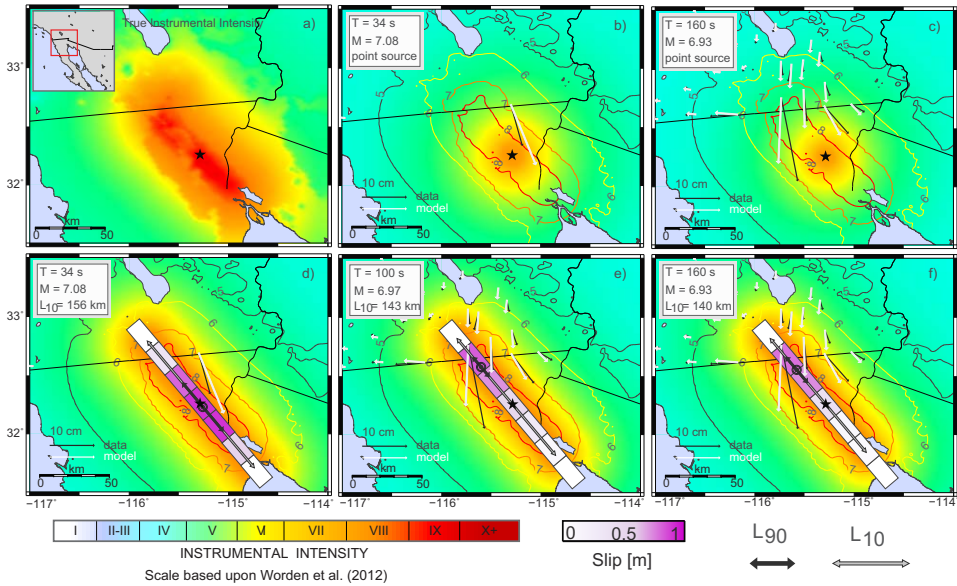


Figure 6.7: Snapshots of the GPS-based strategy inversion for the M_w 7.2, 2010 El Mayor-Cucapah earthquake. Comparison between the (a) observed intensity with the predicted intensity using (b, c) the point source and (d, e, and f) the finite fault for three different times. The first result from the slip inversion is available 34 s (b, d) after the origin time followed by the estimates after 100 s (e) and 160 s (c, f). The gray, yellow, orange, and red foreground lines represent the $MMI = 5, 6, 7,$ and 8 contour lines, respectively. For details, refer to the caption of Figure 6.3. [After Colombelli, Allen, and Zollo 2013.]

the fault plane as a rectangular area of 140×30 km. Most of the slip occurred in an area of approximately 40×10 km, concentrated in the north-western part of the fault plane where the rupture, after nucleating from the hypocenter, propagated and broke the largest asperity. (Fig. 3 from Wei (2011); Fig. 4 from Rodriguez-Perez and Castro (2012)). Our real-time estimates of L_{10} and L_{90} show an excellent agreement with both the total length of the rupture area and the extension of the main asperity, respectively. The position of our real-time slip centroid also reproduces the observed north-west oriented slip distribution.

In terms of ground shaking prediction the El Mayor-Cucapah earth-

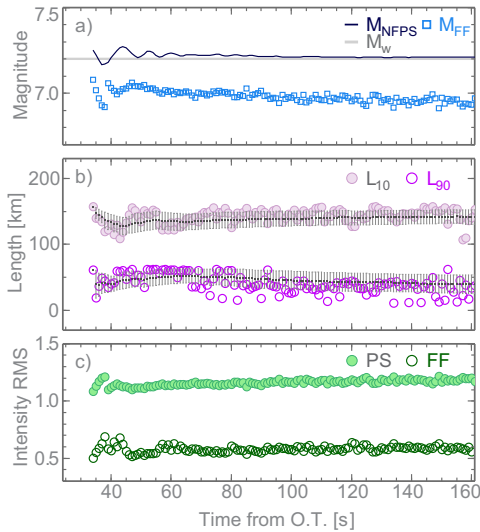


Figure 6.8: Real-time output for the M_w 7.2, 2010 El Mayor-Cucapah earthquake. For details, refer to the caption of Figure 6.4. [After Colombelli, Allen, and Zollo 2013.]

quake is the clearest evidence of how the prediction improves when the extended fault is considered. A visual comparison between the maps of Figure 6.7 shows that when the point source is used, the resulting intensity is biased, especially along the strike direction. When the extended fault plane is used, instead, a more realistic and accurate prediction of the intensity distribution is obtained. The RMS error on intensity (Figure 6.8c) is significantly reduced from a value of ~ 1.1 (with the point source) to ~ 0.6 when the finite fault is considered and remains approximately stable for the entire duration of the event.

6.5 Discussion

The proposed methodology provides reasonable magnitude estimates for the three analyzed cases. This result is even more relevant for the 2011 Tohoku-Oki event, for which the GPS-based estimates are significantly higher than the real-time seismic-based estimates. The first magnitude estimate ($M_{FF} = 8.15$) can be determined 39 s after the origin time. At the same time, the seismic-based magnitude was ~ 7.7 2.4. As discussed in Section 5.6, the strong-motion arrived along

the Sendai coast about one minute after the earthquake occurrence and it took nearly two minutes for the strongest shaking to hit residential areas in the Tokyo region. The GPS-based magnitude estimate could have been used for the prompt activation of emergency actions in the faraway Tokyo region as well as along the closest Sendai coast.

In addition to the magnitude estimate, the proposed methodology provides a real-time estimate of the rupture area extent, based on the slip distribution on the fault plane. Comparison of our inversion results with other post-earthquake studies shows that L_{10} and L_{90} are approximate, but useful estimates of the total rupture length and of the region where most of the slip is occurring, respectively. The fault length estimates (L_{10} and L_{90}) are also very stable in time. This information should be integrated in a real-time EEWS to improve the ground shaking prediction by using the distance to the finite fault rather than distance from the hypocenter when estimating shaking intensity.

For the 2011, Tohoku-Oki and the 2010, El Mayor-Cucapah earthquakes we found a clear improvement in the intensity prediction when the real-time GPS magnitude estimates and the finite fault are considered. The intensity prediction is not as good in the case of the 2003, Tokachi-Oki earthquake. For this event, however, the fault plane has been modelled by others with an aspect ratio close to one and a significant slip contribution comes from the deeper part of the plane. The down-dip length of the fault planes are typically 2-3 times that of our model based on the Wells and Coppersmith (1994) relations. The fact that we do not consider down-dip variations in slip is indeed a limitation and is the main cause of our overestimate of the total rupture length (L_{10}) in this case.

One of the assumptions that we make in the methodology is that the earthquake is occurring on a predefined fault plane. To assess the significance of this assumption we simulated the real-time methodology for the Tohoku-Oki earthquake with a modified fault model, whose

orientation differs from the previous case with a change in strike and dip of 15° and a change rake of 20° . We found that moderate changes in the orientation of the fault like this do not lead to significant differences in the estimated magnitude and slip distribution (see Auxiliary Material of Colombelli, Allen, and Zollo 2013). A more serious source of error is when a dip-slip earthquake on an unidentified fault occurs in a strike-slip environment. The proposed methodology would most likely fail in this circumstance. For this reason it would be prudent to define an acceptance criteria that must be met before the finite-fault solution is used as part of an earthquake alert. One option might be to simultaneously solve for slip on different fault models (i.e., for strike-slip and dip-slip faults) and then let the RMSfit to the GPS data select the best fault model.

In the proposed methodology, the initial fault extent is defined based on the preliminary M_{NFPS} and this may represent a possible source of error. We evaluated this effect by simulating an underestimated initial magnitude. We performed this test on the Tohoku-Oki earthquake, by assuming that the initial M_{NFPS} was 6.0 and seeing how the self-adapting strategy responded (see Auxiliary Material of Colombelli, Allen, and Zollo 2013). After a few underestimated initial solutions (small magnitude, short lengths) the magnitude rapidly increases (in 4-5 s) while ~ 25 s are necessary for the methodology to expand the fault plane and recover a length similar to that of Figure 6.3.

In principle, there is no limitation to the practical applicability of the proposed methodology and no specific source-receiver configuration is required. As long as a good coverage and density of real-time GPS stations is available, the methodology is expected to be suitable for any seismically active area.

CONCLUSIONS AND PERSPECTIVES

The work presented in this thesis has been divided into three parts, which reflect different aspects of the common, central topic of Early Warning for large earthquakes. Methodological aspects, related to the real-time magnitude estimate and to the rapid prediction of the expected ground shaking, have been analyzed. At the same time, physical aspects of the rupture process initiation have been also investigated.

In the first part of the thesis, through the analysis of the 2011, M 9.0 Tohoku-Oki earthquake records, the feasibility of existing Early Warning methodologies for giant events has been studied.

In the second part of the work, different magnitude earthquakes have been analyzed and their behaviour in terms of beginning of the rupture process has been investigated.

Finally, in the third part of the thesis, two practical approaches for the prediction of the damaging effect of a large earthquake have been proposed. While the results of each analysis are already presented and

discussed in details within the chapters, a summary of the main results is reported below.

- **suitability of the existing methodologies:** the application of Early Warning methodologies to the Tohoku-Oki earthquake records has shown that the existing methodologies can be applied even to large events, provided that appropriate P-wave time windows are used. The empirical scaling relationships, which have been calibrated for small-to-moderate earthquakes, can be extended to large events, but longer portion of signals are required for a correct magnitude estimate.
- **evolutionary approach for the magnitude estimate:** two Early Warning parameters have been explored for the Tohoku-oki event. The initial peak displacement amplitude (P_d) and the average period (τ_c) have been both explored as a function of time. The analysis has shown that both parameters provide an evolutionary image of the ongoing fracture process and are informative about the event size, thus allowing for a real-time, evolutionary estimate of the earthquake magnitude;
- **expanding the P-wave time window and the distance range:** for the Tohoku-Oki earthquake, the use of small signal portions result is underestimated magnitude values; longer P-wave time windows are required for a reliable magnitude estimate. In particular, 25-30 seconds of P-wave signal are necessary to get a stable magnitude estimate of $M = 8.4$. The need of expanding the P-wave time window implies that records up to very large distances from the source have to be included;
- **time evolution of Early Warning parameters and source process:** the evolutionary approach has been applied to a larger data set earthquakes and has provided relevant insights on the possible relationship between Early Warning parameters and the source process. In particular, among the two analyzed parameters, the logarithm of τ_c has not shown a clear time dependency,

while the logarithm of P_d has shown a clear behaviour with time;

- **time evolution of peak displacement:** for all the analyzed earthquakes, the logarithm of the peak displacement starts with small initial values and then progressively increases until a final, stable value is reached. The initial increase has been found to be different between small and large events. In particular, the initial increase is very rapid for small events while a slower growth toward the final value is observed for large earthquakes. The initial evolution of logarithm of P_d with time is informative about the final size of the earthquake, thus suggesting a possible deterministic nature of earthquake rupture;
- **physical model for the rupture beginning:** a physical model for the rupture beginning has been proposed to justify the observed time evolution of logarithm of P_d . In particular, the variation of the initial slope of the logarithm of P_d vs. time curves has been interpreted in terms of differences in the friction during the nucleation phase of earthquakes. According to the proposed model, earthquakes breaking in a region with a large critical slip distance value have a larger probability to grow into a large size rupture than those originating in a region with a smaller slip distance value;
- **rapid estimate of the Potential Damage Zone:** a practical methodology for the real-time prediction of the potential damage area of an earthquake has been proposed. The methodology has been applied to ten strong Japanese events and to the megathrust Tohoku-Oki earthquake and has provided satisfying results. The comparison between the real-time predicted shaking maps and the post-event intensity distribution has shown that the real-time PDZ maps approximately correspond to the area where most of the damage is observed;

- **feasibility of Early Warning using continuous GPS data:** an innovative approach to earthquake Early Warning using continuous, 1Hz GPS data has been proposed. In the proposed approach, the coseismic ground deformation is used to provide fast and reliable magnitude estimates and approximate estimates of the extension of the source. The GPS approach has been tested using three earthquakes. The use of the GPS-based magnitude and of the finite fault extent improves the accuracy of ground shaking prediction, as compared to the existing seismology-based point source approaches. This approach would also facilitate more rapid tsunami warnings.

Among the overall results of this work, the magnitude-dependence of the initial slope of the logarithm of P_d vs. time curves is, undoubtedly, the most important result, both in terms of Early Warning applications and in terms of understanding the process of rupture initiation. The possibility to rapidly distinguish a small shock from a large event has an immediate, important impact on effectiveness of Early Warning Systems. However, the slope measured in this work is derived from the average trend of hundreds of records, spanning wide azimuth and distance ranges, while in real-time the availability of data depends on the source-station geometry. Further analyses are hence required to simulate the real-time data streaming and assess the minimum near-source data necessary to constrain the initial slope. Assuming that the slope is well constrained from near-source data, if the observed slope variation with magnitude is preserved even when a few data are used, a short time window (~ 1 s) can be enough for a rapid evaluation of the earthquake size.

Furthermore, a deeper investigation about the period parameter (τ_c) needs to be done. In the present work we aimed at understanding if both the peak displacement and the average period were related to the rupture process. While observing that the average period carries in-

formation about the event size, due to its unstable time behaviour and larger error (as compared to P_d), τ_c has not been deeply investigated and interpreted. Selected, high-quality data have to be explored to understand the role of this parameter during the rupture process.

SUPPORTING INFORMATION

A.1 Database description

The database consists of 43 moderate-to-strong earthquakes in the magnitude range $M4 \div 9$, located all over the Japanese active seismic region. To avoid any bias related to specific criteria for data selection (tectonic environment, dominant fault mechanism, aftershock/-mainshock, event depth, ...) we selected earthquakes occurred all over Japan, in different tectonic environments, both crustal and subcrustal events. We tried to avoid the inclusion of aftershocks belonging to the same sequence and tried to include events with different types of fault mechanism. Acceleration waveforms have been provided by K-Net and Kik-Net online databases (<http://www.kyoshin.bosai.go.jp/>). Table A.1 includes the list of the selected earthquakes and their source parameters. For earthquake waveforms extracted from K-Net and KiK-Net catalogues, the information concerning the event locations and magnitudes are provided by the JMA. By a comparison between the M_{JMA} and moment magnitude M_w , different authors (Dziewonski, Chou, and Woodhouse 1981; Katsumata 1996; Oth et al. 2010) have found negligible differences between the two scales the magnitude range 4 to 8. Here we simply denote magnitude as M .

Event Date	Event Time	Lon (°)	Lat (°)	Depth (km)	M
2003-09-26	04:50:00	144.074	41.781	42	8.0
2003-09-26	06:08:00	143.691	41.710	21	7.1
2008-05-08	01:45:00	141.607	36.227	51	7.0
2008-06-14	08:43:00	140.880	39.028	8	7.2
2010-03-29	10:29:00	139.882	36.035	43	4.3
2010-05-01	18:20:00	139.190	37.558	9	4.9
2010-07-21	06:19:00	135.693	34.205	58	5.1
2010-10-24	13:50:00	139.852	36.058	45	4.4
2010-11-05	19:14:00	139.842	36.062	45	4.6
2011-03-11	14:46:00	142.860	38.103	24	9.0
2011-03-12	03:59:00	138.597	36.985	8	6.7
2011-03-19	18:56:00	140.570	36.783	5	5.8
2011-03-23	07:12:00	140.787	37.083	8	5.0
2011-04-01	20:58:00	142.165	39.335	45	5.9
2011-04-11	17:16:00	140.672	36.945	6	6.4
2011-04-11	20:42:00	140.633	36.965	11	5.7
2011-04-12	14:07:00	140.643	37.052	15	5.0
2011-04-26	21:12:00	139.975	36.085	46	6.0
2011-06-18	20:31:00	141.820	37.617	28	5.5
2011-06-23	06:51:00	142.590	39.947	36	5.6
2011-07-08	03:35:00	141.128	37.097	55	6.3
2011-07-25	03:51:00	141.627	37.708	46	6.2
2011-07-31	03:54:00	141.220	36.902	57	6.1
2011-09-15	17:00:00	141.483	36.255	51	5.2
2011-09-17	04:26:00	143.085	40.258	7	4.4
2011-09-21	22:30:00	140.577	36.737	9	5.3
2011-11-20	10:23:00	140.587	36.710	9	4.9
2012-01-12	12:20:00	141.303	36.967	33	5.4
2012-01-28	07:39:00	138.978	35.492	18	4.7
2012-01-28	07:43:00	138.977	35.488	18	4.7
2012-01-29	16:46:00	138.983	35.537	21	5.2
2012-02-11	10:27:00	139.788	36.087	46	5.3
2012-03-01	07:32:00	140.625	36.438	56	5.4
2012-03-27	20:00:00	142.333	39.805	21	4.8
2012-05-05	18:56:00	137.173	35.188	45	6.5
2012-05-18	17:19:00	139.840	36.135	51	5.1
2012-06-01	17:48:00	139.875	36.027	44	4.5
2012-06-09	04:07:00	138.368	35.023	26	4.2
2012-06-17	16:13:00	140.010	36.178	51	4.8
2012-07-12	13:54:00	139.885	36.082	46	4.6
2012-07-16	04:31:00	139.817	36.152	52	4.1
2012-08-03	22:19:00	139.898	36.025	43	5.6
2012-08-30	04:17:00	139.850	36.120	49	4.5

Table A.1: List of the selected earthquakes and source parameters. For each event information are provided by the Japan Meteorological Agency.

A.2 Description of data processing

In order to obtain displacement waveforms, the mean value and linear trend are first removed from the raw acceleration data. These are then double integrated and a non-causal, high-pass Butterworth filter with cut-off frequency of 0.075 Hz is applied to remove the artificial long-period trend and baselines introduced by the double integration operation. The P-wave onset times have been manually picked on each vertical component of accelerometer records. The peak displacement is measured in a recursive manner, starting from 0.05 s after the P-wave onset and moving forward with a time step of 0.05 s. To avoid the inclusion of S-waves into the considered P-wave Time Window (PTW), we computed the expected S-wave arrival time at each station (T_S) using the following relation:

$$T_S - T_P = b \cdot R \quad (\text{A.1})$$

where T_P is the observed P-wave onset time, R is the hypocentral distance and $b = 0.088$. The coefficient b has been derived through a linear regression analysis, after manually picking the S-wave arrival times for a selected number of records in our data-set.

To compare the observed P_d values at different stations, the geometrical attenuation effect has been corrected with the following attenuation relationship:

$$\log P_d = A + B \cdot M + C \cdot \log R \quad (\text{A.2})$$

where M is the event magnitude, P_d is measured in cm (in a fixed time window of 3 seconds) and the hypocentral distance R is measured in km. In the above equation a single term ($\log R$) is used to account for both the geometrical spreading and the anelastic attenuation.

For earthquakes with $M < 7$ we used only data up to a maximum hypocentral distance of 200 km, while for $M \geq 7$ we included records up to 500 km. We preliminary estimated the coefficients A, B, C of

Coefficient	$M < 7; R \leq 200\text{km}$	$M \geq 7; R \leq 500\text{km}$
A	-2.89 ± 0.12	-2.24 ± 0.12
B	0.62 ± 0.01	0.59 ± 0.01
C	-1.25 ± 0.06	-1.51 ± 0.02

Table A.2: List of the coefficients. Coefficient of equation A.2 for different magnitude and distance ranges.

equation for each distance range, through a non-weighted, linear, regression analysis. Then, depending on the magnitude and the distance range, we used the appropriate coefficients to compare the observed Pd values at different stations. Table A.2 shows the coefficients A , B , C for each magnitude and corresponding distance range. For each event we set a maximum PTW to be explored, based on the expected duration of the source from kinematic models for the corresponding magnitude, and considered at least twice the expected duration. To compute the average LPDT curve, we also required at least 5 data to be used in each PTW. The average computation stops either when the number of data is not sufficient, or when the PTW reaches its maximum time limit, whichever condition comes first.

A.3 Resolution and tests

To assess the reliability and robustness of the results, we identified different factors that could have influenced the observed shape of the LPDT curves. Among them, the high-pass filtering operation, the propagation effects and the source depth, are the most relevant. Hence, we separately investigated each of these factors to understand their influence on the analysis.

A.3.1 Filter effect

Because the corner frequency of the event depends on the magnitude, the high-pass filtering operation may distort the recorded waveforms, eventually resulting in an artificial variation of the initial slope of LPDT curves. We performed two tests to exclude that the observed trend of T1, B1, T2 and B2 with magnitude is an artificial effect of the high-pass filtering operation.

First we repeated the entire analysis using unfiltered velocity and acceleration records. With the same approach as used for P_a , we measured the initial Peak Velocity (P_v) and the initial Peak Acceleration (P_a) and obtained the corresponding log. P_v vs. PTW and log. P_a vs. PTW curves. We fitted these curves and estimated T1, B1, T2, B2 parameters. Figure A.1 shows that the scaling of these parameters with magnitude is preserved even when unfiltered acceleration or velocity records are used.

A second test consists in the use of different cut-off frequencies for the high-pass filtering operation on displacement waveforms. We tested 0.01 Hz, 0.075 Hz, 0.1 Hz and 0.5 Hz. For each filter we obtained the LPDT curves and estimated T1, B1, T2 and B2 parameters. Figure A.2 shows the fit parameters as a function of magnitude using different cut-off frequencies for the filter. The trend of parameters with magnitude is preserved when different filters are used.

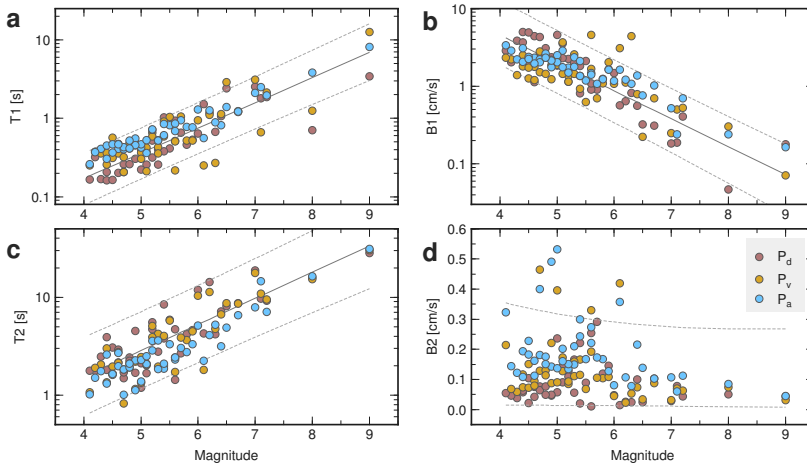


Figure A.1: Filter effect on fit parameters T1, B1, T2, B2. The figure shows the four parameters resulting from the fitting procedure as a function of magnitude using filtered displacement waveforms (brown circles), unfiltered velocity waveforms (yellow circles) and unfiltered acceleration records. In all panels the solid gray line shows the linear best fit function when the cut-off frequency of 0.075 Hz is used and the thin dashed lines are the corresponding 95% confidence bounds for new observations.

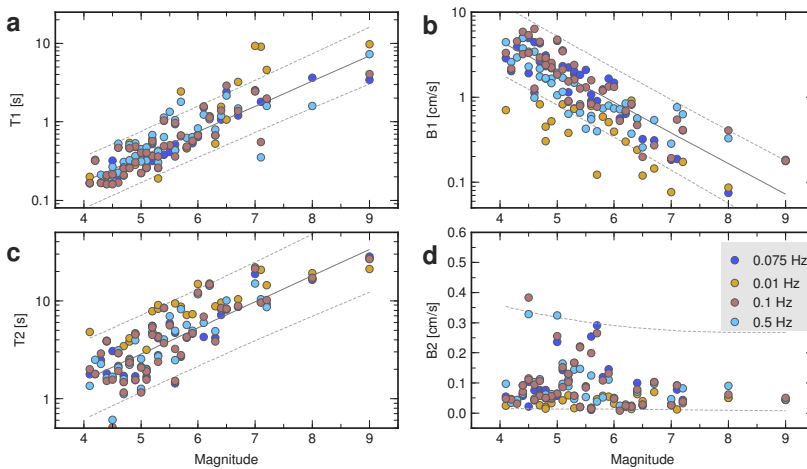


Figure A.2: Filter effect on fit parameters T1, B1, T2, B2. Same as Figure A.1 but using different cut-off frequencies for the high-pass filtering operation on displacement waveforms: 0.075 Hz (dark blue circles), 0.01 Hz (yellow circles), 0.1 Hz (brown circles) and 0.05 Hz (light blue circles).

A.3.2 Distance effect

The initial P-wave amplitude may be strongly affected by all the propagation effects related to crustal structure, geometrical spreading and anelastic attenuation. In addition to this, we must consider that in our analysis, due to the natural amplitude decay with distance and magnitude, for the largest events P_d is measured up to larger hypocentral distances (> 200 km). Moreover the largest events in our database are mostly offshore earthquakes associated to the subduction zone. An intrinsic bias due to distance-attenuation and multipathing could therefore affect the results of this analysis. A further source of error can be the distance correction of P_d , which is necessary to compare records at different stations. As a matter of fact, an inadequate distance correction (i.e., an inadequate coefficient C equation A.2) could influence the initial slope variation of $\log P_d$ curves.

To understand if these effects are contributing to (and are responsible of) the different initial slope, we looked at different events in the same distance range. We prior determined the coefficients A, B, C of equation A.2 for each distance range (i.e., 0-100km, 0-200km, 100-200km, 0-500km); we then corrected P_d using the appropriate coefficient for each distance and fitted the LPDT curves to determined T1 and B1. Figure A.3 shows the two parameters as a function of magnitude and of the distance range.

Assuming that T1 and B1 depend on both magnitude and distance, we would expect to see an evident (and systematic) variation when a different distance range is used. This effect, instead, is not evident from the plot, suggesting that the observed trend with magnitude is not controlled by the distance range. The trend of T1 and B1 with magnitude is preserved even when restricting the average to a smaller distance range, although it is evident but less pronounced when looking at larger distances, due to the poor magnitude coverage.

Furthermore, if the anelastic attenuation was responsible of the ob-

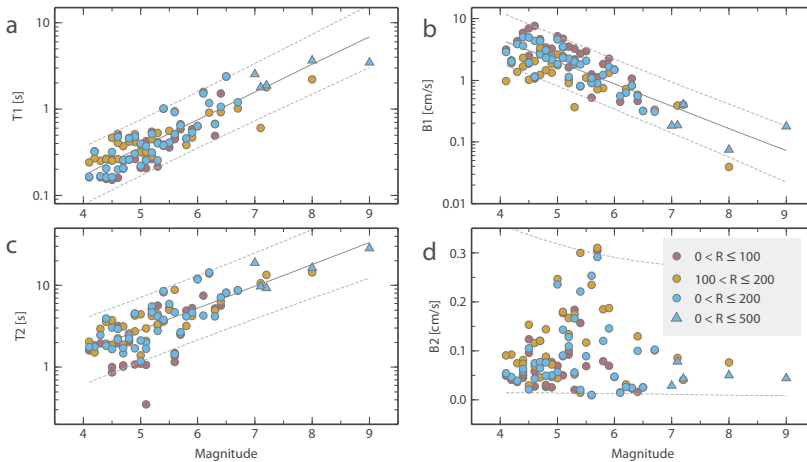


Figure A.3: Distance effect on fit parameters T1, B1, T2, B2. Same as Figure A.1 but using different distance ranges for the average $\log P_d$ computation: 0-100 km (brown circles), 100-200 km (yellow circles), 0-200 km (light blue circles) and 0-500 km (light blue triangles). In all panels the solid gray line shows the linear best fit function when the cumulative ranges are used (0-200 km for $M < 7$ and 0-500 km for $M \geq 7$).

served T1 and B1 trend with M we would expect an increase of the initial slope with magnitude, since higher frequencies attenuate more rapidly, as opposed to the observed behaviour. A more realistic situation in our analysis is that, because higher frequencies are mostly recorded at small distances while lower frequencies are mainly associated to long distances, the overall anelastic attenuation effect is averaged out.

Another issue is the azimuthal variation of displacement amplitude which in case of only few stations available may introduce variability of the LPDT curves. The average on a large number of data (i.e. hundreds of stations, as done in our analysis) is generally expected to reduce the influence of the radiation pattern.

Finally, we considered that averaging the displacement amplitude over a wide range of distances may result in the inclusion of different P-arrivals within the considered PTW (i.e., Pn, Pg phases) thus possibly

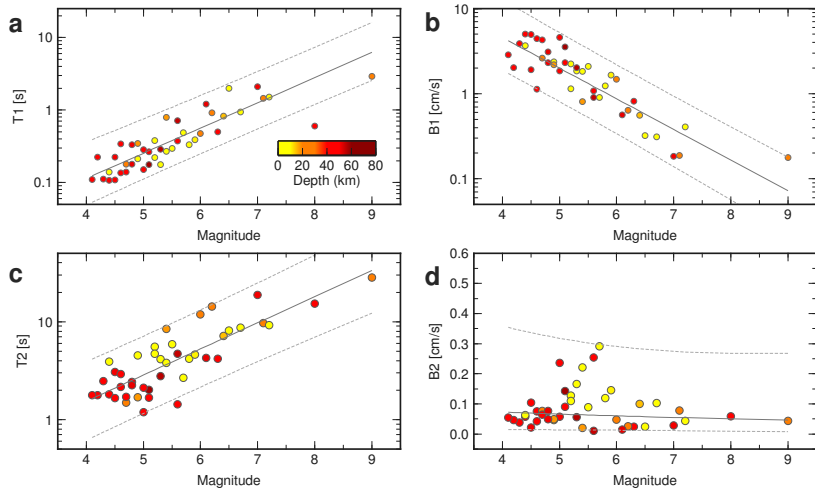


Figure A.4: Source depth effect on fit parameters $T1$, $B1$, $T2$, $B2$. Same as Figure A.1 with a color scale representing the source depth.

affecting the slope estimate. The results of Figure A.3 show that the trend of $T1$ and $B1$ with magnitude is preserved even when restricting the average to a smaller distance range where a single P-wave arrival is expected.

A.3.3 Source depth effect

The earthquake depth might impact on source processes and frictional properties and therefore on the observation about the evolution of P-wave peak displacement with time. The scatter plot of Figure 3.1c shows that there is no magnitude-depth dependence for the earthquakes in our database. Thus, the observed trend of parameters should not be influenced by the frictional processes occurring at different depths. To clarify this point, in figure A.4 we plotted the fit parameters as a function of magnitude, with a color scale representing the event depth. We did not find any clear evidence that the source depth may affect the initial P-wave displacement evolution.

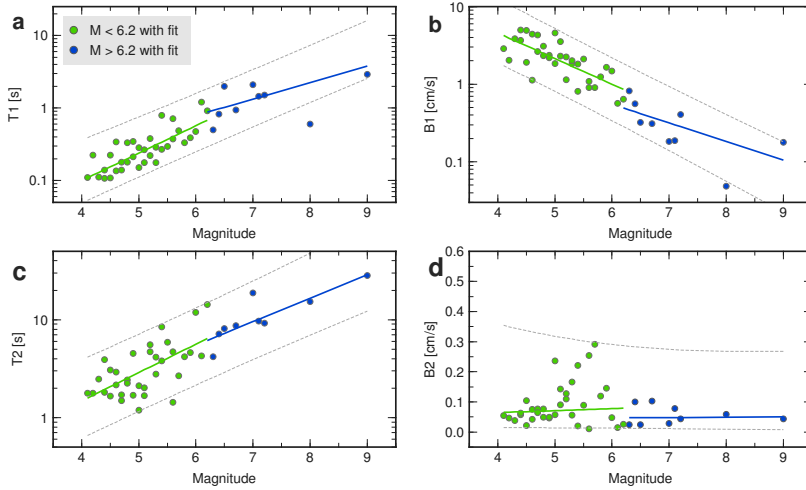


Figure A.5: Validation of the linear trend. Same as figure A.1. Blue circles are the $M \geq 6.2$ data with their linear fit line (blue solid line). Green circles are the $M < 6.2$ data with the best fit line (green solid line).

A.4 Validation of the linear trend

The log-linear correlation of T1 and B1 parameters with magnitude is robust and evident when looking at the whole magnitude range, although a clear variability of data appears from the plot (Figure 4.2a,b). The magnitude-dependency of T1 and B1 is not so clear for magnitude larger than 6.2-6.5, although the variability of T1 values for the largest earthquakes (i.e., for $M = 7 - 7.2$) is comparable to the variability observed for any other magnitude ranges. The weaker, linear trend for the parameter T1 for $M \geq 6.2$ is due to the limited number of available events in this range and to the scatter of data. To validate the hypothesis that a linear trend does exist for the largest magnitudes, in figure A.5 we plotted the best fit line obtained for $M \geq 6.2$ (blue solid line) and the best fit line obtained for magnitude $M < 6.2$ (green solid line). We found that the linear trend for $M \geq 6.2$ is consistent with the one for the whole magnitude range, within the error bars.

A.5 Residual analysis

To compare the observed P_d at different stations, a standard Ground Motion Prediction Equation (in the form of equation A.2) has been used. To show that the attenuation relationship does not introduce any bias, we plotted the residuals $\log P_{d(\text{observed})} - \log P_{d(\text{predicted})}$ as a function of distance and magnitude and the histograms of the residuals in different magnitude classes. Figure A.6 (top panel) shows that residuals are distributed around zero in the whole distance range and no evident bias appears neither from the scatter plot, nor from the histograms (right panel). A similar behaviour is observed in the plot of residuals as a function of magnitude (bottom panel). Also in this case we found that residuals are distributed around zero, except for the case of the *M*9.0 Tohoku-Oki earthquake.

For this single event, the deviation from the zero value is related to the problem of parameter saturation, when a short PTW is used to estimate the magnitude. For the case of the Tohoku-Oki event, the use of a fixed PTW of 3 seconds, results in significantly lower initial peak displacement values. It is worth to note, however, that no evident bias appears from the residual vs. distance plot. To correct P_d values for the distance effect, only the distance contribution is used. If a bias effect with magnitude would exist, it will not affect the slope of LPDT curves.

A.6 Dependency on the fit model

The observed variation of the initial slope of P_d for different magnitude earthquakes (i.e., the trend of B1 vs. M) appears evident from a visual inspection of the curves, without using any fitting procedure. To assess in a quantitative way the initial behaviour of the curves, we fit the P_d vs. time curves using a piecewise linear function and determined 5

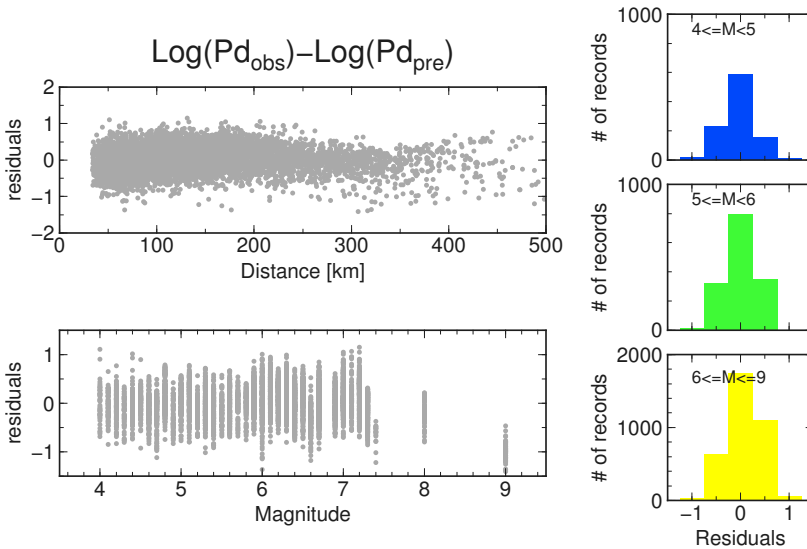


Figure A.6: Residual distribution. The figure shows the difference between the logarithm of the observed P_d and the logarithm of the predicted P_d as a function of distance (top) and magnitude (bottom). Right panel shows the histograms of the residuals in different magnitude classes.

best fit parameters, for each event. The agreement between data and fit function is very high and the parameter estimates are accurate in terms of errors. In particular, the first corner time T1, is estimated as the intersection of two straight lines, whose slope is well constrained (as shown by the fit examples in Figure A.7 below). However, the use of a 3-piecewise function might introduce some bias in the estimate of B1 and T1. For this reason, we carried out a further analysis.

For each event we stopped the P_d curve at its saturation time (T2) and used a 2-piecewise, linear function to fit the data. Figure A.7 shows example of fitted curves with a 2-piecewise linear function while Figure A.8 shows that the new estimates of T1 and B1 are consistent with those obtained by fitting the entire curve evolution, confirming that the final part of the curves does not significantly contaminate the estimates of T1 and B1.

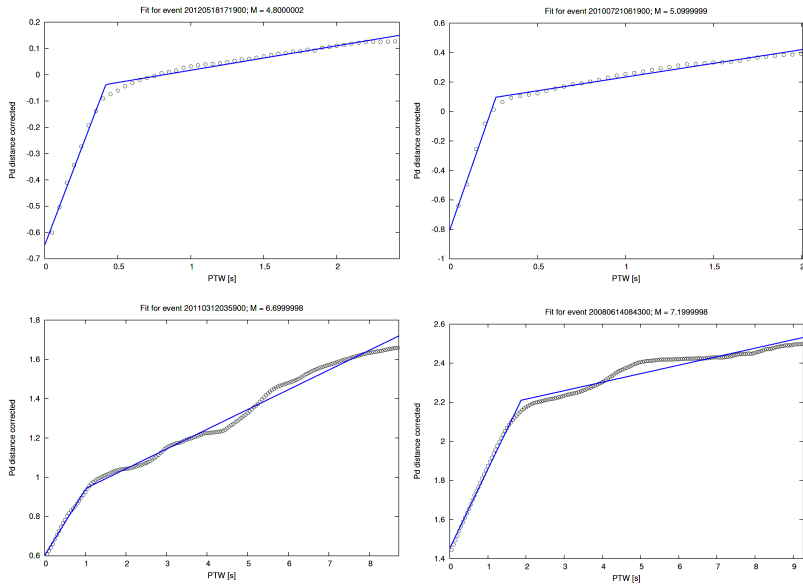


Figure A.7: Example of data fitting. The figure shows examples of LPDT curves as a function of the P-wave time window and the 2-piecewise best fit function. Grey empty circles are the data while the blue solid line is the best fit function.

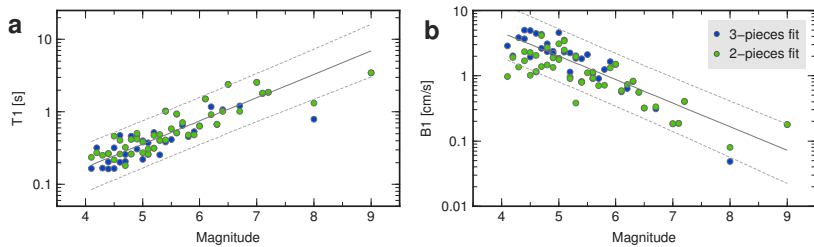


Figure A.8: Fit parameters $T1$, 1 , $T2$, $B2$ with a 2-piecewise function. The figure shows the two initial parameters resulting from the fitting procedure with a 2-piecewise linear function, as a function of magnitude. In both panels the blue circles are the initial fit parameters using a 3-piecewise model, while green circles are the initial fit parameters using a 2-piecewise model.

DATA AND RESOURCES

All the acceleration waveforms used in this study were extracted from the KiK-net and K-NET online databases (<http://www.kyoshin.bosai.go.jp/>).

For the 2011 Tohoku-Oki earthquake raw 1Hz GPS data were collected by the Japanese GPS Earth Observation Network (GEONET) stations (Sagiya 2004). Point-positions were provided by the Pacific Northwest Geodetic Array at central Washington University and were computed using GIPSY 6 and final satellite ephemerides and clock corrections provided by the Jet Propulsion Laboratory. For the 2003 Tokachi-Oki earthquake and the 2010 El Mayor-Cucapah earthquake the raw 1Hz GPS data were collected by GEONET and California Real-time Network (CRTN) stations, respectively. Both data sets are the same used by Crowell, Bock, and Melgar (2012).

The Japanese Intensity data for the events analyzed in Chapter 5 were provided by the Annual Bulletin of Japan (2008), published by the Japan Meteorological Agency. We thank Drs. Mitsuyuki Hoshihara and Nobuo Hamada for making us available the JMA intensity data.

For this study, the displacement waveforms were stored and analyzed in SAC (Seismic Analysis Code) format (Goldstein et al. 2003). Most of the analyses were made using the GNU PLOT, MATLAB (MATLAB version 6.5.1, 2003, computer software, The MathWorks Inc., Natick, Massachusetts) and GMT (Generic Mapping Tools) softwares (Wessel

and Smith 1995).

This work was funded by the University of Bologna Alma Mater Studiorum, the University of Naples Federico II, and a grant to UC Berkeley from the Gordon and Betty Moore Foundation. This research was carried out in the framework of REAKT Project (Strategies and tools for Real-Time EArthquake RiSk ReducTion) founded by the European Community via the Seventh Framework Program for Research (FP7), contract 282862.

BIBLIOGRAPHY

- Aki, K. and P.G. Richard (2002). *Quantitative Seismology, second edition*. University Science Books.
- Alcik, H. et al. (2009). “A study on warning algorithms for Istanbul earthquake early warning system”. In: *Geophys. Res. Lett.* 36.
- Allen, R. M. and H. Kanamori (2003). “The potential for earthquake early warning in southern California.” In: *Science (New York, N.Y.)* 300.5620, pp. 786–789. DOI: [10.1126/science.1080912](https://doi.org/10.1126/science.1080912).
- Allen, R. M. and A. Ziv (2011). “Application of real-time GPS to earthquake early warning”. In: *Geophysical Research Letters* 38.
- Allen, R. M. et al. (2009a). “Real-time earthquake detection and hazard assessment by ElarmS across California”. In: *Geophys. Res. Lett.* 36. DOI: [10.1029/2008GL036766](https://doi.org/10.1029/2008GL036766).
- Allen, R. M. et al. (2009b). “The Status of Earthquake Early Warning around the World: An Introductory Overview”. In: *Seismological Research Letters* 80.5, pp. 682–693. DOI: [10.1785/gssrl.80.5.682](https://doi.org/10.1785/gssrl.80.5.682).
- Allen, R. V. (1978). “Automatic earthquake recognition and timing from single traces”. In: *Bulletin of the Seismological Society of America* 68, pp. 1521–1532.
- Ampuero, J. P., J. P. Vilotte, and F. J. Sánchez-Sesma (2002). “Nucleation of rupture under slip dependent friction law: Simple models of fault zone”. In: *J. Geophys. Res.* 107, p. 2324.

- Andrews, D.J. (1976). “Rupture Velocity of Plane Strain Shear Crack”. In: *J. Geophys. Res.* 81, pp. 5679–5687.
- Beroza, G.C. and W.L. Ellsworth (1996). “Properties of the seismic nucleation phase”. In: *Tectonophysics* 261, pp. 209–227.
- Bock, Y., D. Melgar, and B. W. Crowell (2011). “Real-time strong-motion broadband displacements from collocated GPS and accelerometers”. In: *Bull.Seismol. Soc. Am.* 101, pp. 2904–2925. DOI: [10.1785/0120110007](https://doi.org/10.1785/B0120110007).
- Boore, D. M., W. B. Joyner, and T. E. Fumal (1997). “Equations for estimating horizontal response spectra and peak acceleration from western North American earthquakes: A summary of recent work”. In: *Seismol. Res. Lett.* 68, pp. 128–153.
- Boore, D.M., C.D. Stephens, and W.B. Joyner (2002). “Comments on Baseline Correction of Digital Strong-Motion Data: Examples from the 1999 Hector Mine, California earthquake”. In: *Bull.Seism. Soc. Am.* 92.4, pp. 1543–1560.
- Böse, M., C. Ionescu, and F. Wenzel (2007). “Earthquake early warning for Bucharest, Romania: Novel and revised scaling relations”. In: *Geophysical Research Letters* 34.7, pp. 1–6. DOI: [10.1029/2007GL029396](https://doi.org/10.1029/2007GL029396).
- Böse, M. et al. (2009). “Real-time testing of the on-site warning algorithm in Southern California and its performance during the July 29, 2008 Mw 5.4 Chino Hills earthquake”. In: *Geophys. Res. Lett.* 36. DOI: [10.1029/2008GL036366](https://doi.org/10.1029/2008GL036366).
- Carlson, R. L. and G. S. Raskin (1984). “Density of the ocean crust”. In: *Nature* 311, pp. 555–558.
- Carranza, M. et al. (2013). “Earthquake early warning for southern Iberia: A P wave threshold-based approach”. In: *Geophys. Res. Lett.* 40. DOI: [10.1002/grl.50903](https://doi.org/10.1002/grl.50903).
- Colombelli, S., R. M. Allen, and A. Zollo (2013). “Application of real-time GPS to earthquake early warning in subduction and strike-slip

- environments”. In: *JGR* 118, pp. 3448–3461. DOI: [10.1002/jgrb.50242](https://doi.org/10.1002/jgrb.50242).
- Colombelli, S. et al. (2012a). “Early magnitude and potential damage zone estimates for the great Mw 9 Tohoku-Oki earthquake”. In: *Geophys. Res. Lett.* 39. DOI: [10.1029/2012GL053923](https://doi.org/10.1029/2012GL053923).
- Colombelli, S. et al. (2012b). “Test of a Threshold-Based Earthquake Early Warning Using Japaned Data”. In: *Bull. Seism. Soc. Am.* 102, pp. 1266–1275. DOI: [10.1785/0120110149](https://doi.org/10.1785/0120110149).
- Crowell, B. W., Y. Bock, and D. Melgar (2012). “Real-time inversion of GPS data for finite fault modeling and rapid hazard assessment”. In: *Geophys. Res. Lett.* 39. DOI: [10.1029/2012GL051318](https://doi.org/10.1029/2012GL051318).
- Crowell, B. W., Y. Bock, and M. B. Squibb (2009). “Demonstration of earthquake early warning using total displacement waveforms from real-time GPS networks”. In: *Seismol. Res. Lett.* 80, pp. 772–782. DOI: [10.1785/gssrl.80.5.772](https://doi.org/10.1785/gssrl.80.5.772).
- Das, S. and C.H. Scholz (1982). “Theory of time-dependent rupture in the Earth”. In: *J. Geophys. Res.* 86, pp. 6039–6051.
- Dasgalaou, C., I. R. Ionescu, and M. Campillo (2000). “Fault finiteness and initiation of dynamic shear instability”. In: *Earth Planet. Sci. Lett.* 177, pp. 163–176.
- Dieterich, J.H. (1979). “Modeling of rock friction: 1 Experimental results and constitutive equations”. In: *J. Geophys. Res.* 84, pp. 2161–2168.
- (1986). “A model for the nucleation of earthquake slip”. In: *Earthquake Source Mechanics*. Ed. by S. Das, J. Boatwright, and C.H. Scholz. Advanced Technologies in Earth Sciences. Am. Geophys. Union, pp. 37–47.
- Dziewonski, A. M., T. A. Chou, and J. H. Woodhouse (1981). “Determination of earthquake source parameters from waveform data for studies of global and regional seismicity”. In: *J. Geophys. Res.* 86, pp. 2825–2852.

- Ellsworth, W.L. and G.C. Beroza (1995). “Seismic Evidence for an Earthquake Nucleation Phase”. In: *Science* 268.
- Espinosa-Aranda, J. M. et al. (2009). “Evolution of the Mexican Seismic Alert System (SASMEX)”. In: *Seismological Research Letters* 80, pp. 694–706.
- Festa, G., A. Zollo, and M. Lancieri (2008). “Earthquake magnitude estimation from early radiated energy”. In: *Geophysical Research Letters* 35.22, pp. 2–7. DOI: [10.1029/2008GL035576](https://doi.org/10.1029/2008GL035576).
- Goldstein, P. et al. (2003). “SAC2000: Signal processing and analysis tools for seismologists and engineers”. In: *IASPEI International Handbook of Earthquake and Engineering Seismology*.
- Hanks, T. and H. Kanamori (1979). “A moment magnitude scale”. In: *J. geophys. Res* 84, pp. 2348–2350. DOI: [10.1029/JB084iB05p02348](https://doi.org/10.1029/JB084iB05p02348).
- Hashimoto, C. et al. (2009). “Interplate seismogenic zones along the Kuril-Japan trench inferred from GPS data inversion”. In: *Nat. Geosci.* 2, pp. 141–144.
- Hauksson, E. et al. (2010). “The 2010 Mw 7.2 El Mayor-Cucapah earthquake sequence, Baja California, Mexico and southernmost California, USA: Active seismotectonics along the Mexican Pacific margin”. In: *Pure Appl. Geophys.* 168, pp. 1255–1277. DOI: [10.1007/s00024-010-0209-7](https://doi.org/10.1007/s00024-010-0209-7).
- Holland, J. H. (1975). “Adaptation in Natural and Artificial Systems”. In: *Univ. of Mich. Press, Ann Arbor*. DOI: [10.1029/2003GL019150](https://doi.org/10.1029/2003GL019150).
- (1992). “Genetic algorithms”. In: *Sci. Am.* 267, pp. 66–72. DOI: [10.1029/2003GL019150](https://doi.org/10.1029/2003GL019150).
- Honda, R. et al. (2004). “Ground motion and rupture process of the 2003 Tokachi-Oki earthquake obtained from strong motion data of K-net and KiK-net”. In: *Earth, Planets and Space* 56, pp. 317–322. DOI: [10.5047/eps.2011.05.034](https://doi.org/10.5047/eps.2011.05.034).
- Honda, R. et al. (2011). “A complex rupture image of the 2011 off the Pacific coast of Tohoku Earthquake revealed by the MeSO-net”. In:

- Earth, Planets and Space* 63.7, pp. 583–588. DOI: [10.5047/eps.2011.05.034](https://doi.org/10.5047/eps.2011.05.034).
- Horiuchi, S. et al. (2005). “An automatic processing system for broadcasting system earthquake alarms”. In: *Bull. Seismol. Soc. Am.* 95, pp. 347–353.
- Hoshiya, M. et al. (2011). “Outline of the 2011 off the Pacific coast of Tohoku Earthquake (Mw 9.0) Earthquake Early Warning and observed seismic intensity”. In: *Earth, Planets and Space* 63.7, pp. 547–551. DOI: [10.5047/eps.2011.05.031](https://doi.org/10.5047/eps.2011.05.031).
- Ida, Y. (1972). “Cohesive force across tip of a longitudinal shear crack and the Griffith’s specific surface energy”. In: *J. Geophys. Res.* 77, pp. 3796–3805.
- Ide, S., A. Baltay, and G. C. Beroza (2011). “Shallow dynamic overshoot and energetic deep rupture in the 2011 Mw 9.0 Tohoku-Oki earthquake.” In: *Science (New York, N.Y.)* 332.6036, pp. 1426–9. DOI: [10.1126/science.1207020](https://doi.org/10.1126/science.1207020).
- Iinuma T., et al. (2011). “Coseismic slip distribution of the 2011 off the Pacific Coast of Tohoku Earthquake (M9.0) refined by means of seafloor geodetic data”. In: *Geophys. Res. Lett.* 117. DOI: [10.1029/2012JB009186](https://doi.org/10.1029/2012JB009186).
- Irwan, M. et al. (2004). “Measuring ground deformation with 1-Hz GPS data: The 2003 Tokachi- Oki earthquake (preliminary report).” In: *Earth Planets Space* 56, pp. 389–393.
- Ishii, M. (2011). “High-frequency rupture properties of the Mw 9.0 Off the Pacific Coast of Tohoku Earthquake”. In: *Earth, Planets, and Space* 63, pp. 609–614.
- Ito, T., S. Yoshioka, and S. Miyazaki (2000). “Interplate coupling in northeast Japan deduced from inversion analysis of GPS data”. In: *Earth Planet. Sci. Lett.* 176, pp. 117–130.
- Joyner, W. B. and D. M. Boore (1981). “Peak horizontal acceleration and velocity from strong-motion records including records from the

- 1979 Imperial Valley, California, earthquake". In: *Bull. Seismol. Soc. Am.* 71.9, pp. 2011–2038. DOI: [10.1002/eqe.675](https://doi.org/10.1002/eqe.675).
- Kanamori, H. (2005). "REAL-TIME SEISMOLOGY AND EARTHQUAKE DAMAGE MITIGATION". In: *Annual Review of Earth and Planetary Sciences* 33.1, pp. 195–214. DOI: [10.1146/annurev.earth.33.092203.122626](https://doi.org/10.1146/annurev.earth.33.092203.122626).
- Kanamori, H. and E.E. Brodsky (2004). "The physics of earthquakes". In: *Rep. Prog. Phys.* 67, pp. 1429–1496.
- Kanasewich, E. R., C. D. Hemmings, and T. Alpaslan (1973). "Nth-root stack nonlinear multichannel filter." In: *Geophysics* 38, pp. 327–338.
- Kaneko, Y. and J.-P. Ampuero (2011). "A mechanism for preseismic steady rupture fronts observed in laboratory experiments". In: *Geophys. Res. Lett.* 38.
- Katsumata, A. (1996). "Comparison of magnitudes estimated by the Japan Meteorological Agency with moment magnitudes for intermediate and deep earthquakes". In: *Bull. Seismol. Soc. Am.* 86, pp. 832–842.
- Kinoshita, S. and M. Takagishi (2011). "Generation and propagation of static displacement estimated using KiK-net recordings". In: *Earth Planets Space* 63, pp. 779–783. DOI: [10.5047/eps.2011.05.003](https://doi.org/10.5047/eps.2011.05.003).
- Koketsu, K. et al. (2004). "Joint inversion of strong motion and geodetic data for the source process of the 2003 Tokachi-Oki, Hokkaido, earthquake". In: *Earth Planets Space* 55, pp. 329–334.
- Koketsu, K. et al. (2011). "A unified source model for the 2011 Tohoku Earthquake". In: *Earth Planet. Sci. Lett.* 310, pp. 480–487.
- Koper, K. D., A. R. Hutko, and T. Lay (2011). "Along-dip variation of teleseismic short-period radiation from the 11 March 2011 Tohoku earthquake (Mw 9.0)". In: *Geophys. Res. Lett.* 38.

- Kruger, F. and M. Ohrnberger (2005). “Tracking the rupture of the Mw 5.9 Sumatra earthquake over 1,150 km at teleseismic distance”. In: *Nature* 435.2, pp. 937–939.
- Kurahashi, S. and K. Irikura (2011). “Source model for generating strong ground motions during the 2011 off the Pacific coast of Tohoku Earthquake”. In: *Earth, Planets and Space* 63.7, pp. 571–576. DOI: [10.5047/eps.2011.06.044](https://doi.org/10.5047/eps.2011.06.044).
- Lancieri, M. and A. Zollo (2008). “A Bayesian approach to the real-time estimation of magnitude from the early P and S wave displacement peaks”. In: *Journal of Geophysical Research* 113.B12, pp. 1–17. DOI: [10.1029/2007JB005386](https://doi.org/10.1029/2007JB005386).
- Lee, S.-J. et al. (Oct. 2011). “Evidence of large scale repeating slip during the 2011 Tohoku-Oki earthquake”. In: *Geophysical Research Letters* 38.19, pp. 1–6. DOI: [10.1029/2011GL049580](https://doi.org/10.1029/2011GL049580).
- Maercklin, N. et al. (2012). “Twin ruptures grew to build up the giant 2011 Tohoku, Japan, earthquake”. In: *Sci. Rep.* 2. DOI: [10.1038/srep00709](https://doi.org/10.1038/srep00709).
- Meng, L., A. Inbal, and J.-P. Ampuero (2011). “A window into the complexity of the dynamic rupture of the 2011 Mw 9 Tohoku-Oki earthquake”. In: *Geophys. Res. Lett.* 38.
- Meng, L. et al. (2012). “Mitigating artifacts in backprojection source imaging with implications on frequency-dependent properties of the Tohoku-Oki earthquake”. In: *Earth, Planets, and Space* 64.12, pp. 1101–1109. DOI: [10.5047/eps.2012.05.010](https://doi.org/10.5047/eps.2012.05.010).
- Midorikawa, S., K. Fujimoto, and I. Muramatsu (1999). “Correlation of new J.M.A. instrumental seismic intensity with former J.M.A. seismic intensity and ground motion parameters [in Japanese]”. In: *J. Inst. Social Saf. Sci.* 1, pp. 51–56. DOI: [10.1785/0120110156](https://doi.org/10.1785/0120110156).
- Miura, S. et al. (2004). “The 2003 M8.0 Tokachi-Oki earthquake: How much has the great event paid back slip debts?” In: *Geophys. Res. Lett.* 31, pp. 317–322. DOI: [10.1029/2003GL019021](https://doi.org/10.1029/2003GL019021).

- Nakamura, Y. (1984). “Development of the earthquake early-warning system for the Shinkansen, some recent earthquake engineering research and practical in Japan”. In: *The Japanese National Committee of the International Association for Earthquake Engineering*, pp. 224–238.
- (1988). “On the urgent earthquake detection and alarm system (UrEDAS)”. In: *Proceedings of 9th World Conference on Earthquake Engineering, Tokyo-Kyoto, Japan*, pp. 673–678.
- Nielsen, S., J. Taddeucci, and S. Vinciguerra (2010). “Experimental observation of stick-slip instability fronts”. In: *Geophys. J. Int.* 180, pp. 697–702.
- Odaka, T. et al. (2003). “A new method of quickly estimating epicentral distance and magnitude from a single seismic record”. In: *Bulletin of the Seismological Society of America* 93, pp. 526–532.
- Ohnaka, M. (1996). “Nonuniformity of the Constitutive Law Parameters for Shear Rupture and Quasistatic Nucleation to Dynamic Rupture: A Physical Model of Earthquake Generation Processes”. In: *Proc. Natl. Acad. Sci. USA* 93, pp. 3795–3802.
- (2000). “A physical scaling relation between the size of an earthquake and its nucleation zone size”. In: *Pure Appl. Geophys.* 15, pp. 2259–2282.
- Ohnaka, M. and T. Yamashita (1989). “A Cohesive Zone Model for Dynamic Shear Faulting Based on Experimentally Inferred Constitutive Relation and Strong Motion Source Parameters”. In: *Proc. Natl. Acad. Sci. USA* 94, pp. 3795–3802.
- Ohta Y., et al. (2012). “Quasi real-time fault model estimation for near-field tsunami forecasting based on RTK-GPS analysis: Application to the 2011 Tohoku-Oki earthquake (Mw 9.0)”. In: *J. Geophys. Res.* 117. DOI: [10.1029/2011JB008750](https://doi.org/10.1029/2011JB008750).
- Okada, Y. (1985). “Surface deformation due to shear and tensile faults in a half-space”. In: *Bull. Seismol. Soc. Am.* 75, pp. 1135–1154.

- Olson, E. L. and R. M. Allen (2005). “The deterministic nature of earthquake rupture.” In: *Nature* 438.7065, pp. 212–215. DOI: [10.1038/nature04214](https://doi.org/10.1038/nature04214).
- Oth, A. et al. (2010). “Earthquake scaling characteristics and the scale-(in)dependence of seismic energy-to-moment ratio: Insights from KiK-net data in Japan”. In: *Geophys. Res. Lett.* 37.
- Pei, S. et al. (2009). “Structure of the upper crust in Japan from S-wave attenuation tomography”. In: *Bull. Seismol. Soc. Am.* 99, pp. 428–434. DOI: [10.1029/2011GL049580](https://doi.org/10.1029/2011GL049580).
- Peng, H. S. et al. (2011). “Developing a prototype earthquake early warning system in the Beijing Capital Region”. In: *Seismological Research Letters* 82, pp. 294–403.
- Rodriguez-Perez Q., L. Ottemoller and R. R. Castro (2012). “Stochastic finite-fault ground-motion simulation and source characterization of the 4 April 2010 Mw 7.2 El Mayor-Cucapah Earthquake”. In: *Seismol. Res. Lett.* 83, pp. 235–249. DOI: [10.1785/gssrl.83.2.235](https://doi.org/10.1785/gssrl.83.2.235).
- Romano, F. et al. (2010). “Slip distribution of the 2003 Tokachi-Oki Mw 8.1 earthquake from joint inversion of tsunami waveforms and geodetic data”. In: *J. Geophys. Res.* 115.
- Romano, F. et al. (2012). “Clues from joint inversion of tsunami and geodetic data of the 2011 Tohoku-Oki earthquake”. In: *Sci. Rep.* 2, pp. xxix–xli. DOI: [10.1038/srep00385](https://doi.org/10.1038/srep00385).
- Rubin, A. and J.-P. Ampuero (2009). “Self-similar slip pulses during rate-and-state earthquake nucleation”. In: *Geophysical Research Letters* 114.
- Rydelek, P. and S. Horiuchi (2006). “Earth science: is earthquake rupture deterministic?” In: *Nature* 442.7100. DOI: [10.1038/nature04963](https://doi.org/10.1038/nature04963).
- Rydelek, P., C. Wu, and S. Horiuchi (2007). “Comment on ”Earthquake magnitude estimation from peak amplitudes of very early seismic signals on strong motion records” by Aldo Zollo, Maria Lancieri,

- and Stefan Nielsen”. In: *Geophys. Res. Lett.* 34. DOI: [10.1029/2007GL029387](https://doi.org/10.1029/2007GL029387).
- Sagiya, T. (2004). “A decade of GEONET: 1994-2003 The continuous GPS observation in Japan and its impact on earthquake studies”. In: *Earth Planets Space* 56, pp. xxix–xli.
- Sato, M. and T. Hirasawa (1973). “BODY WAVE SPECTRA FROM PROPAGATING SHEAR CRACKS.” In: *J. Phys. Earth* 21, pp. 415–431.
- Satriano, C., A. Lomax, and A. Zollo (2008). “Real-Time Evolutionary Earthquake Location for Seismic Early Warning”. In: *Bulletin of the Seismological Society of America* 98.3, pp. 1482–1494. DOI: [10.1785/0120060159](https://doi.org/10.1785/0120060159).
- Satriano, C. et al. (2010). “PRESTo, the earthquake early warning system for Southern Italy: Concepts, capabilities and future perspectives”. In: *Soil Dynamics and Earthquake Engineering* 31.2, pp. 137–153. DOI: [10.1016/j.soildyn.2010.06.008](https://doi.org/10.1016/j.soildyn.2010.06.008).
- Shirzaei, M. and T. R. Walter (2009). “Randomly Iterated Search and Statistical Competency (RISC) as powerful inversion tools for deformation source modeling: Application to volcano InSAR data”. In: *J. Geophys. Res.* 114. DOI: [10.1029/2008JB006071](https://doi.org/10.1029/2008JB006071).
- Si, H. and S. Midorikawa (1999). “Attenuation relations for peak ground acceleration and velocity considering effects of fault type and site condition [in Japanese]”. In: *J. Struct. Construct. Eng.* 523, pp. 63–70. DOI: [10.1029/2007GL029387](https://doi.org/10.1029/2007GL029387).
- Simons, M. et al. (2011). “The 2011 magnitude 9.0 Tohoku-Oki earthquake: mosaicking the megathrust from seconds to centuries.” In: *Science (New York, N.Y.)* 332.6036, pp. 1421–1425. DOI: [10.1126/science.1206731](https://doi.org/10.1126/science.1206731).
- Stein, S. and E. A. Okal (2011). “The size of the 2011 Tohoku earthquake need not have been a surprise.” In: *Eos Trans.* 92, pp. 227–228.

- Suzuki, W., S. Aoi, and T. Sekiguchi H.and Kunugi (2011). “Rupture process of the 2011 Tohoku-Oki mega-thrust earthquake (M9.0) inverted from strong-motion data”. In: *Geophysical Research Letters* 38.July, pp. 2–7. DOI: [10.1029/2011GL049136](https://doi.org/10.1029/2011GL049136).
- Tinti, E., A. Bizzarri, and M. Cocco (2005). “Modeling the dynamic rupture propagation on heterogeneous faults with rate- and state-dependent friction”. In: *Annals of Geophysics* 48, pp. 327–345.
- Uenishi, K. and J. R. Rice (2003). “Universal Nucleation Length for Slip-Weakening Rupture Instability under Nonuniform Fault Loading”. In: *J. Geophys. Res.* 108, p. 2042.
- Wald, D. et al. (1999). “Relationships between Peak Ground Acceleration, Peak Ground Velocity, and Modified Mercalli Intensity in California”. In: *Earthquake Spectra* 15.3, p. 557. DOI: [10.1193/1.1586058](https://doi.org/10.1193/1.1586058).
- Wei, S. et al. (2011). “Superficial simplicity of the 2010 El Mayor-Cucapah earthquake of Baja California in Mexico”. In: *Nat. Geosci.* 4, pp. 615–618. DOI: [10.1038/ngeo1213](https://doi.org/10.1038/ngeo1213).
- Wells, Donald L. and Kevin J. Coppersmith (1994). “New empirical relationships among magnitude, rupture length, rupture width, rupture area, and surface displacement”. In: *Bulletin of the Seismological Society of America* 84.4, pp. 974–1002.
- Wessel, P. and W.H.F. Smith (1995). “New version of the Generic Mapping Tools Released”. In: *EOS Trans.* 76.
- Worden, C. B. et al. (2012). “Probabilistic relationships between ground-motion parameters and modified mercalli intensity in California”. In: *Bull. Seismol. Soc. Am.* 102, pp. 204–221.
- Wright, T. J. et al. (2012). “Real-time, reliable magnitudes for large earthquakes from 1 Hz GPS precise point positioning: The 2011 Tohoku-Oki (Japan) earthquake”. In: *Geophys. Res. Lett.* 39. DOI: [10.1029/2012GL051894](https://doi.org/10.1029/2012GL051894).

- Wu, Y.-M. and H. Kanamori (2005a). “Experiment on an Onsite Early Warning Method for the Taiwan Early Warning System”. In: *Bulletin of the Seismological Society of America* 95.1, pp. 347–353. DOI: [10.1785/0120040097](https://doi.org/10.1785/0120040097).
- Wu, Y.-M. and H. Kanamori (2005b). “Rapid Assessment of Damage Potential of Earthquakes in Taiwan from the Beginning of P Waves”. In: *Bulletin of the Seismological Society of America* 95.3, pp. 1181–1185. DOI: [10.1785/0120040193](https://doi.org/10.1785/0120040193).
- Wu, Y.-M. and H. Kanamori (2008a). “Development of an earthquake early warning system using real-time strong motion signals”. In: *Sensors* 8, pp. 1–9.
- Wu, Y.-M. and H. Kanamori (2008b). “Exploring the feasibility of on-site earthquake early warning using close-in records of the 2007 Noto Hanto earthquake”. In: *Earth Planets and Space* 60, pp. 155–160.
- Wu, Y. M. and T. L. Teng (2002). “A virtual sub-network approach to earthquake early warning”. In: *Bull. Seismol. Soc. Am.* 92, pp. 2008–2018.
- Wu, Y.-M. and L. Zhao (2006). “Magnitude estimation using the first three seconds P-wave amplitude in earthquake early warning”. In: *Geophysical Research Letters* 33.16, pp. 4–7.
- Yoshida, K., K. Miyakoshi, and K. Irikura (2011). “Source process of the 2011 off the Pacific coast of Tohoku Earthquake inferred from waveform inversion with long-period strong-motion records”. In: *Earth, Planets and Space* 63.7, pp. 577–582. DOI: [10.5047/eps.2011.06.050](https://doi.org/10.5047/eps.2011.06.050).
- Zollo, A., M. Lancieri, and S. Nielsen (2006). “Earthquake magnitude estimation from peak amplitudes of very early seismic signals on strong motion records”. In: *Geophysical Research Letters* 33.23, pp. 2–7. DOI: [10.1029/2006GL027795](https://doi.org/10.1029/2006GL027795).

- (2007). “Reply to comment by P. Rydelek et al. on “Earthquake magnitude estimation from peak amplitudes of very early seismic signals on strong motion records””. In: *Geophysical Research Letters* 34.20, pp. 12–15. DOI: [10.1029/2007GL030560](https://doi.org/10.1029/2007GL030560).
- Zollo, A. et al. (2010). “A threshold-based earthquake early warning using dense accelerometer networks”. In: *Geophysical Journal International* 183.2, pp. 963–974. DOI: [10.1111/j.1365-246X.2010.04765.x](https://doi.org/10.1111/j.1365-246X.2010.04765.x).
- Zollo, A. et al. (2014). “An Integrated Regional and On-Site Earthquake Early Warning System for Southern Italy: Concepts, Methodologies and Performances”. In: *Early Warning for Geological Disasters*. Ed. by Friedemann Wenzel and Jochen Zschau. Advanced Technologies in Earth Sciences. Springer Berlin Heidelberg, pp. 117–137. ISBN: 978-3-642-12232-3. DOI: [10.1007/978-3-642-12233-0_7](https://doi.org/10.1007/978-3-642-12233-0_7). URL: http://dx.doi.org/10.1007/978-3-642-12233-0_7.
- Zollo, et al. (2009). “The earthquake early warning system in southern Italy”. In: *Encycl. Complexity Syst. Sci.* Pp. 2395–2421. DOI: [10.1007/978-0-387-30440-3](https://doi.org/10.1007/978-0-387-30440-3).